DISSERTATION

BRILLOUIN LIGHT SCATTERING: A POWERFUL TOOL FOR MAGNONICS RESEARCH

Submitted by

Micthell S. Swyt

Department of Physics

In partial fulfillment of the requirements

For the Degree of Doctor of Philosophy

Colorado State University

Fort Collins, Colorado

Spring 2024

Doctoral Committee:

Advisor: Kristen S. Buchanan

Carl Patton
Carmen Menoni
Stuart Field

ABSTRACT

BRILLOUIN LIGHT SCATTERING: A POWERFUL TOOL FOR MAGNONICS RESEARCH

The slow down in generation-over-generation improvement in CMOS based logic and storage devices has spurred recent exploration into magnonic devices, those based on propagating perturbations of magnetic order called magnons, or spin waves. These devices are of particular interest due to their chargeless, low-power operation, scalability to the nanoscale, and compatibility with existing CMOS technologies. By exploiting spin waves, information may be transferred and operated upon without electrical currents. Magnetic textures like Néel domain walls, chiral transitions between magnetic domains, or skyrmions, magnetic vortices, represent additional avenues in magnonics for data storage and logic devices. Magnonic crystals, artificial crystals made by modulating magnetic properties in a periodic fashion, are one example of magnonic devices that have seen recent interest. With applicability in logic and signal processing, study of how spin waves propagate through these crystals is a necessity in the pursuit of new crystal designs. Brillouin light scattering (BLS) spectroscopy, an inelastic light scattering technique, is a powerful tool in this pursuit, as it allows for the spatial and temporal mapping of spin wave propagation.

In this thesis, we will discuss three studies of spin waves by BLS: a 1D magnonic crystal, a 2D magnonic crystal, and a study of the interfacial Dzyaloshinskii-Moriya interaction. First, time-resolved BLS was used to study the band gap formation in a 1D magnonic crystal. By mapping the propagation of spin wave pulses through the crystal, complex two dimensional interference patterns were observed. These patterns are ignored by the simple models used to understand the behavior of this crystal design, and we provide a model to calculate these patterns from the spin wave dispersion relation. The temporal development of interference that forms the basis for band gap formation in this system is also observed. Second, time-resolved BLS was used to study spin wave caustic beams in a 2D magnonic crystal. This crystal design represents a new regime in

magnonic crystals, in which the patterning dimensions are much smaller than the spin wave wavelength and generate caustic beams. The formation of a narrow (3 MHz) wide rejection band is observed and the possible mechanisms, including edge effects and interference between caustic beams, are explored. Third, the temperature dependence of the interfacial Dzyaloshinskii-Moriya interaction (iDMI) is measured in a Pt/Co film for temperatures ranging from 15 K to room temperature. Previous studies have been reported for temperatures above room temperature and this study serves to test theory over a greater range of temperatures. The iDMI parameter was quantitatively measured by measuring the frequency difference for counter-propagating surface spin waves by BLS. These three studies demonstrate that BLS is a versatile and powerful tool in the field of magnonics.

ACKNOWLEDGEMENTS

This work would not have been possible without the help and support of many people, primarily my advisor Kristen S. Buchanan. She welcomed me into her group before I even knew what a spin wave was, and without her support and guidance, I never would have made it this far.I would also like that thank my colleagues and mentors at CSU. I would like to thank Katie Nygren, who helped get me on my feet in the lab and without whom I would have been lost at the start. Carl Patton, whose advice and guidance has helped me along the way and pushed me to be a better scientific communicator. Lia Compton, who helped set up the apparatus used in much of this work and who I hope will produce great science with it after I'm gone. Cèsar Ordóñez-Romero and Giuseppe Pirruccio, who patterned the crystals in this work and helped get the project started. All of these people, and more, helped me along the path to completing this work and I will always be grateful. No one makes it through graduate school alone.

For funding and additional help on specific projects, we would like to acknowledge the following: for the 1D magnonic crystal project, we thank Michael Flatté and Denis Candido for fruitful discussions on magnonic crystals. This work was supported by the National Science Foundation Emerging Frontiers in Research and Innovation (NSF-EFRI), Grant No. NSF EFMA-1741666. For the 2D magnonic crystal project, this work was supported by the W. M. Keck Foundation and by Grants UNAM DGAPA PAPIIT No. IN104522, IG101424 and No. IG100521 and CONACyT projects 1564464 and 1098652. We acknowledge D. Ley Dominguez for technical support..

DEDICATION

I would like to dedicate this thesis to my wonderful wife, Alyx, whose constant support and encouragement has kept me going.

TABLE OF CONTENTS

ABSTRACT ii
ACKNOWLEDGEMENTS iv
DEDICATION v
LIST OF FIGURES viii

Chapter 1 Introduction 1
1.1 Magnetic Systems and Dynamics 1
1.1.1 Magnetic moments 1
1.1.2 Magnetic interactions 2
1.1.3 Continuum approximations of magnetic energies and effective fields . . 5
1.1.4 Magnetization dynamics 6
1.1.5 Spin waves and dispersion 7
1.1.6 Dispersion with the iDMI 15
1.2 Experimental Techniques 16
1.2.1 Brillouin light scattering spectroscopy 16
1.2.2 Magnetometry 27
1.2.3 Microwave characterization 32

Chapter 2 The importance of two dimensional behavior of spin waves in a 1D magnonic crystal 36
2.1 Context 36
2.2 Paper Summary 36
2.3 Research Article 37
2.3.1 Introduction 37
2.3.2 Experimental Methods 39
2.3.3 Results 41
2.3.4 Discussion 49
2.3.5 Conclusion 51

Chapter 3 Magnonic notch filter based on spin wave caustic beams 53
3.1 Context 53
3.2 Paper Summary 53
3.3 Research Article 54

Chapter 4 Low temperature Brillouin Light Scattering measurement of the interfacial Dzyaloshinskii-Moriya interaction 66
4.1 Context 66
4.2 Paper Summary 66
4.3 Research Article 67
4.3.1 Introduction 67
4.3.2 Experimental Methods 68

4.3.3 Results and Discussion 70
4.3.4 Conclusion 75

Chapter 5 Conclusion 76

Bibliography 78

Appendix A The importance of two dimensional behavior of spin waves in a 1D magnonic crystal 94
A.1 Calculation of interference patterns with reflections 95
A.2 Supplemental Materials 100

Appendix B Magnonic notch filter based on spin wave caustic beams 103
B.1 Supplemental Materials 104

LIST OF FIGURES

1.1 Forward volume spin wave dispersion relations for (a) unpinned and (b) pinned boundary conditions. Calculated for a $t = 0.25$ μm thick YIG film using $H = 3500$ Oe ($\mu_0 H = 350$ mT), $4\pi M_s = 1758$ G ($M_s = 140$ kA/m), $|\gamma| = 17.6 \times 10^{-3}$ GHz/Oe ($|\gamma| = 176$ GHz/T), and $\alpha = 3 \times 10^{-12}$ cm^2 ($J/M_s = 3 \times 10^{-8}$ m^2). n is the thickness mode number. Pinned modes must vanish at the surfaces and consequently start with $n = 1$. 10
1.2 Backward volume spin wave dispersion curves for (a) unpinned and (b) pinned boundary conditions. Calculated for a $t = 0.25$ μm thick YIG film using $H = 3500$ Oe, $4\pi M_s = 1758$ G, $|\gamma| = 17.6 \times 10^{-3}$ GHz/Oe, and $\alpha = 3 \times 10^{-12}$ cm^2. 11
1.3 Magnetostatic surface spin wave dispersion relation for (a) unpinned and (b) pinned boundary conditions. Calculated for a $t = 0.25$ μm thick YIG film using $H = 3500$ Oe, $4\pi M_s = 1758$ G, $|\gamma| = 17.6 \times 10^{-3}$ GHz/Oe, and $\alpha = 3 \times 10^{-12}$ cm^2. 12
1.4 Dispersion surface for the first three modes of an in-plane magnetized YIG film with pinned boundary conditions. The magnetic field is in-plane along the k_{BV} direction. . . 14
1.5 Dispersion relation for surface spin waves in the presence of the iDMI. Calculated using typical parameters for a Co/Pt bilayer. 15
1.6 Diagram of the beam path through the TFP2-HC. The scattered light is collected from the sample and focused through an input pinhole (P.H. In). It is then passed through each etalon (FP1 + FP2) three times, before being focused through an output pinhole (P.H. Out) and on to the photodetector (P.D.). 18
1.7 Transmission profile for a single etalon with a mirror spacing of 10 mm, calculated using Eq. 1.38. The spacing between transmission frequencies, the FSR, is labeled. . . 19
1.8 Transmission profile of the first etalon FP1 (blue), second etalon FP2 (red), and overall transmission TFP (black) at a fixed mirror position of 10 mm. Small ghost peaks appear at the repetition positions of the transmission profiles. 20
1.9 FSR and resolution of a Fabry-Pérot interferometer as functions of mirror spacing. Common mirror spacings are highlighted by the dashed lines. 21
1.10 Geometry of the TFP2-HC scanning stage. A constant ratio of mirror spacing is held between the two etalons during a scan. Reproduced from Ref. [1] 22
1.11 Transmission profiles for each of the etalons of the TFP2-HC interferometer during a scan, with mirror spacings of 10 mm and the frequencies plotted relative to the unshifted laser frequency. The black portions of the plot correspond to zero transmission, while the bright lines are the maximum transmission lines. The profiles are slightly offset one another and have narrow transmission lines. 23
1.12 Overall transmission profile of the TFP2-HC, calculated using Eq. 1.41. A bright line is observed at the frequency shift (BLS frequency) that corresponds to the frequency of the light incident on the interferometer. This central transmission line is approximately $\times 10^7$ more intense than the first ghost peaks, $\times 10^9$ than the second set of ghost peaks. 23

1.13 A typical BLS spectrum of a surface spin wave, measured in the backscattering geometry for a [1.5/1.5/1] nm W/Pt/Co film with an applied field of $H = 1500$ Oe. The Stoke, Anti-Stokes, and Ghost peaks are labeled. The central reference peak corresponds to the pure laser frequency and all frequencies are measured relative to it. . . . 28
1.14 An in-plane hysteresis curve for a 1 nm Co/Pt film measured at 10 K. The saturation magnetization, coercivity, and remanence are labeled. 29
1.15 DC SQUID magnetometer scan and detection geometry for the MPMS3 magnetometer, shown in [2] 30
1.16 Normalized magnetic field components excited by a current in a rectangular stripline antenna of width $w = 50$ μm and thickness $t = 2$ μm. 33
1.17 Normalized Fourier components of the field excited by a stripline antenna 1 μm above the antenna. The antenna has width $w = 50$ μm and thickness $t = 2$ μm. 34

2.1 a) Diagram of the magnonic crystal. The YIG film (yellow) on a GGG substrate (green) has 20 grooves of width $w = 25$ μm and depth 3.5 μm with a center-to-center spacing of $d = 275$ μm. The magnetic field H is applied along the y direction, perpendicular to the long axis of the crystal (MSSW configuration) and spin wave pulses are excited by a stripline antenna (grey). b) The measured profile of the etched grooves. c) A TR-BLS spectrum (left) showing the spin wave pulse, and the corresponding time integrated signal (right), measured at the position marked by the green dot in a) with $H = 865$ Oe and a driving frequency $f = 4.25$ GHz. 40
2.2 Comparison of BLS measurements at various driving frequencies and microwave measurements. (left) Time integrated BLS measurements as a function of frequency and position along the central axis of the magnonic crystal (shown as a dashed line in Fig 2.1a). (right) Comparison of microwave transmission measurements (blue line, measured between the left and right antennas in Fig 2.1a) and the ratio of BLS intensities measured at $x - x_0 = 4.3$ mm (red dashed line) and at $x - x_0 = 0$ are shown in red. Band gaps (BG1, BG2, and BG3) are observed in the BLS and microwave measurements. 41
2.3 Calculated dispersion relations for the first 45 odd width-quantized modes. Spatial scans were measured by BLS at the frequencies marked by dashed lines above FMR (BP, BG1, BG2, BG3 in Fig 2.4 and below FMR (A, B, C, D in Fig 2.5. The unshaded (shaded) regions indicate the wavevector ranges over which the antenna efficiently (inefficiently) excites spin waves. 42
2.4 Two-dimensional maps of the spin wave propagation, where the scan region begins at $x_0 = 1$ mm away from the edge of the antenna. The columns show, from left to right, BLS measurements, calculations with no reflections ($R = 0$), and calculations with reflections ($R = 0.01$), and the rows correspond to the frequencies marked in Fig 2.2 (BP, BG1, BG2, BG3). 43
2.5 Two-dimensional maps of the spin wave propagation as a function of the position, where the scan region begins at $x_0 = 1$ mm away from the edge of the antenna. The columns show, from left to right, BLS measurements, calculations with no reflections ($R = 0$), and calculations with reflections ($R = 0.01$), and the rows correspond to the frequencies marked in Fig 2.2 below FMR (A, B, C, D). 44

2.6 TR-BLS measurements along the length of the magnonic crystal where the intensity has been integrated over the width of the crystal. Panels (a-c) show measurements made at the first band pass (BP), while (d-f) show measurements at the first band gap (BG1). (a,d) show the pulse propagating down the full length of the crystal and (b,e) show a zoomed view (white square in (a, d)) ahead of the first etched groove. Black arrows indicate the groove positions, and the pink arrows in (e) and (f) show the positions of interference lines that develop at the first band gap BG1. No interference is observed for BP (b,c). The dark horizontal lines in (e) are absent within the region indicated by the dashed white lines and develop just to the right of the right-most line that marks the arrival times of reflection from the first groove position. 45
2.7 Calculated spin wave density as function of time for BP (a,b) and BG1 (c,d). Grooves are marked by white (black) dashed lines in (a,c) (b,d). a,c) show the calculated BLS spin wave density for the zoomed region in Fig 2.6b,e) for the BP and BG1, respectively. b,d) show single time traces spaced by 4 ns starting at $t = 135$ ns 46
2.8 a) Width averaged time-resolved BLS intensity shifted by the average pulse group velocity for the BP. The trailing edge of mode $n = 45$ is indicated by the dashed green line for the BP, and the solid green line for BG1. The group velocities for each mode are shown in b), with triangles giving the group velocity for each mode at the BP, and circles for BG1. The spatial distribution of the BLS intensity at the time marked by the white dashed line in a) are shown for c) the BP and d) BG1. The predicted trailing edge of direct arrivals for the pulse is marked by the green dashed (solid) lines for the BP (BG1). The region where the reflection from the end of the crystal is present is shaded. 48

3.1 Profilometry measurements of the 2D magnonic crystal showing (a) the patterned region and (b) a cross-sectional profile along the length of the crystal through the second row from the top. The lattice parameters $\boldsymbol{a}_1$ and $\boldsymbol{a}_2$, spacing a, and width l of the square wells are shown on (a). 56
3.2 Spin wave transmission profile in the MSSW configuration ($\phi = 0°$, green) and with H applied at $\phi = 20°$ from the y-direction (blue). The inset shows a zoomed-in view of a sharp dip in transmission observed for $\phi = 20°$ with a fit (red line). Dashed lines indicate frequencies at which the effective caustic wavelength $\lambda_{\mathtt{eff}}$ (Fig. 3.4(d)) satisfies the condition for destructive interference for $\phi = 0°$ (green) and $\phi = 20°$ (blue). 57
3.3 Time-integrated BLS intensity maps with a logarithmic intensity scale for (a) 4.320 GHz, and (b) 4.350 GHz with $\phi = 20°$, and for (c) 4.320 GHz with $\phi = 0°$. The spin waves are generated by the antenna on the left. In (a) and (b), white arrows indicate where the main pulses hit the edge of the crystal, and black arrows highlight selected caustics generated by the square wells. The white dots in the images are areas where the transmitted light intensity was low. 58

3.4 (a) Calculated dispersion relation for a YIG film with isofrequency curves (white) for $f = 4.320$ GHz and 4.350 GHz. Only the highest frequency mode is shown. Pseudo-caustic points are marked with teal arrows that indicate the direction of the group velocity. The red arrow shows the wave vector for one of the 4.320 GHz caustic points. (b) Group velocity magnitudes (top) and angle θ_{vg} (bottom) as a function of θ_k, both relative to $\boldsymbol{H}$ (y'), for 4.320 GHz. The vertical dashed line indicates the pseudo-caustic point. (c) A versus f and θ_{vg}, showing strong enhancement in specific directions. (d) Angles $|\theta_{vg}|$ (teal) and $|\theta_k|$ (red) for the maximum A in (c), and $\lambda_{\mathtt{eff}}$ (bottom) as a function of f. The inset shows a zoomed view of $\lambda_{\mathtt{eff}}$. The measurement frequencies, 4.320 and 4.350 GHz, are marked by vertical dashed lines. (e) Calculated caustic for $f = 4.320$ GHz showing a plane wave with the caustic beam position overlaid (teal lines) and the corresponding masked caustic beam (right). 61
3.5 BLS intensity as a function of time integrated over the boxed regions in (g) and (h), where the trace and box colors correspond. (a-f) BLS signals before and after the labeled wells in (g) and (h). “Pre" and “Post" signals correspond to positions along the main beam before and after interaction with a well, “Caust." is the caustic offshoot, and “Sum" is the sum of “Post" and “Caust." (black line). (i-n) BLS signals obtained before (“Pre") and after (“Post") selected edge locations, where the integration regions are indicated by the dashed boxes. The signals in (a-c,g,i-k) and (d-f,h,l-n) were obtained at 4.320 and 4.350 GHz, respectively, for $\phi = 20°$. 63

4.1 (a) BLS spectra for spin waves in Pt/Co measured at $T = 238$ K. Lorentzian fits are overlaid. (b) Frequency shifts measured at room temperature for Pt/Co and W/Co as a function of wavevector. Linear fits used to extract D are overlaid. 69
4.2 (a) Room temperature hysteresis loops for in-plane (blue) and out-of-plane (red) configurations, showing an in-plane easy axis. (b) Magnetization measurements as a function of temperature for Pt/Co at $\mu_0 H = 100$ mT (blue), values extracted from hysteresis measurements at $\mu_0 H = 100$ mT (green stars), and a fit overlaid (red). Coercivity versus temperature is shown in the inset (green stars) where the line is a guide to the eye. 71
4.3 (a) Measured spin wave frequencies, Stokes and Anti-Stokes, versus temperature. (b) FWHM of the Lorentzian fit to the spin wave peak. (c) Extracted iDMI parameter D versus temperature, with fit overlaid. (d) Log-log plot of D versus M_s, each normalized to their room temperature value. The linear fit, $\log_{10} D/D_{RT} = \alpha \log_{10} M_s/M_{s,RT} + \beta$, shows a power dependence of $\alpha = 4.5 \pm 0.8$ of D on M_s. . . . 72
4.4 (a) Measured spin wave frequencies (blue, red) and D (green) versus incident laser power. (b) Apparent local temperature extracted from linear fits to the spin wave frequencies versus temperature, and from the measured iDMI parameter versus temperature. 73

A1 Snapshots of the spin wave pulses for a) the BP, b) BG1, c) BG2, and d) BG3, 260 ns after excitation. 101
A2 Snapshots of the spin wave pulses for measurement frequencies a) A, b) B, c) C, and d) D, 260 ns after excitation. 101

A3 a) Pulse lag times vs. position for the BP, found through cross correlation. Blue markers indicate cross correlation amplitudes greater than 10% of the autocorrelation amplitude, and orange indicate amplitudes lower than 10%. A linear fit (red) to the high amplitude points is overlaid. b) An example of the cross correlated pulses, with the (black) reference pulse and (green) pulse further along the sample. 102
A4 Predicted arrival times for the first 45 odd width quantized modes for a) the BP and b) BG1. The red dashed line indicates the time marked in Fig. 2.8 a), showing the presence of direct arrivals of n$\geq$21 for the BP, and no direct arrivals present for BG1. . 102

A1 Spin wave transmission profiles of an unpatterned YIG strip measured with three input antenna locations. The legend indicates the input-output antenna separation distance. An external field of $H = 770$ Oe was applied at (a) $\phi = 0°$, (b) $\phi = 20°$, and (c) $\phi = -20°$ from the short axis of the crystal. 105

Chapter 1

Introduction

1.1 Magnetic Systems and Dynamics

Magnetic materials host a wide range of phenomena, such as spin waves, skyrmions, and domain walls, that are of interest for application in future technologies. Spin waves, also known as magnons, are propagating perturbations of the magnetic ordering [3]. Spin wave-based devices are of particular interest for chargeless, low power computing and signal processing devices, while are also attractive because they are compatible with existing CMOS technology [4–10]. Domain walls and skyrmions are of interest for new memory technologies, such as racetrack memory [11, 12], since they may be moved around reliably using spin currents [13, 14]. Understanding the dynamics of these systems, such as how spin waves propagate through a device, is a necessity to properly design future devices. Beyond applicability in new technologies, studying these systems enables the exploration of the fundamental physics and interactions driving magnetization dynamics. In this chapter, we will explore the origin of the magnetic moments that form the building blocks for these phenomena, the interactions that these moments have with each other and with external fields, and how those interactions drive the dynamics of magnetic systems. We will discuss types of spin waves that emerge and how we understand their behavior through dispersion relations, before presenting the experimental techniques used in this thesis to study spin waves. For this thesis, we will limit our discussion to the case of thin magnetic films. Equations will be given SI units.

1.1.1 Magnetic moments

The dynamics of magnetic systems are dictated by a host of competing interactions, including the interactions between magnetic moments and the magnetic moments with external and internal magnetic fields. It is thus necessary to first understand the origin of these moments and how they interact with one another. Fundamentally, magnetic moments in materials originate from the

quantum mechanical spin and orbital angular momentum of unpaired electrons in atomic orbitals [15]. The spin of the electron, $\boldsymbol{S}$, and the orbital moment, $\boldsymbol{L}$, combine to give the overall angular momentum of each electron, $\boldsymbol{S}+\boldsymbol{L}=\boldsymbol{J}$. The magnetic moment is related to these three quantities through the magnetic moment operators, $\boldsymbol{\mu}_{S,L,J}$, by

$$\mu_i = \gamma_i \hbar \boldsymbol{O}_i \tag{1.1}$$

where $\boldsymbol{O}_i = \boldsymbol{S}, \boldsymbol{L}$, or $\boldsymbol{J}$. The gyromagnetic ratio γ_i is given by

$$\gamma_i = \frac{g_i |q|}{2mc} \tag{1.2}$$

where g_i is the spectroscopic splitting factor, $|q|$ is the magnitude of the electron charge, and m is the mass of the electron. The g-factors are [16],

$$g_S \approx 2 \tag{1.3}$$

$$g_L \approx 1 \tag{1.4}$$

and

$$g_J = \frac{3}{2} + \frac{2S(S+1) - L(L+1)}{2J(J+1)}. \tag{1.5}$$

For most applications, the gyromagnetic ratio used is that of the free electron, where $|\gamma|/2\pi = 2.8 \times 10^{-3}$ GHz/T, unless γ is specifically measured. Here we will denote the microscopic magnetic moment $\boldsymbol{m}$ and the macroscopic magnetization per unit volume of a material, $\boldsymbol{M} = \sum_i \boldsymbol{m}_i / V$, is then sum of all moments present divided by the volume, V, of the material.

1.1.2 Magnetic interactions

As mentioned above, magnetic moments interact with each other, and with external fields, in a variety of ways. The exchange interaction is a purely quantum mechanical effect. The Pauli exclusion principle, which states that fermions such as the electron cannot exist in the same state as

another, results in the exchange interaction when the wave functions of electrons spatially overlap. This interaction, given by

$$E_{ex} = -\frac{1}{2}\sum_{i,j} J_{ij}\boldsymbol{S}_i \cdot \boldsymbol{S}_j, \tag{1.6}$$

where $\boldsymbol{S}_i$ is the spin at site i and J_{ij} is the exchange integral between the electron wavefunctions at site i and j, is the origin of macroscopic ferromagnetism and anti-ferromagnetism. When $J_{ij} > 0$ ($J_{ij} < 0$), the exchange aligns adjacent moments parallel (anti-parallel). This interaction is also known as symmetric exchange, or Heisenberg exchange.

The interaction with the external magnetic field $\boldsymbol{B}$ is known as the Zeeman interaction [17],

$$E_{zm} = -\boldsymbol{m} \cdot \boldsymbol{B}, \tag{1.7}$$

which promotes the alignment of the moment with the applied field. The dipole-dipole interaction [18],

$$E_{dip} = \sum_{i \neq j} -\frac{\mu_0}{4\pi|\boldsymbol{r}|^3}\left[3(\boldsymbol{m}_i \cdot \widehat{\boldsymbol{r}})(\boldsymbol{m}_j \cdot \widehat{\boldsymbol{r}}) - \boldsymbol{m}_i \cdot \boldsymbol{m}_j + \frac{8\pi}{3}\boldsymbol{m}_i \cdot \boldsymbol{m}_j \delta(\boldsymbol{r})\right], \tag{1.8}$$

the interaction of a moment with the dipolar field of another moment, promoting head-to-tail or anti-parallel alignment of adjacent moments. As the interaction scales $\propto \boldsymbol{r}^{-3}$, the dipole-dipole interaction is reasonably long-range in the context of magnetic materials.

In systems where there is a lack of inversion symmetry, such as at the interface between thin film layers [19–22] or in non-centrosymmetric crystals like the B20 space group [23–27], an antisymmetric exchange interaction can exist. Known as the Dzyaloshinskii-Moriya interaction (DMI), the antisymmetric exchange is mediated by an atom at a third site, such as a heavy metal atom across an interface [28]. The DMI, given by

$$E_D = -\sum_{i \neq j} \boldsymbol{D}_{ij} \cdot \boldsymbol{S}_i \times \boldsymbol{S}_j, \tag{1.9}$$

favors perpendicular alignment of adjacent spins. $\boldsymbol{D}_{ij}$ is the DMI vector, and has direction dictated by either the crystal symmetry, or pointing along the plane of the interface. This interaction is

typically weak in comparison to the exchange or dipolar interactions, so it plays the role of a minor perturbation. The DMI serves to stabilize chiral magnetic textures, such as Néel domain walls and skyrmions, as it gives a preferential direction of twisting to adjacent moments [12, 29]. In thin film systems where the interfacial DMI (iDMI) is present, it also provides a preferred direction of surface spin wave propagation, increasing the attenuation length in the preferred direction and decreasing it in the opposite direction [30, 31].

Anisotropies in magnetic materials lead to energetically preferential directions for the magnetization. There are several origins of magnetic anisotropy, the most notable being shape, magneto-crystalline, and surface anisotropy.

Magneto-crystalline anisotropy originates in the spin-orbit interaction, as the inclusion of the orbital angular momentum in the total magnetic moment causes the magnetic moment to be sensitive to anisotropies in the crystal structure [32]. This creates preferential directions for the magnetization that are determined by the crystal symmetry. For hexagonal crystals such as Co, or crystals with uniaxial anisotropy, the magneto-crystalline energy density can be described as

$$K_{uni} = K_0 + K_1 \sin^2\theta + K_2 \sin^4\theta + ..., \tag{1.10}$$

where $K_0, K_1, K_2, ...$ are the anisotropy constants, and θ is the angle of $\boldsymbol{M}$ relative to the anisotropy axis [32]. For hexagonal crystals, the anisotropy axis lies along the c axis of the crystal lattice. For thin films, which are typically polycrystalline, the magneto-crystalline anisotropy is usually neglected due to the random orientations of the grains in the film.

The anisotropy in thin films can vary strongly from the bulk, due to the increased importance of surface or interfacial effects [33]. Thus, in experimental studies of thin films with uniaxial or perpendicular anisotropy, the anisotropy energy is often represented by an effective anisotropy, given by

$$E_{ani} = K_{eff} \sin^2\theta \tag{1.11}$$

where θ is defined relative to the normal of the film and K_{eff} containing both bulk and surface components, according to

$$K_{eff} = K_u + \frac{1}{2}\mu_0 M_s^2. \tag{1.12}$$

K_u is the uniaxial anisotropy due to surface or interfacial effects and M_s is the saturation magnetization, and the second term represents the shape anisotropy for a saturated thin film. Films with $K_{eff} > 0$ have an out-of-plane easy axis, and $K_{eff} < 0$ an in-plane easy plane with no preferred direction in-plane.

1.1.3 Continuum approximations of magnetic energies and effective fields

At the quantum level, interactions between magnetic moments are described pairwise for each set of pairs in the system. At the length scales of interest in this work, it is convenient to apply a continuum approximation of the demagnetization and exchange energies and to find effective fields for each interaction. To find the demagnetization energy, the starting point is the Zeeman energy per unit volume,

$$E_{zm} = -\boldsymbol{M} \cdot \boldsymbol{B}, \tag{1.13}$$

where the only change compared to Eq. 1.7 is the magnetic moment $\boldsymbol{m}$ becomes the total magnetization vector $\boldsymbol{M}$ and $\boldsymbol{B}$ is the total magnetic field due to all other magnetic moments. The dipole-dipole energy can be found using a Green's function approach, as described in [18], giving

$$E_{dip} = \int d\boldsymbol{r}' \left(\frac{\boldsymbol{r} - \boldsymbol{r}'}{4\pi|\boldsymbol{r} - \boldsymbol{r}'|} \right) \cdot \boldsymbol{M}(\boldsymbol{r}'), \tag{1.14}$$

where the integral is over the full volume of the system. The Green's function approach also allows for the inclusion of the effects of the nonuniform magnetization states, static or dynamic, such as the presence of a spin wave. The effective field associated with the demagnetization energy is known as the demagnetization field $\boldsymbol{H}_{demag}$ and is simply the negative gradient of E_{dip},

$$\boldsymbol{H}_{demag} = -\nabla E_{dip}. \tag{1.15}$$

The effective exchange field is given by

$$\boldsymbol{H}_{ex} = \lambda_{ex} \nabla^2 \boldsymbol{M} \tag{1.16}$$

where $\lambda_{ex} = \sqrt{\frac{A}{2\pi M_s^2}}$ is the exchange length. The particulars of the anisotropy field differs with the exact symmetry of the anisotropy, but can be written generally as

$$\boldsymbol{H}_{ani} = -\frac{1}{M_s} \nabla_{\boldsymbol{M}} E_{ani} \tag{1.17}$$

1.1.4 Magnetization dynamics

Equations of motion form the framework through which we understand how the previous discussed interactions contribute to the dynamics of magnetic systems. Dynamic excitations provide insight into the origin of different observed phenomena, such as ferromagnetic resonance conditions, spin wave dispersion relations, the formation of spin wave caustic beams, and more.

The most basic equation of motion for magnetic systems is the torque equation. Given by

$$\frac{d\boldsymbol{M}}{dt} = -\mu_0 |\gamma| \boldsymbol{M} \times \boldsymbol{H}_{\boldsymbol{eff}}, \tag{1.18}$$

where

$$\boldsymbol{H}_{eff} = \boldsymbol{H}_0 + \boldsymbol{H}_{demag} + \boldsymbol{H}_{ex} + \boldsymbol{H}_{ani} + \boldsymbol{H}_{dmi} + ... \tag{1.19}$$

is the sum of all the static applied field, $\boldsymbol{H}_0$, and all other effective fields in the system. Eq. 1.18 describes the precession of the magnetization about the effective field, but lacks any term to dampen the precessional amplitude of the magnetization. As real systems do not precess infinitely and come into equilibrium with the magnetization parallel to H_{eff}, the torque equation is obviously lacking in physicality. It can, however, be used to calculate the ferromagnetic resonance condition, such as the well known Kittel equation [34],

$$f = \mu_0 \frac{|\gamma|}{2\pi} \sqrt{H_0 (H_0 + M_s)} \tag{1.20}$$

where f is the ferromagnetic resonance frequency.

There are two main equations used to phenomenologically capture the damping of the magnetization. The first method was derived by Landau and Lifshitz [35],

$$\frac{d\boldsymbol{M}}{dt} = -\mu_0|\gamma|(\boldsymbol{M} \times \boldsymbol{H}_{eff}) + |\gamma|\frac{\lambda}{M_s^2}(\boldsymbol{M} \times (\boldsymbol{M} \times \boldsymbol{H}_{eff})), \tag{1.21}$$

where the damping parameter λ dictates the rate the precessional amplitude decreases.

The second method was proposed by Gilbert [36], in which Eq. 1.18 is substituted into Eq. 1.21, giving

$$\frac{d\boldsymbol{M}}{dt} = -\mu_0|\gamma|(\boldsymbol{M} \times \boldsymbol{H}_{eff}) + \frac{\alpha_G}{M_s}\left(\boldsymbol{M} \times \frac{d\boldsymbol{M}}{dt}\right), \tag{1.22}$$

where α_G becomes the Gilbert damping parameter. Both methods preserve the component of the magnetization parallel to $\boldsymbol{H}_{eff}$, as the damping torque will lie in the plane perpendicular to the $\boldsymbol{H}_{eff}$. Other equations of motion that do not preserve the magnetization vector, such as the Bloch-Bloembergen equation [37, 38], exist but will not be discussed here. Gilbert's version (eq. 1.22) is used most frequently, especially in micromagnetics [39, 40].

1.1.5 Spin waves and dispersion

Spin waves are non-uniform, propagating magnetic excitations. They behave as waves and exhibit wave-like behavior, such as interference and diffraction. The simplest illustration of a spin wave is that of a chain of spins precessing about a field at the same frequency, with a phase difference between each neighboring spin. The equations of motion discussed above provide means to understand the behavior of these spin waves, since the equations of motions, along with appropriate expressions for the effective magnetic fields, can be used to derive the spin wave dispersion relations. The dispersion relation, $\omega(\boldsymbol{k})$, relates the frequency (ω), or energy ($\hbar\omega$), of the spin wave to the wavevector ($\boldsymbol{k} = (2\pi/\lambda)\widehat{\boldsymbol{k}}$), or momentum ($\hbar\boldsymbol{k}$). A dispersion relation shows how the fields discussed in Section 1.1.2 influence the behavior of the wave. From the dispersion relation, the

group velocity

$$v_g = \frac{\partial \omega}{\partial \boldsymbol{k}}, \tag{1.23}$$

and the phase velocity

$$v_p = \frac{\omega}{k} \tag{1.24}$$

can also be found, which dictate the propagation characteristics of the spin wave. For a propagating wave, the group velocity determines how the energy of the wave will travel, while the phase velocity determines how the phase of the wave will change in time and space. In the case of a wave packet, the envelope of the wave packet will travel at the group velocity, while the phase of the wave under the envelope will evolve in time according to the phase velocity. The phase velocity will always be parallel to the wavevector, while the direction of the group velocity may differ due to the details of the dispersion relation.

There exists a broad spectrum of spin waves, depending on the particulars such as the relative directions of the magnetization, the spin wave wavevector, and the film normal. Here, we will focus on three limiting cases for thin films under the magnetostatic approximation: the magnetostatic forward volume spin wave (MSFVSW), the magnetostatic backward volume spin wave (MSBVSW), and the magnetostatic surface spin wave (MSSW). For each of these cases, the direction of the wavevector relative to the magnetization and the film normal determines the type of spin wave, and the rate of change of the magnetization is assumed to be slow with respect to the speed of light. For intermediate directions, spin wave states also exist following a smooth transition between the high symmetry solutions. The collection of all possible spin wave states is known as the spin wave manifold. In addition to these propagating spin waves, standing modes appear in confined systems.

Standing Waves

Like standing waves on a string, standing spin waves appear in confined magnetic systems. The confinement is typically either along the depth of the film, where perpendicular standing spin wave (PSSW) modes appear across the thickness of the film [41], or laterally such as in thin magnetic

wires, where width-quantized spin wave modes appear across the width of the wire [42, 43]. In either case, these standing modes are characterized by a quantized wavevector along their direction of confinement. For the PSSW, the wavevector is

$$\kappa_n = \frac{n\pi}{t}, \tag{1.25}$$

where n is the mode number, and t is the thickness of the film. Similarly for the width-quantized mode, the wavevector is

$$k_m = \frac{m\pi}{w}, \tag{1.26}$$

where m is the mode number, and w is the width of the film. For either of these modes, the dynamic magnetization can either be pinned, where $\boldsymbol{m} = 0$ at the interface, or unpinned where $\partial \boldsymbol{m}/\partial n = 0$ at the interface. In the pinned case, the spins at the interface cannot precess and the mode amplitude goes to zero. In the unpinned case, the spins are free to precess. The pinning conditions must be determined experimentally, as they are dictated by the surface conditions [44]. These standing modes can mix with the propagating spin wave modes to create additional branches of the dispersion relations.

We will discuss each of the propagating spin wave modes and how they may be understood using the dispersion relations. There are several methods that are used to calculate dispersion relations, ranging from finding analytical solutions for limiting cases, such as along specific high-symmetry directions, to matrix methods for finding numerical approximations of the dispersion relation. The dispersion relations used in this work are found both ways, using the analytical expression for specific directions, as well as the numerical matrix method described in [45]. An additional relation for surface waves in the presence of the iDMI is used and the derivation can be found in [30, 31]. Here, we will use the main results of these works to discuss the features of the different spin wave modes.

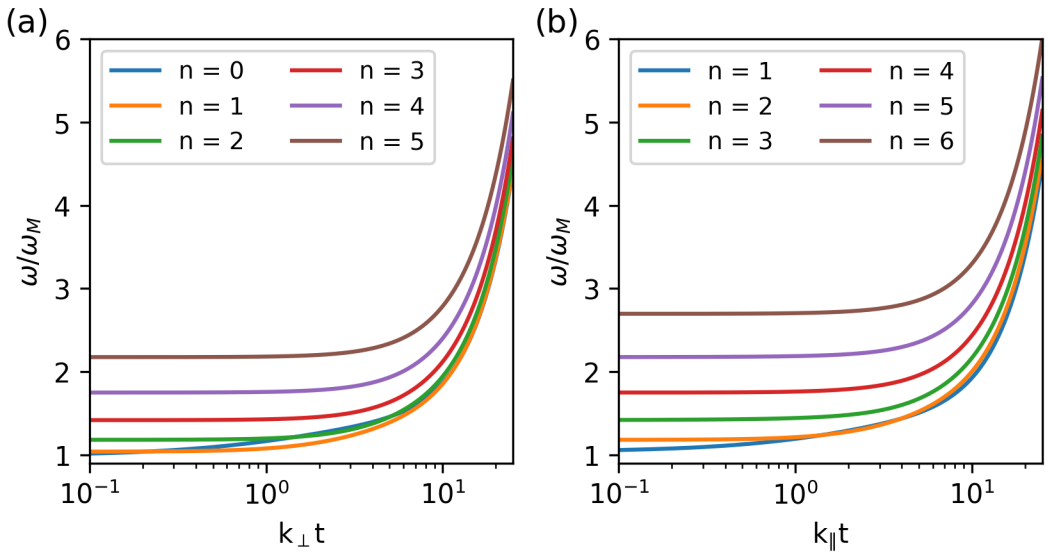

Figure 1.1: Forward volume spin wave dispersion relations for (a) unpinned and (b) pinned boundary conditions. Calculated for a $t = 0.25$ μm thick YIG film using $H = 3500$ Oe ($\mu_0 H = 350$ mT), $4\pi M_s = 1758$ G ($M_s = 140$ kA/m), $|\gamma| = 17.6 \times 10^{-3}$ GHz/Oe ($|\gamma| = 176$ GHz/T), and $\alpha = 3 \times 10^{-12}$ cm^2 ($J/M_s = 3 \times 10^{-8}$ m^2). n is the thickness mode number. Pinned modes must vanish at the surfaces and consequently start with $n = 1$.

Magnetostatic Forward Volume Spin Waves (MSFVSW)

The forward volume spin wave (MSFVSW) mode appears when a film is magnetized out-of-plane and the wavevector is fixed in-plane. The propagation of the MSFVSW is isotropic in-plane and the mode has a standing wave profile across the thickness of the film. It is a volume wave, in that the mode is present across the full thickness of the film. The group and phase velocities of this mode are always parallel to one another.

For the MSFVSW case, the dispersion relation is [46]

$$\omega = \sqrt{(\omega_0 + \alpha\omega_M k_n^2)(\omega_0 + \alpha\omega_M k_n^2 + \omega_M P_n)} \tag{1.27}$$

where

$$\kappa_n = \frac{n\pi}{t}, \; k_n = \sqrt{k_\parallel^2 + \kappa_n^2}, \tag{1.28}$$

$$\omega_H = |\gamma| H, \; \omega_M = |\gamma| M_s, \; \omega_0 = \omega_H - \omega_M, \tag{1.29}$$

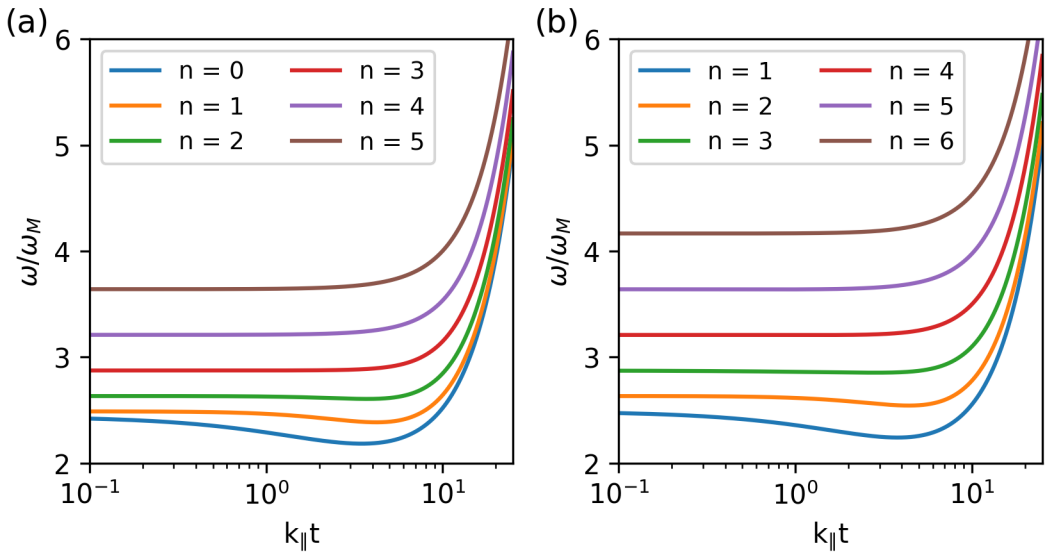

Figure 1.2: Backward volume spin wave dispersion curves for (a) unpinned and (b) pinned boundary conditions. Calculated for a $t = 0.25$ μm thick YIG film using $H = 3500$ Oe, $4\pi M_s = 1758$ G, $|\gamma| = 17.6 \times 10^{-3}$ GHz/Oe, and $\alpha = 3 \times 10^{-12}$ cm^2.

where $k_\parallel$ is the wavevector parallel to the surface of the film, while κ_n is the wavevector normal to the surface and k_n is the total wavevector. $|\gamma|$ is the gyromagnetic ratio, α is the exchange constant, n is the thickness mode number, and t is the film thickness. The demagnetization factors, P_n, are

$$P_n = \frac{k_\parallel^2}{k_n^2} - \frac{2}{k_\parallel t}\frac{k_\parallel^4}{k_n^4}\frac{1}{1+\delta_{0n}}(1-(-1)^n e^{-|k_\parallel|t}) \tag{1.30}$$

for pinned boundary conditions, and

$$P_n = \frac{k_\parallel^2}{k_n^2} + \frac{2}{k_\parallel t}\frac{k_\parallel^2\kappa_n^2}{k_n^4}(1-(-1)^n e^{-|k_\parallel|t}) \tag{1.31}$$

for unpinned boundary conditions. The integer values differ for depending on the boundary conditions, with $n = 1, 2, 3...$ for pinned boundary conditions, and $n = 0, 1, 2, 3, ...$ for unpinned boundary conditions. P_n represents the effect of the dipolar boundary conditions on the dispersion.

The first several thickness modes for the MSFVSW are shown in Fig. 1.1 (a) for unpinned boundary conditions and (b) for pinned boundary conditions. These modes are calculated for a $t =$

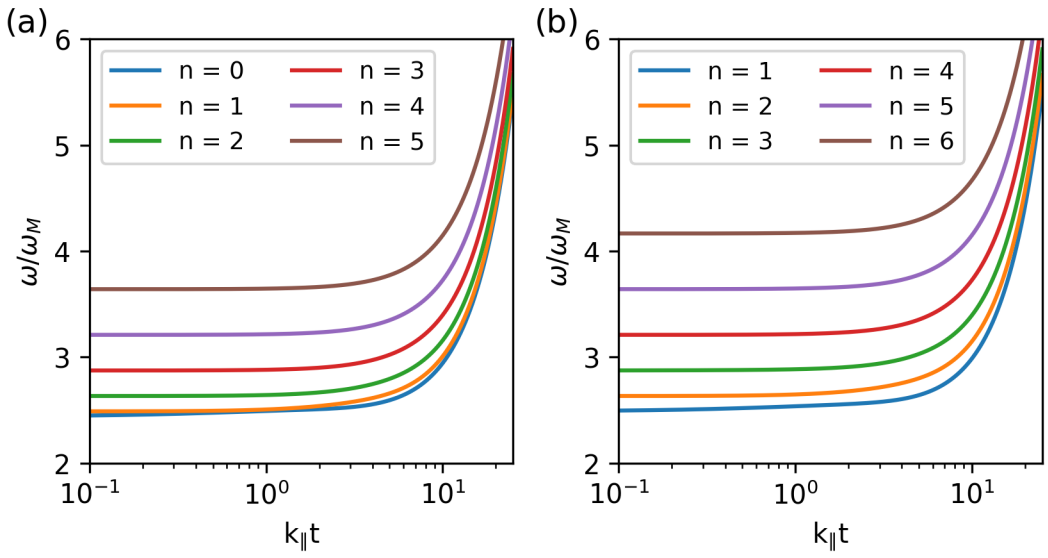

Figure 1.3: Magnetostatic surface spin wave dispersion relation for (a) unpinned and (b) pinned boundary conditions. Calculated for a $t = 0.25$ μm thick YIG film using $H = 3500$ Oe, $4\pi M_s = 1758$ G, $|\gamma| = 17.6 \times 10^{-3}$ GHz/Oe, and $\alpha = 3 \times 10^{-12}$ cm^2.

0.25 μm thick film with values typical for YIG, using $H = 3500$ Oe, $4\pi M_s = 1758$ G, $|\gamma| = 17.6 \times 10^{-3}$ GHz/Oe, and $\alpha = 3 \times 10^{-12}$ cm^2. The dispersion curves are plotted where the frequencies are scaled by ω_M and plotted as a function of $k_\parallel t$ on a logarithmic scale to emphasize the features of the dispersion curves. For the MSFVSW case, the dispersion relations are isotropic in the plane of the film. The lowest-order thickness mode ($n = 0$ for unpinned, $n = 1$ for pinned) crosses the higher modes for intermediate $k_\parallel t$. Each mode increases in frequency with increasing $k_\parallel t$, and all of the thickness modes converge at large $k_\parallel t$, where the spin wave wavelength becomes short. This is the exchange limit, where the dispersion is dominated by the exchange interaction and spin waves in this range are known as exchange spin waves. The wavelengths become sufficiently short in the exchange limit that the thickness mode contributions become small and the modes converge. For long wavelengths, the dispersion is dominated by the dipole-dipole interaction, known as the dipole limit, and the spin waves are called dipolar spin waves. The intermediate region, where the exchange and dipolar interactions both play appreciable roles, is where the majority of spin waves observed in this thesis reside, and the spin waves are called dipole-exchange spin waves.

Magnetostatic Backward Volume Spin Waves (MSBVSW)

When a film is magnetized in-plane, the behavior of spin waves differs greatly depending on whether the wavevector lies along the magnetization, or perpendicular to it. The magnetostatic backward volume spin wave (MSBVSW) mode appears in the case where $\boldsymbol{k} \parallel \boldsymbol{M}$. The group velocity and the phase velocity of the MSBVSW are anti-parallel, hence the spin wave appear to be propagating backwards, giving these modes their name. Like the MSFVSW, the MSBVSW is a volume mode with a standing mode profile across the depth of the film.

For the magnetization lying in-plane, the dispersion relation is [45]

$$\omega = \sqrt{(\omega_H + \omega_M + \alpha\omega_M k_n^2 - \omega_M P_n)(\omega_H + \alpha\omega_M k_n^2 + \omega_M P_n \sin^2\theta)}, \tag{1.32}$$

where θ is the angle of $k_\parallel$ relative to $\boldsymbol{M}$, where $\theta = 0$ corresponds to the MSBVSW configuration and $\theta = \pi/2$ the MSSW. The collection of all possible states, in all possible directions, is the spin wave manifold. The first MSBVSW modes, shown in Fig. 1.2, have a dip in the dispersion curves as $k_\parallel t$ where the slope becomes negative. These regions with a negative slope have group velocities that point in the direction opposite the phase velocity, making the waves appear to be traveling backwards, giving the mode its name. As with the MSFVSW, the modes converge in the exchange limit, at large wavevectors.

Magnetostatic Surface Spin Waves (MSSW)

The magnetostatic surface spin wave (MSSW) mode, also known as the Damon-Eshbach (DE) mode after the authors of Ref. [47], has the magnetization in-plane and the wavevector perpendicular to the magnetization. The mode is localized on the surfaces of the film and the mode amplitude follows an exponential-like decay across the depth of the film. The decay length is typically on the order of the spin wave wavelength. The MSSW mode is inherently non-reciprocal, as waves propagating in one direction are localized on one surface, and those traveling in the opposite direction the other. The direction of propagation for each surface can be determined using the right hand rule. The first several MSSW modes are shown in Fig. 1.3. The MSSW dispersion relations

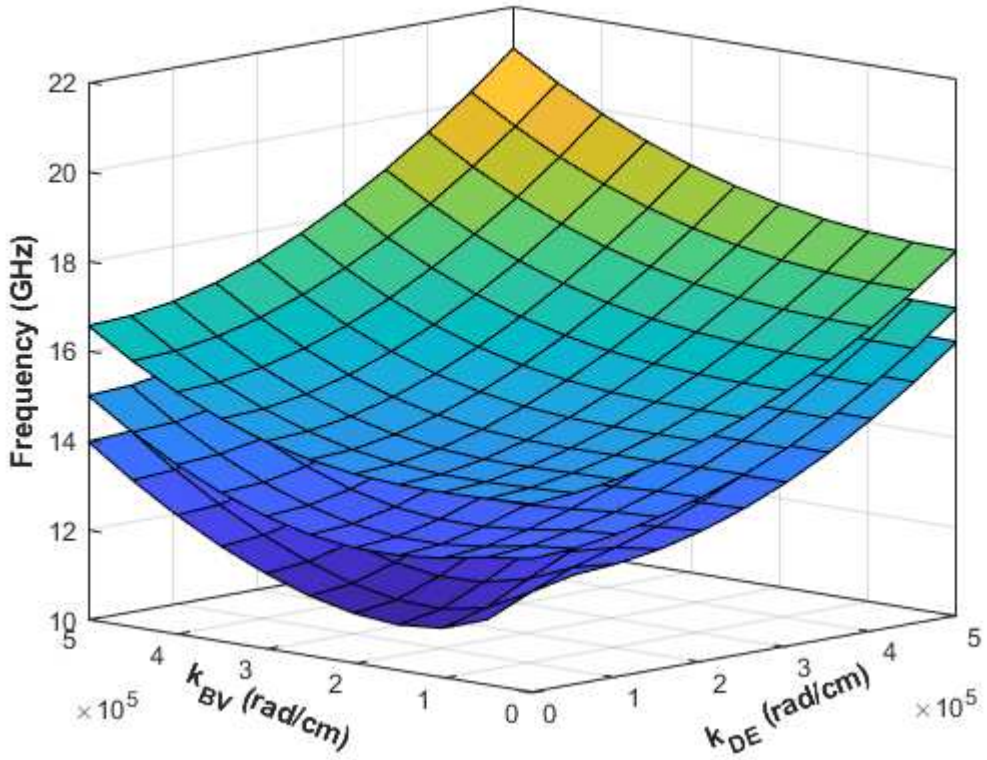

Figure 1.4: Dispersion surface for the first three modes of an in-plane magnetized YIG film with pinned boundary conditions. The magnetic field is in-plane along the k_{BV} direction.

have the same large wavevector limit behavior as the other modes at very large wavevectors, and the modes are exchange dominated. In the dipolar region, the frequency increases with increasing $k_{\|}t$.

To illustrate the dispersion at intermediate angles in-plane, the dispersion surfaces for the first three modes are shown in Fig. 1.4 for pinned boundary conditions, calculated using the matrix method in [45]. k_{BV} denotes the wavevector along the backward-volume direction, and k_{DE} denotes the wavevector along the surface wave direction. The same values were used for this calculation as in the previous curves. The transition between the MSBVSW and MSSW is smooth. At angles near the MSBVSW, there is a dip in the dispersion surface that disappears towards $\theta = \pi/4$. Higher modes lose this depression, which is due to the contribution of the dynamics to the demagnetization field, in the dispersion relations.

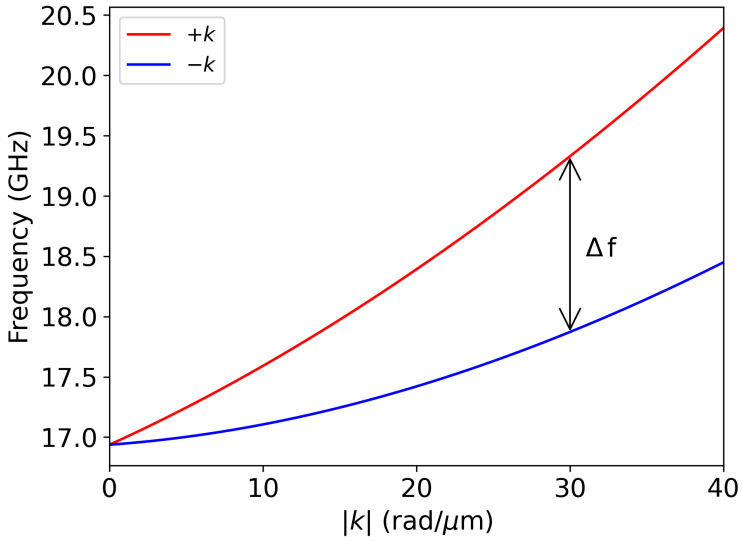

Figure 1.5: Dispersion relation for surface spin waves in the presence of the iDMI. Calculated using typical parameters for a Co/Pt bilayer.

The work in this thesis will focus primarily on surface waves, as well as on surface waves mixed with standing modes.

1.1.6 Dispersion with the iDMI

One particular analytical dispersion relation of interest for this thesis is for the MSSW in the presence of the iDMI. Derived in [30], the dispersion relation becomes, in this case,

$$\omega = \mu_0|\gamma|\sqrt{(H + M_s/4 + Jk^2)(H + 3M_s/4 + Jk^2) - \frac{e^{-4|k|t}M_s^2}{16}(1 + 2e^{2|k|t})} + p\frac{2|\gamma|D}{M_s}k, \tag{1.33}$$

where D is the iDMI parameter, t is the film thickness, $J = 2A/\mu_0 M_s$ is the exchange constant, and p is the polarity of the magnetization. The magnetization polarity, $p = \pm 1$, is determined by the magnetization direction relative to the symmetry breaking direction. The iDMI introduces the term outside the square root that is linearly proportional the wavevector. The dispersion relation is now sensitive not only to the magnitude of k, but also the sign of k. This introduces an asymmetry in the dispersion and propagation in one direction now has a higher frequency than the opposite for spin waves with the same wavevector. The frequency difference between counter propagating

spin waves is given by

$$\Delta f = p\frac{2|\gamma|D}{\pi M_s}k. \tag{1.34}$$

Fig. 1.5 shows the dispersion relation using values appropriate for a Co/Pt bilayer, with $M_s = 1.4$ MA/m, $D = 1.5$ mJ/m^2, $t = 1$ nm, $\mu_0 H = 0.2$ T, $A = 1.3 \times 10^{-11}$ J/m. The frequency difference, Δf, becomes appreciable at larger wavevectors and becomes large enough to be quantitatively determined by experimental techniques such as Brillouin light scattering.

1.2 Experimental Techniques

1.2.1 Brillouin light scattering spectroscopy

Brillouin Light Scattering (BLS) spectroscopy is an inelastic light scattering technique used to quantitatively measure the dynamic properties of magnetic (magnon), elastic (phonon), and electronic (polariton) waves in media. BLS was first proposed theoretically by Brillouin in 1922, and because of the sensitivity of this technique and the wide range of dynamic systems that can be studied, it has grown into a powerful technique that is used for physics, materials science, geology, biomedical, and engineering research [48]. BLS has recently become of particular interest due to the increasing interest in magnetic systems for application in spintronic devices. Through specific implementations of the technique, quantitative measurements of a diverse range of elastic and magnetic properties can be made, including elements of the elastic tensor, the exchange constant, the interfacial Dzyaloshinskii-Moriya interaction parameter, and more. Aside from specific physical properties, spatial and temporal maps of wave propagation can be made with BLS.

Scattering mechanism of BLS

The fundamental mechanism behind BLS is the inelastic scattering of light from a wave in a medium. As a wave, such as a phonon or magnon, travels through a medium, it causes a corresponding oscillation in the dielectric tensor ($\boldsymbol{\epsilon}$). For a magnon, this occurs through the coupling of the magnetic system to the dielectric tensor through magneto-optic effects [49]. For a phonon, the fluctuations of the charge density due to the lattice vibrations causes the change in $\boldsymbol{\epsilon}$ [50,51]. There

are two main ways to picture the interaction of light with the wave. First, a classical description can be used, where the wave is considered as a moving diffraction grating. The scattering can then be described as a Bragg diffraction with an associated Doppler shift, which leads to a shift in the wavevector and frequency of the scattered light determined by the wave's phase velocity [50]. The second description, a quantum mechanical description, uses a particle/quasi-particle scattering description. The light is described as photons interacting with quasi-particles (magnon, phonon) in the medium through either the creation of a new quasi-particle or the annihilation of an existing quasi-particle.

For either description, the end result is the same. Through the conservation of energy and momentum, the scattered light will have momentum and energy given by

$$\hbar \boldsymbol{k_{sc}} = \hbar \boldsymbol{k_i} \pm \hbar \boldsymbol{q} \tag{1.35}$$

$$\hbar \omega_{sc} = \hbar \omega_i \pm \hbar \omega \tag{1.36}$$

where $\boldsymbol{k_{sc}}$, ω_{sc}, $\boldsymbol{k_i}$, ω_i, and $\boldsymbol{q}$, ω are the wavevectors and frequency of the scattered light, incident light, and quasi-particle (magnon, phonon) respectively. For magnons in a thin film, only the in-plane momentum is conserved, rather than the total momentum. These processes are known as the Stokes process (creation), and the Anti-Stokes process (annihilation), and show up in a BLS spectra as negative and positive frequency shifts relative to the elastically scattered light respectively. Fundamentally, BLS as a technique provides information directly on three properties: wavevector, frequency, and polarization. As will be discussed later, the exact scattering geometry of the experiment can be used to determine the wavevector measured, while the interferometer is used to measure the frequency shift of the scattered light. The polarization change of the scattered light also provides information about what type of wave is being measured, since how the wave modifies the dielectric tensor also determines the polarization of the scattered light. For instance, magnetostatic surface waves rotate the polarization of scattered light by 90°, while scattering from bulk longitudinal phonons preserve the polarization of the light. A review of the scattering rules

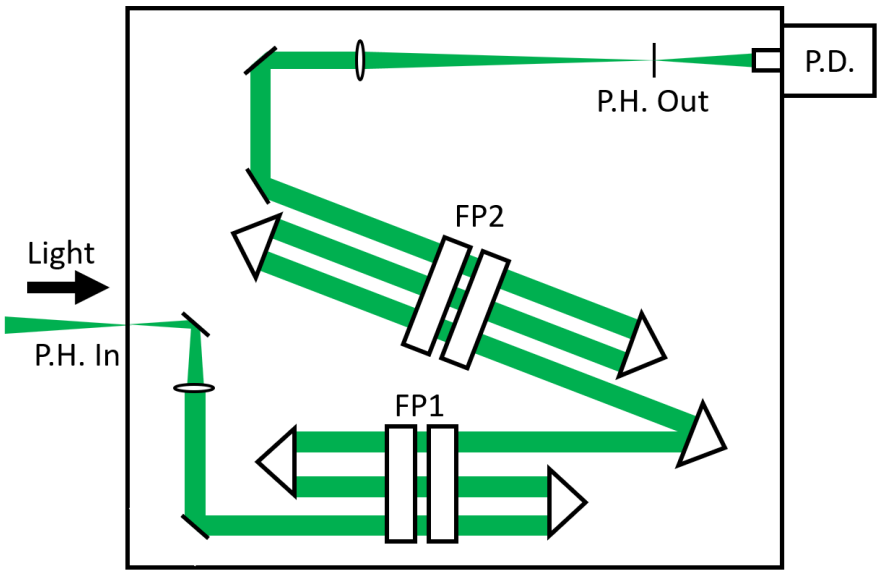

Figure 1.6: Diagram of the beam path through the TFP2-HC. The scattered light is collected from the sample and focused through an input pinhole (P.H. In). It is then passed through each etalon (FP1 + FP2) three times, before being focused through an output pinhole (P.H. Out) and on to the photodetector (P.D.).

for phonons can be found in Ref. [51] and for magnons in Ref [52]. The combination of the wavevector dependence of the frequency, as well as the polarization of the light can be used to determine what type of wave is being observed.

The Tandem Fabry-Pérot Interferometer

The scattered light in a BLS experiment is analyzed using a Tandem Fabry-Pérot (TFP) Interferometer. The shift in frequency of the scattered light is sufficiently small, typically in the GHz range, that methods used for other spectroscopic techniques such as Raman spectroscopy, do not have sufficient resolution [53]. The high contrast achieved by the TFP, up to $\times 10^{11}$ for the main transmission line relative to other frequencies, is also a necessity due to the low scattering intensity from thermal magnons. In Raman spectroscopy, the frequency shifts observed are typically in the THz range and are distinguishable through use of a diffraction grating to spatially separate the light, but the resolution of a grating spectrometer is insufficient to observe the low frequency dynamics of interest in a BLS experiment. Thus, the specialized TFP interferometer is required. The interferometer used for experiments in this thesis, a TFP2-HC interferometer from Table Sta-

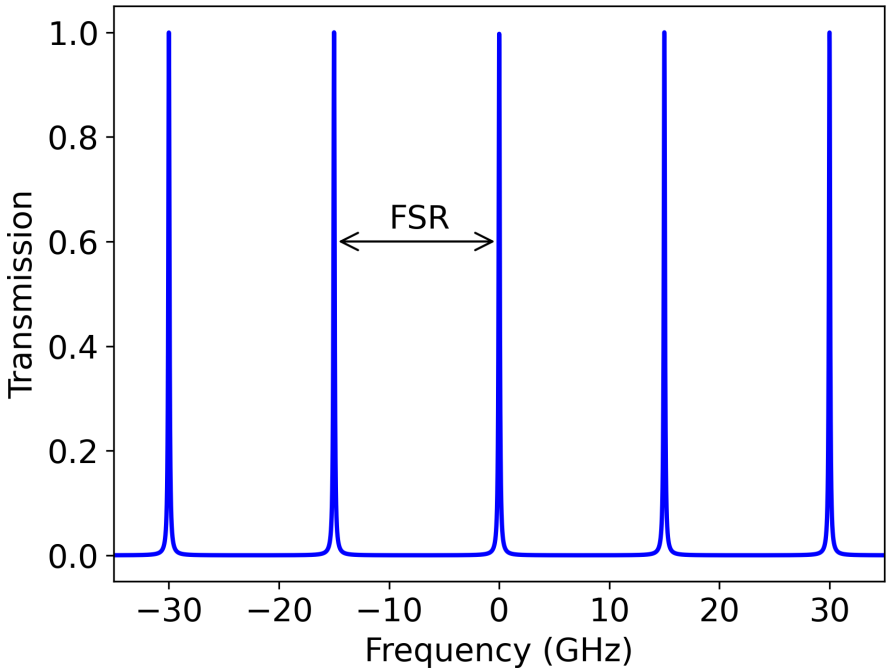

Figure 1.7: Transmission profile for a single etalon with a mirror spacing of 10 mm, calculated using Eq. 1.38. The spacing between transmission frequencies, the FSR, is labeled.

ble LTD. This interferometer uses a pair of coupled etalons with a 3+3 pass design [1]. A diagram of the beam path within the interferometer is shown in Fig. 1.6. Each etalon acts as an individual Fabry-Pérot interferometer and they are coupled together to unambiguously measure the small frequency shifts.

In a typical BLS experiment, the scattered light that enters the interferometer containing both elastically and inelastically scattered light. The photodetector used to detect the light cannot distinguish between frequencies of light, so the frequency discrimination must happen before the photodetector. This is the role of the paired etalons. Each etalon is composed of a pair of flat, parallel mirrors. The light enters the etalon and as it is reflected many times within, it interferes constructively or destructively with itself, depending on the phase difference acquired upon each round trip between mirrors. Constructive interference will occur when the relative phase difference between photons is $2\pi n$, where n is some integer. This gives a phase shift

$$\delta = 2\pi n = \frac{2\pi}{\lambda} 2L, \tag{1.37}$$

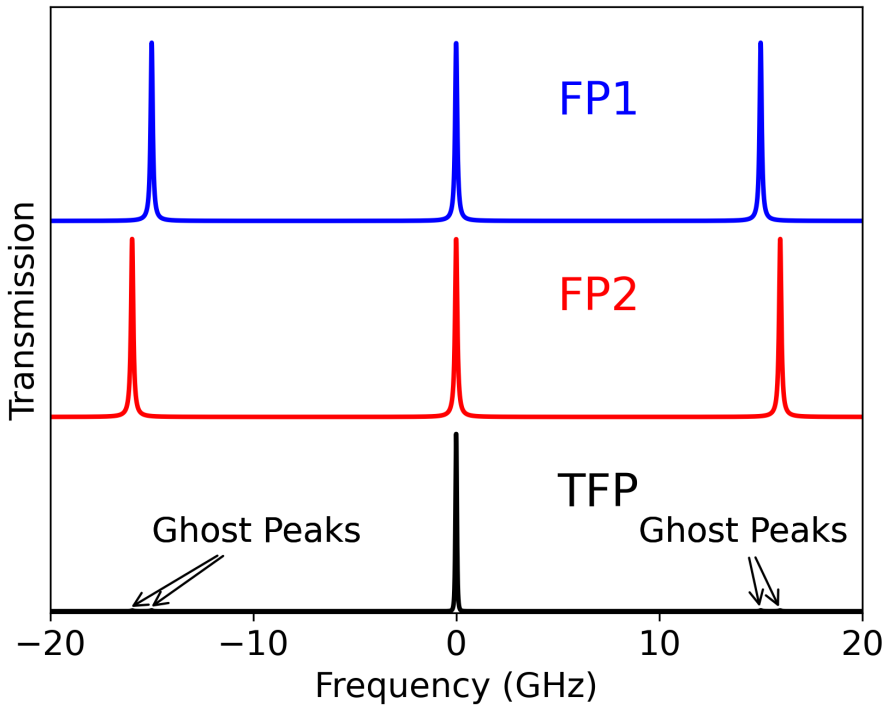

Figure 1.8: Transmission profile of the first etalon FP1 (blue), second etalon FP2 (red), and overall transmission TFP (black) at a fixed mirror position of 10 mm. Small ghost peaks appear at the repetition positions of the transmission profiles.

where λ is the wavelength of the light, n is an integer, and L is the mirror spacing of the etalon and typically $L \gg \lambda$. To transmit the light, the mirror spacing must then be $L = n\lambda/2$. The transmission profile of the etalon repeats for each mirror spacing satisfying this relation, given by

$$T = \frac{\tau_0}{1 + \left(\frac{4F^2}{\pi^2}\right) \sin^2\left(\frac{2\pi L}{\lambda}\right)}, \tag{1.38}$$

where τ_0 is maximum possible transmission with all losses in the system accounted for, F is the finesse of the etalon, which is determined by the reflectivity and flatness of the mirrors, L is the mirror spacing, and λ is the wavelength of light passing through the etalon. The frequency, or wavelength, spacing of the transmission maximums is known as the free spectral range (FSR), where

$$FSR_f = \frac{c}{2L}, FSR_\lambda = \frac{\lambda^2}{2L}. \tag{1.39}$$

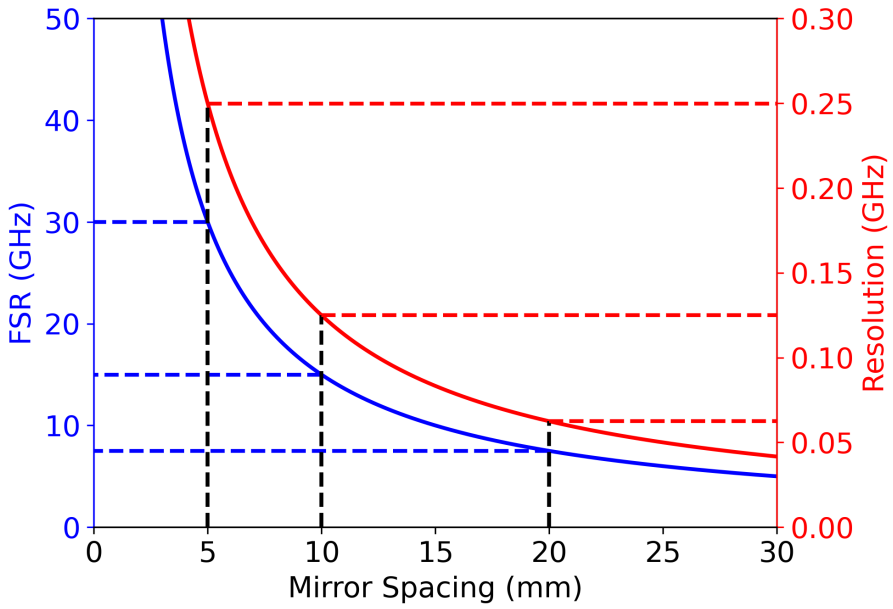

Figure 1.9: FSR and resolution of a Fabry-Pérot interferometer as functions of mirror spacing. Common mirror spacings are highlighted by the dashed lines.

The resolution of the interferometer is related to the FSR through

$$R = FSR_f/F, \tag{1.40}$$

where F is typically about 120. Fig. 1.9 shows the FSR and resolution as functions of the mirror spacing, with commonly used spacing highlighted by dashed lines.

If the interferometer were composed of only one etalon, the frequency of light transmitted could not be uniquely identified due to the repeating transmission profile. To overcome this, the second etalon is placed in series with the first with a slightly different mirror spacing. The ratio of the mirror spacings of the two etalons is held while scanning. This creates an overall transmission profile with only one main allowed frequency, as shown in Fig. 1.8. Small artifacts, called ghost peaks, are also present at the repetition frequencies for each etalon, but are dramatically reduced in amplitude due to the small overlap in the individual transmission profiles of the etalons at those positions.

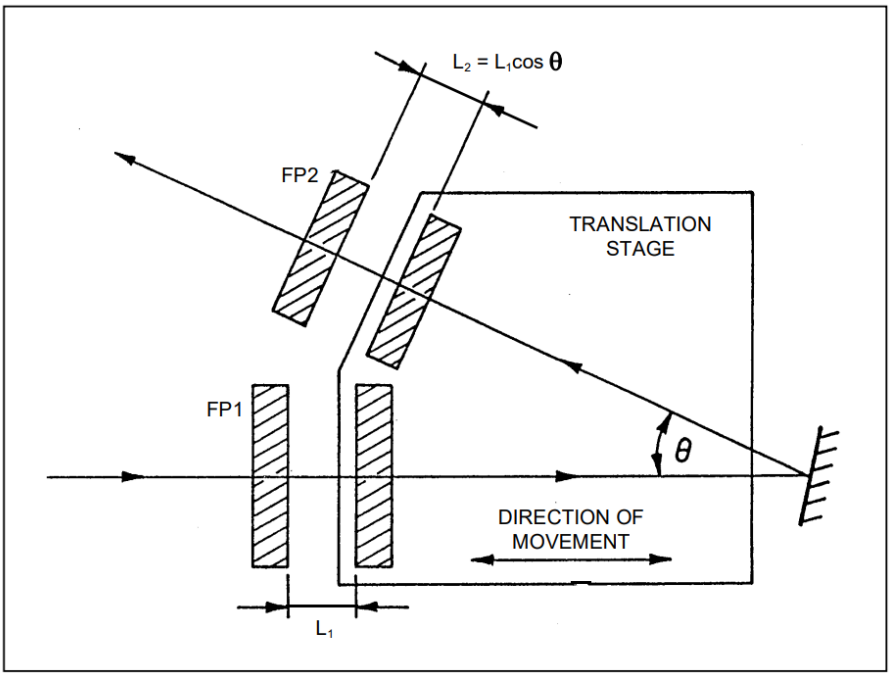

Figure 1.10: Geometry of the TFP2-HC scanning stage. A constant ratio of mirror spacing is held between the two etalons during a scan. Reproduced from Ref. [1]

To measure the full spectrum of the scattered light, the mirror spacing of the etalons are scanned in tandem. Due to the angle θ, shown in Fig. 1.10, held between the two beam paths, the second etalon mirror spacing is $L_2 = L_1' \cos\theta$, and $L_1' = L_1 + \Delta L$, where ΔL is the mirror displacement from the scanning. The overall transmission profile of the tandem interferometer is then

$$T_{tot} = \frac{\tau_0^6}{\left(1 + \left(\frac{4F^2}{\pi^2}\right)\sin^2\left(\frac{2\pi(L_1+\Delta L)}{\lambda}\right)\right)^3 \left(1 + \left(\frac{4F^2}{\pi^2}\right)\sin^2\left(\frac{2\pi(L_1+\Delta L)\cos\theta}{\lambda}\right)\right)^3} \tag{1.41}$$

where the exponents come from the three passes through each etalon. One mirror of each etalon is fixed to a scanning stage, which is then moved along the axis of the first etalon. The scanning range is typically in the range of hundreds of nanometers. Fig. 1.10 shows the geometry of the scanning apparatus. As the stage scans, the frequency of the light that can be transmitted changes, as shown for each of the individual etalons in Fig. 1.11. Here the term "BLS frequency" refers to the frequency difference between the scattered light and an unshifted reference beam of the probe laser. The magnitude of the BLS frequency is then the frequency of the wave (magnon or

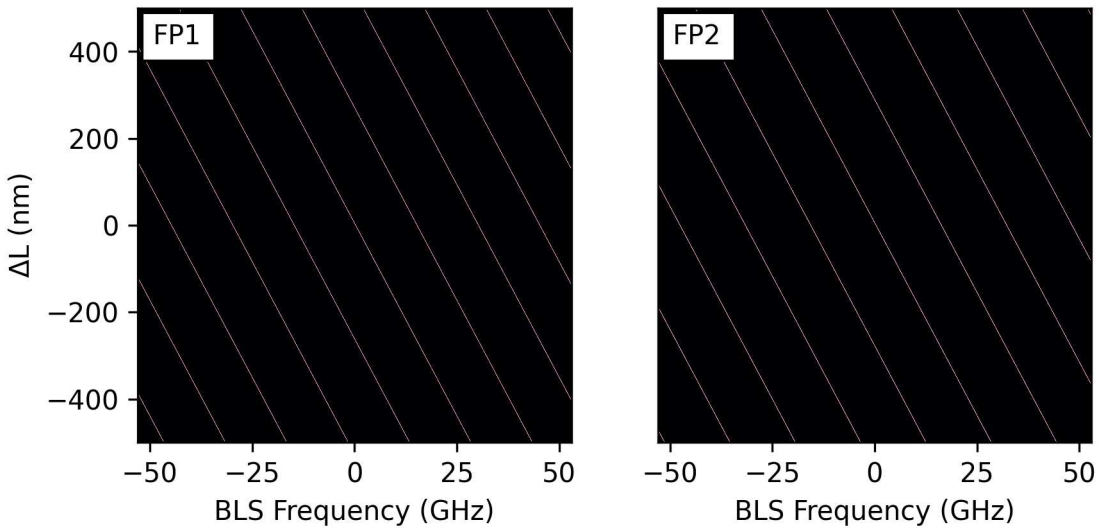

Figure 1.11: Transmission profiles for each of the etalons of the TFP2-HC interferometer during a scan, with mirror spacings of 10 mm and the frequencies plotted relative to the unshifted laser frequency. The black portions of the plot correspond to zero transmission, while the bright lines are the maximum transmission lines. The profiles are slightly offset one another and have narrow transmission lines.

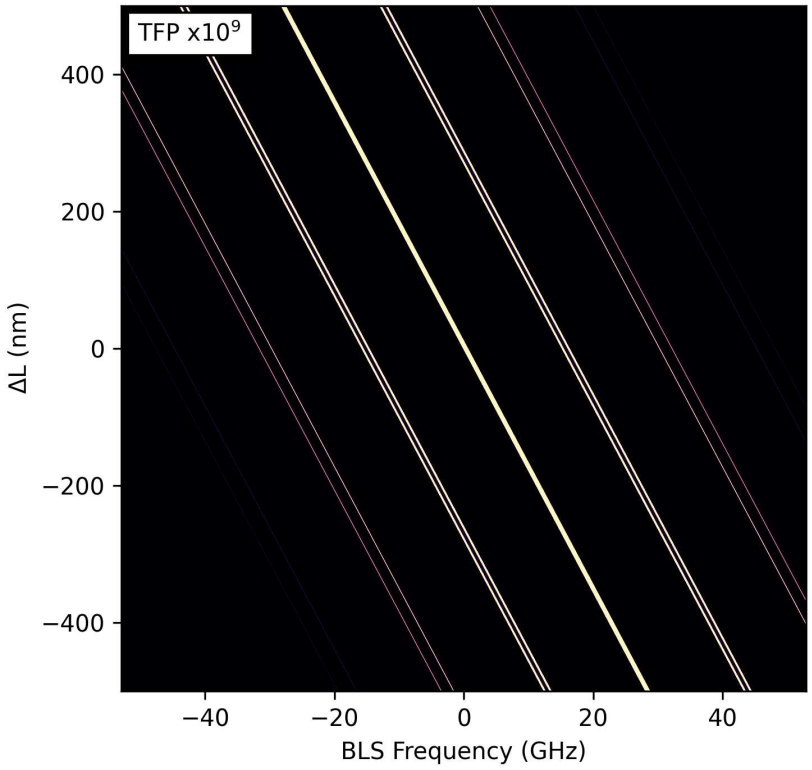

Figure 1.12: Overall transmission profile of the TFP2-HC, calculated using Eq. 1.41. A bright line is observed at the frequency shift (BLS frequency) that corresponds to the frequency of the light incident on the interferometer. This central transmission line is approximately $\times 10^7$ more intense than the first ghost peaks, $\times 10^9$ than the second set of ghost peaks.

phonon) from which the probe laser scattered, and the sign is determined by the type of scattering interaction, either the annihilation or creation of the scattering wave.

While light may transmit through the interferometer at more than one frequency, the contrast between the main transmission line and other frequencies is sufficient that at each scan position, the frequency measured is considered only the main transmission line. The extinction ratio, the ratio between the main transmission line and frequencies away from the main line and the ghost peaks, achieved by the interferometer is better than 10^{10}. Additional light is transmitted at the ghost peak frequencies, the secondary lines shown in Fig. 1.12, is suppressed by 7 orders of magnitude relative to the main frequency. In most cases, the only ghost peaks that are strong enough to be observed are those that are associated with the elastically scattered light. Additional ghost peaks at the higher repetitions also appear, but the higher order ghost peaks are suppressed by 9 orders of magnitude.

Scattering Geometries

There are several common BLS geometries used in experiments. These include the conventional geometries for backward scattering [19, 54], forward scattering [55, 56], and the micro-BLS technique [57, 58]. Each of these techniques provides different information that will be detailed below. In addition to the scattering geometry, techniques that provide additional information such as low temperature BLS and time-resolved BLS (TR-BLS) will be discussed.

A conventional BLS experiment is designed as follows: a narrow linewidth (about 10 MHz) continuous-wave (CW) laser source is focused onto a sample. The scattered light is collected and passed through an interferometer to a photodetector. The interferometer functions as a frequency discriminator, as discussed previously, allowing only a single frequency of light to pass through at a time, while the photodetector records the intensity of the transmitted light. The difference between the backward scattering and forward scattering geometries stems from how the scattered light is collected.

In a backward scattering configuration, the light the incoming and scattered light are at 180° with respect to one another, meaning the scattered light travels along the same axis as the incident

light but in the opposite direction. This light is collected by the sample lens. From conservation of momentum, the measured wavevector can be related to the angle of incidence of the light. The incident light only couples the component of light in the plane of the sample. Through a judicious application of the law of cosines, the measured wavevector is found to be

$$q = 2k_i \sin\theta. \tag{1.42}$$

With a laser source of $\lambda = 532$ nm, and an experimentally achievable range of angles from 5°-75°, wavevectors along the range $q = 2 - 23$ rad/μm can be measured. Issues arise with the precise understanding of the angle of incidence at small θ, as the wavevector will change rapidly with small changes in θ, and at large θ the amount of light coupled to the sample becomes small enough that the signal-to-noise ratio becomes an issue.

In a forward scattering configuration, the laser beam passes through the sample, the forward scattered light is collected with an additional lens, and is then being passed to the interferometer. In contrast to backward scattering, this geometry does not have any wavevector selectivity; all wavevectors up to a maximum value defined by the collection angle of the lens are measured. While the wavevector selectivity is lost, this geometry allows for the detection of waves with very small wavevectors that would require too small an angle of incidence in the backscattering geometry to observe. An additional caveat to this technique is that the sample must be transparent, as the light must pass through the sample to be collected. While this may prevent many materials from being measured, this scattering geometry has a much higher signal intensity than backward scattering for transparent materials.

The forward scattering geometry is typically used in driven experiments, where waves are excited with transducers, such as a stripline antenna for spin waves or interdigitated transducers (IDTs) for phonons. The excitation method can allow for the reintroduction of wavevector selectivity. Beside the excitation method, wavevector selectivity can also be reintroduced through the use of apertures in the beam path [55].

Time-resolved BLS (TR-BLS) can be used in conjunction with a driven experiment, where the temporal information is constructed by time-of-flight. In this technique, the waves are generated by the excitation method of choice, such as a stripline antenna with a CW microwave source gated by a microwave switch, and the start of the excitation is initiated by a trigger signal. The same trigger signal is used to trigger a fast time-of-flight card that bins all photons hitting the photodetector in time relative to the arrival of the trigger signal. As this method spreads the BLS signal over many time bins, the experiment must be repeated many times to achieve a reasonable signal-to-noise ratio for each time bin. This technique can achieve a time resolution of 250 ps with the electronics used in this work. Pairing TR-BLS with a spatial scan of the sample allows one to generate a movie of the waves passing through the sample, and allows for the extraction of detailed time and spatial information.

The micro-BLS technique uses a microscope objective. The objective focuses the laser light to a diffraction limited spot size of only a few hundred nanometers. The micro-focus BLS configuration provides the best spatial resolution achievable in BLS, while also increasing the signal to noise ratio due to an increase laser power density. Additional optics to introduce focus stabilization are required to compensate for drift of the sample position. A detailed discussion of the micro-BLS technique and instrumentation can be found in Ref [59].

As an offshoot of the conventional backward scattering geometry, low temperature BLS has an identical scattering geometry, simply with the addition of a cryostat to cool the sample. The cryostat used in this work is a Montana Instruments Cryostation with Magneto-Optic module, which enables measurements from room temperature down to 5 K. It uses a dry helium compressor to cool the sample, with an electromagnet in place to allow an applied field up to $\mu_0 H = 730$ mT. In practice, 10 K is the lowest consistently achievable temperature with the use of internal radiation shielding in the sample chamber. Attocube piezoelectric positioners are used to position the sample within the chamber.

Cooling the sample adds additional experimental considerations, as spot heating from the laser becomes important to consider. While the laser will heat the sample at the focus spot at any tem-

perature, at low temperatures the decreased heat capacity of the sample allows the laser power to appreciably change the spot temperature relative to the surrounding sample. In this work, a variety of incident laser powers were used to determine an effective laser power to use that balances data collection times with the additional temperature uncertainty added by the spot heating. Collection times for low-temperature BLS increase by up to an order of magnitude for a given laser power, due to the decreased population of spin waves at lower temperatures, and then the signal level decreases further with decreasing laser power.

BLS Spectra

A typical BLS spectrum of a surface spin wave is show in Fig. 1.13, collected in the backscattering geometry for a [1.5/1.5/1] nm W/Pt/Co film with an applied field of $H = 1500$ Oe. The spectrum shows, from left to right, the ghosts peaks discussed above, the Stokes signal for a surface wave, the elastic region with the reference peak, the anti-Stokes signal, and the other set of ghost peaks. The ghost peaks are not always safe to measure, since they may have enough power to damage the photodetector, but may be measured for this sample since a backscattering configuration is used and the sample is very reflective. The Stokes signal corresponds to scattered light shifted down in frequency due to the creation of a spin wave, while the anti-Stokes signal is shifted up in frequency from annihilating a spin wave.

From an individual scan, we can extract the spin wave frequency for a given wavevector. By changing the angle of incidence, the spin wave dispersion relation can be mapped by changing the measured wavevector as shown in Eq. 1.42.

1.2.2 Magnetometry

Magnetometry is a cornerstone tool in the study of magnetism and magnetic materials in which the magnetization response under an applied field is measured. A wide range of properties in magnetic films may be inferred from this response, such as the saturation magnetization, coercivity, magnetic remnance, magnetic anisotropy strength and direction, and the temperature dependence of the magnetization and anisotropy [60].

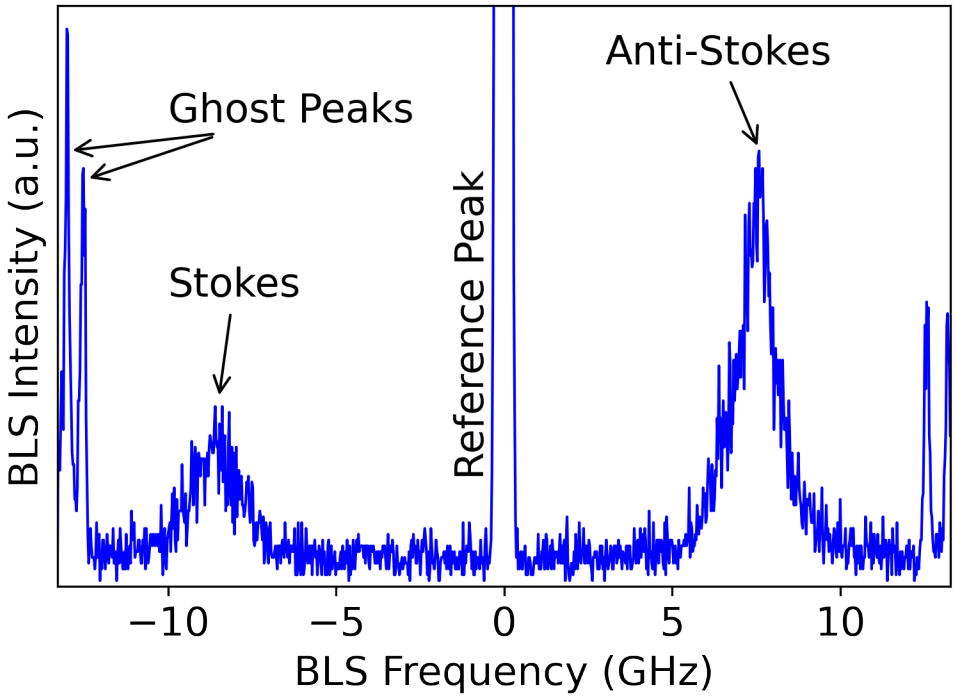

Figure 1.13: A typical BLS spectrum of a surface spin wave, measured in the backscattering geometry for a [1.5/1.5/1] nm W/Pt/Co film with an applied field of $H = 1500$ Oe. The Stoke, Anti-Stokes, and Ghost peaks are labeled. The central reference peak corresponds to the pure laser frequency and all frequencies are measured relative to it.

Magnetic hysteresis

As discussed previously, there are a variety of competing energies and anisotropies in magnetic materials. The short range order of the system is dominated by the exchange interaction, which for ferromagnetic materials aligns neighboring moments, while the long range order is determined by the dipole-dipole interactions. In order to minimize the dipole-dipole interaction energy of the system, domains form in magnetic materials. These domains are regions where the moments are pointing in the same directions, and the boundaries between domains where the magnetization changes direction are known as domain walls. Applying a magnetic field to the system creates an energetically favorable direction for the domains to align. As the magnitude of the applied field increases, the domains oriented along the field grow and the other domains shrink, until there is a single domain remaining. When only one domain is present, the film is considered saturated, as the magnetization is at the maximum achievable by the film.

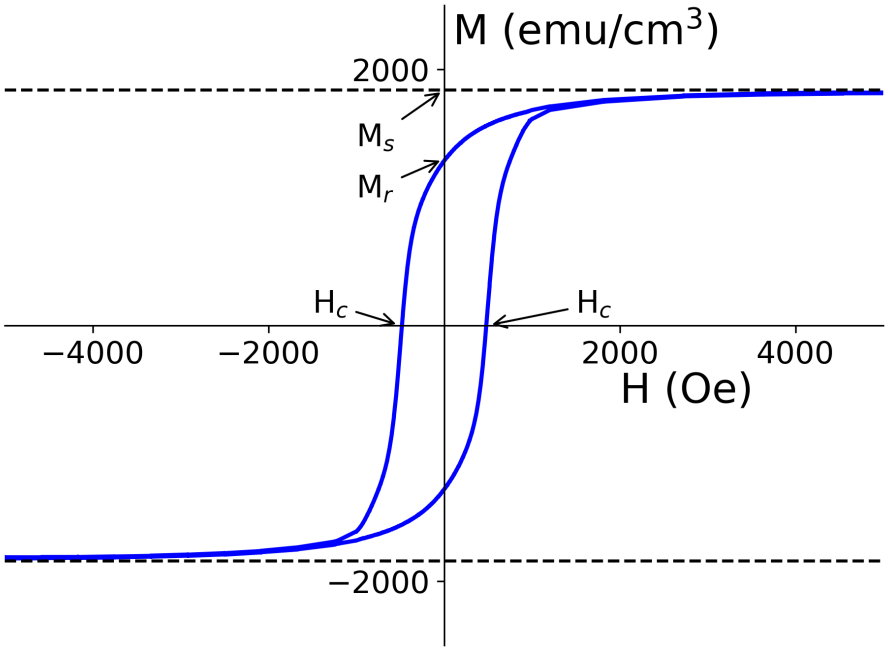

Figure 1.14: An in-plane hysteresis curve for a 1 nm Co/Pt film measured at 10 K. The saturation magnetization, coercivity, and remanence are labeled.

A full reversal process, where a saturated film has its magnetization direction reversed and saturated in the opposite direction, then back again, is known as a hysteresis loop. Typically shown as an $\boldsymbol{M}$ vs. $\boldsymbol{H}$ curve, the hysteresis loop contains information on the magnetic properties of the sample. A hysteresis loop, measured in-plane for a [1/1.5] nm Co/Pt film at 10 K, is shown in Fig. 1.14. The saturation magnetization, $\boldsymbol{M}_s$, is determined by the point where the magnetization stops increasing with additional applied field. The magnetic remnance, $\boldsymbol{M}_r$, is the magnetization remaining at zero field after the sample had been saturated. The coercivity, $\boldsymbol{H}_c$, is the field required to reverse the direction of the magnetization, shown as the horizontal intercepts of the hysteresis loop.

In the parlance of the magnetic materials community, the "easy-axis" is the preferred direction of the magnetization, while the "hard-axis" is the energetically unfavorable direction. These directions are set by the anisotropies present in the sample, which for thin films are typically the shape anisotropy and interfacial anisotropies. The shape anisotropy promotes an in-plane easy axis, as it aligns the moments tip to tail in the plane of the film and minimizes the dipole-dipole energy.

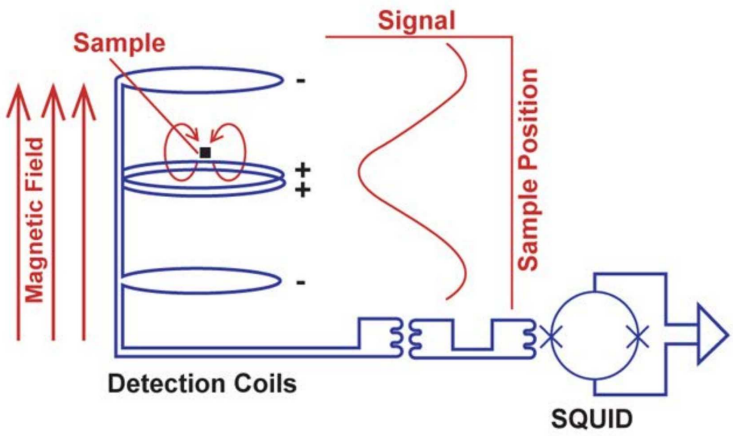

Figure 1.15: DC SQUID magnetometer scan and detection geometry for the MPMS3 magnetometer, shown in [2]

The sign and magnitude of the interfacial anisotropy depends on the materials across the interface, as well as the quality of the interface. In materials with large spin-orbit coupling (SOC), such as heavy metals like Pt, the interfacial anisotropy usually promotes an out-of-plane easy axis, and the material is said to have perpendicular magnetic anisotropy (PMA). The strength of the anisotropy may be determined by the area between hysteresis loops measured in- and out-of-plane for a thin film, or estimated by the field required to saturate the sample.

The magnetometer

The primary instrument for magnetometry is the magnetometer. At its most basic, the magnetometer consists of a method to apply a uniform magnetic field, a method of moving the sample to create a changing magnetic flux, and pickup coils to generate a voltage from that changing flux through Faraday's law of induction.

The applied field can be from either a conventional electromagnet or, for low temperature and high field measurements, a superconducting magnet. Conventional electromagnets are able to change fields quickly through changing the applied current for fast measurement times, while the maximum field achievable, typically around 2 T for conventional magnetometers [61], is limited by resistive heating. Superconducting electromagnets cannot change fields quickly because the current injection process is slow as compared to conventional electromagnets, but the lack of re-

sistive heating allows them to achieve much higher fields, up to 7 T for the MPMS3 magnetometer used in this work [2].

The motion of the sample to introduce a changing flux is achieved in two main ways: vibrating the sample and scanning the sample. The vibration of the sample is the basis of the Vibrating Sample Magnetometer (VSM). With a vibrating frequency around 40 Hz, the VSM uses lock-in amplification to detect and amplify the induced current signal [2, 61]. The induced signal is fit with an analytical function to extract the overall magnetic moment of the sample. The MPMS3, in contrast, uses a superconducting quantum interference device (SQUID) to amplify the induced signal. The setup used for the direct current (DC) scan is shown in Fig. 1.15, where the sample is moved at a constant rate through a set of counter-wound detection coils. Assuming that the sample dimensions are much smaller than the detection coils, the resulting induced voltage versus position function, typically "sombrero" shaped, can be fit to extract the magnetic moment of the sample. The benefit of the DC SQUID method is to increase the dynamic range of the detection circuit, which increases the sensitivity, and negates any need for RF signals in the system. The DC scan is repeated three times per temperature or field and the average of these measurements is reported. By repeating the measurements and averaging, the overall uncertainty in the sample's moment may be reduced.

The magnetometry performed in this work used a Quantum Design MPMS3 SQUID magnetometer. This magnetometer has exquisite sensitivity down to 10^{-8} emu, or 10^{-11} Am^2. It is also able to attain a base temperature of 1.8 K for low temperature measurements [2]. Measurements in this work were made both using the VSM mode and the DC scan mode.

For a measurement, the sample is mounted either on a quartz rod or inside a plastic straw, depending on the sample orientation. The quartz rod has a flat face for mounting the sample for in-plane measurements. The plastic straw was used to mount the samples perpendicular to the magnetic field. The magnetometer is sensitive to any material within the pickup coils that is non-uniform within the coils, as this non-uniformity will result in a changing magnetic flux. The quartz rod and plastic straw are chosen to minimize the additional moment detected by the magnetometer.

For the quartz rod, the GE-varnish used in mounting the sample must also be applied per sample, as old adhesive that accumulates dust can introduce an erroneous signal of similar magnitude to low moment samples [62]. The volume of the sample is measured using the nominal thickness from deposition and surface area found using an optical microscope.

1.2.3 Microwave characterization

Microwave characterization techniques are used to understand the spin wave transmission characteristics of samples and devices, such as the formation of band gaps where transmission is suppressed in magnonic crystals [63–66]. In this work, the microwave measurements consist of exciting spin waves with a stripline antenna at one end of a magnonic crystal, a crystal in which magnetic properties are periodically modulated, and detecting the transmission of spin waves across the crystal with another antenna. Here we will present the basics of the excitation scheme and the instrumentation used.

Spin wave excitation

Spin waves were excited in this work using a rectangular profile stripline antenna. The applied RF current in the antenna generates a uniform RF field across the sample. The field is considered uniform as the electric field wavelength ($\lambda_{RF} = c/n\nu_{RF}$) is much longer than sample width when in the conductor. The uniform field provides a torque on the magnetization, driving the system at the RF frequency. Driving the system in this manner excites spin waves that propagate away from the antenna.

Which spin waves are excited by the antenna and at what relative efficiency is determined by the wavevectors the RF magnetic field of the antenna can couple to. For a rectangular stripline antenna with width w in the $\widehat{x}$-direction, thickness t in the $\widehat{z}$-direction, current I flowing in the

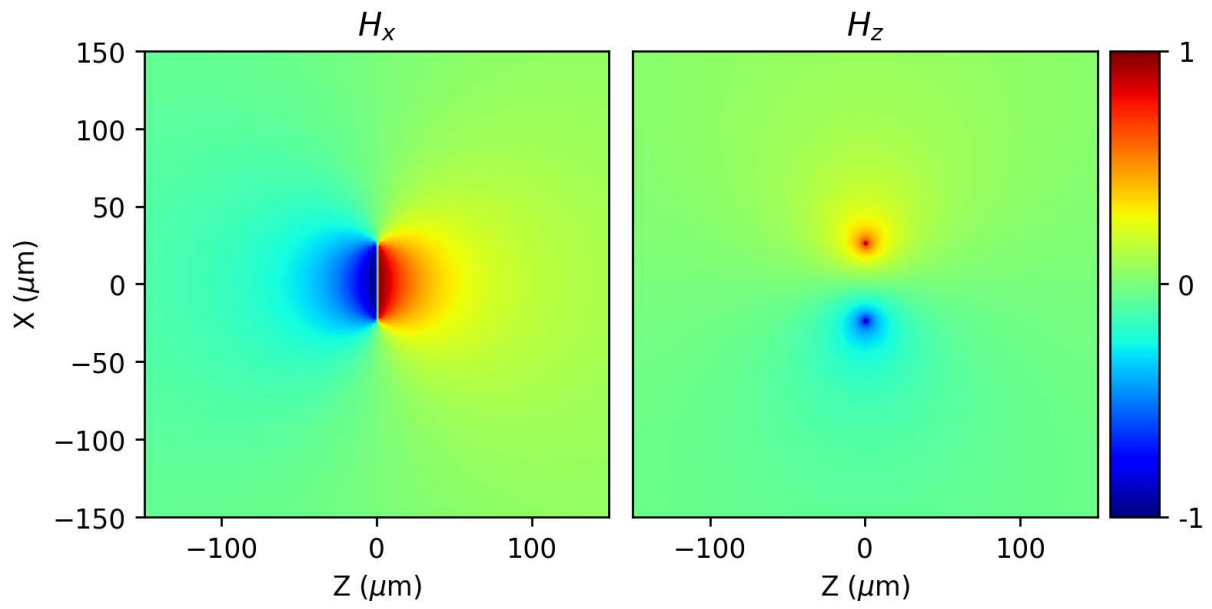

Figure 1.16: Normalized magnetic field components excited by a current in a rectangular stripline antenna of width $w = 50$ μm and thickness $t = 2$ μm.

$\widehat{y}$-direction, the magnetic field components are given by

$$H_z = \frac{2\mu_0 I}{16\pi ab}(-(x-a)\tan^{-1}\left(\frac{z-b}{x-a}\right) + (x+a)\tan^{-1}\left(\frac{z-b}{x+a}\right) - ...$$
$$\frac{1}{2}(z-b)\ln\frac{(z-b)^2+(x-a)^2}{(z-b)^2+(x+a)^2} + (x-a)\tan^{-1}\left(\frac{z+b}{x-a}\right) - (x+a)\tan^{-1}\left(\frac{z+b}{x+a}\right) + ...$$
$$\frac{1}{2}(z+b)\ln\frac{(z+b)^2+(x-a)^2}{(z+b)^2+(x+a)^2}) \quad (1.43)$$

$$H_x = -\frac{2\mu_0 I}{16\pi ab}(-(z-b)\tan^{-1}\left(\frac{x-a}{z-b}\right) + (z+b)\tan^{-1}\left(\frac{x-a}{z+b}\right) - ...$$
$$\frac{1}{2}(x-a)\ln\frac{(z-b)^2+(x-a)^2}{(z+b)^2+(x-a)^2} + (z-b)\tan^{-1}\left(\frac{x+a}{z-b}\right) - (z+b)\tan^{-1}\left(\frac{x+a}{z+b}\right) + ...$$
$$\frac{1}{2}(x+a)\ln\frac{(z-b)^2+(x+a)^2}{(z+b)^2+(x+a)^2}), \quad (1.44)$$

where $a = w/2$, and $b = t/2$. The fields described by these equations are shown in Fig. 1.16 for a stripline with $t = 2$ μm and $w = 50$ μm. For an antenna above a thin film, this field appears uniform both across the width of the film as discussed before, but also through the depth. The

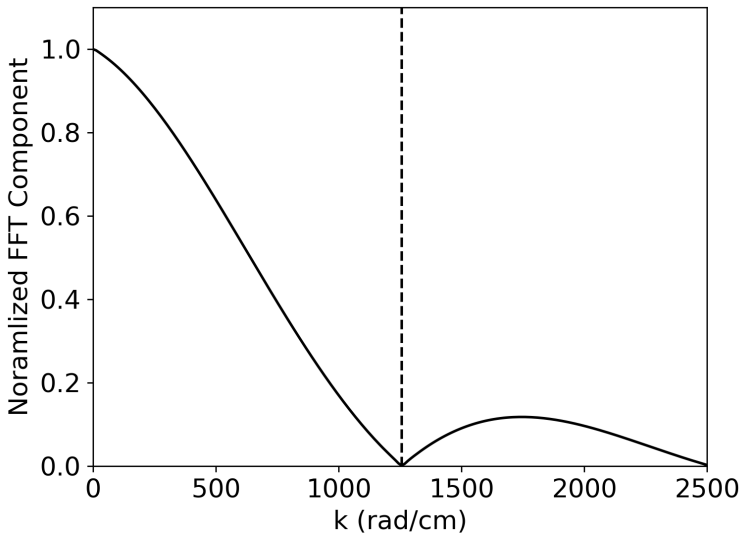

Figure 1.17: Normalized Fourier components of the field excited by a stripline antenna 1 μm above the antenna. The antenna has width $w = 50$ μm and thickness $t = 2$ μm.

region where spin waves may be excited by this field is limited to the region less than 50 μm from the antenna.

A cut in the 2D Fourier transform of the field is shown in Fig. 1.17, showing the wavevector components of the field. These wavevectors correspond to the spin wave wavevectors that the field can efficiently couple to. The amplitudes of the Fourier components are normalized to show the relative amplitude at each wavevector. The cutoff wavevector, where the component amplitude goes to zero, occurs at $k = 2\pi/w$ where the wavelength is the width of the antenna.

In this work, all driven measurements are carried out in samples that are confined laterally. As a consequence of this confinement, when driving at a fixed frequency, many width-quantized modes are excited. Since the driving field is uniform across the width of the sample, only modes that are symmetric, and have non-zero width-averaged magnetizations, across the width are excited [67]. The mode amplitudes scales as $\propto 1/n$, where n is the mode number. The excited modes have slightly different wavevectors, as they have different dispersion relations, and propagate at different group velocities. The resulting interference patterns between these modes are complex and change with the excitation frequency, applied field, sample width, and field angle.

Microwave instrumentation

All microwave characterization measurements conducted in this work used an Agilent Model E8361A General Purpose Network Analyzer (PNA) in conjunction with an applied field from an electromagnet. The PNA is capable of acting as both microwave source and receiver in a measurement, allowing it to measure the transmitted and reflected microwave signals from a device. In this work, the PNA was primarily used to measure the spin wave transmission. The electrical microwave signals were converted to spin waves, and from spin waves to electrical signals, by stripline antennas, as mentioned in the previous section.

Spin wave transmission profiles were measured using the PNA to determine transmission losses through magnonic crystals as a function of frequency, typically in the GHz range. Due to the excitation and detection mechanisms, the transmission profiles measured are averaged across the width of the crystals. The microwave measurements are useful to quickly determine transmission characteristics of a magnonic crystal, while TR-BLS may be used in conjunction to provide detailed information about spin wave propagation and the origin of transmission characteristics that cannot be extracted from the microwave measurements.

Chapter 2

The importance of two dimensional behavior of spin waves in a 1D magnonic crystal

2.1 Context

This chapter consists of the paper *The importance of two dimensional behavior of spin waves in a 1D magnonic crystal*, a manuscript under preparation.[1]

The supplemental information is shown in section A.2. This work aimed to observe the formation of band gaps in a 1D magnonic crystal in time as a spin wave pulse propagated through the crystal. The formation was demonstrated, and complex interference patterns were observed in the spin wave pulses that changed with the spin wave frequency. We provided a framework to calculate these interference patterns from the spin wave dispersion relation, as well as to model the effect of reflections in a 1D magnonic crystal on the spin wave propagation pattern.

2.2 Paper Summary

Here we report detailed time-resolved Brillouin light scattering (TR-BLS) measurements of a 1D yttrium iron garnet (YIG) magnonic crystal in the magnetostatic surface wave geometry. Microwave measurements confirm that periodic grooves etched into the YIG film (20 grooves of width $w = 25$ μm, depth 3.5 μm, and center-to-center spacing of $d = 275$ μm) create band gaps that suppress the transmission of spin waves by $>$15 dB, and these band gaps are also observed by BLS. The TR-BLS measurements provide direct insight into the temporal and spatial evolution

[1]Author list: Mitchell S. Swyt, Lia Compton, César L. Ordóñez-Romero, Giuseppe Pirruccio, H. J. Jason Liu, and Kristen S. Buchanan. The magnonic crystal was patterned by César L. Ordóñez-Romero and Giusseppe Pirruccio (Universidad Nacional Autónoma de México). All Brillouin light scattering, microwave, and profilometry measurements were made by Mitchell S. Swyt. Lia Compton assisted in setting up the time-resolved Brillouin light scattering apparatus. Interference pattern calculations were made by Mitchell S. Swyt and Kristen S. Buchanan. The paper was written and edited by Mitchell S. Swyt, Kristen S. Buchanan, H. J. Jason Liu, César L. Ordóñez-Romero, and Giuseppe Pirruccio.

of propagating spin wave packets as they travel through the magnonic crystal, and these measurements highlight the importance of the 2D nature of the spin wave propagation in this configuration. The temporal aspects of the spin wave interference are also directly observed.

2.3 Research Article

2.3.1 Introduction

Magnonic crystals are created by introducing a periodic modulation of the material properties that leads to the formation of bands of allowed frequencies where spin waves can pass through the crystal and band gaps where propagation is suppressed. Analogous to photonic crystals in optical devices, magnonic crystals show promise for signal processing and logic applications [6, 7, 9, 10, 68] and concepts drawn from optics have inspired advances in magnonics, for example, steering spin waves using non-uniform effective internal magnetic fields [69]. Magnonic devices also have potential as hybrid interconnects for quantum computing where magnetic excitations in patterned materials offer potential to couple a single magnon mode to the spin state of a nitrogen-vacancy center qubit [70], to manipulate entangled qubit states [71], and to encode and interact with information in the spin domain [72, 73]. The scalability for magnon based devices is promising because the wavelength of spin waves is much shorter than that of light at the same frequency, which will facilitate scaling down to the nanoscale regime [5, 10, 74].

YIG has long been the material of choice for prototype magnonic and spintronic devices due to its low damping and long spin wave attenuation lengths. YIG magnonic crystals have been studied in a variety of geometries, where the simplest configuration is the 1D magnonic crystal where the magnetic properties are periodically modulated along one dimension, usually in the form of an array of evenly spaced grooves or stripes of different materials [63–66]. The periodic modulation of the magnetic environment leads to the formation of band gaps. The transmission profiles of YIG magnonic crystals have been measured in the backward volume (BV) and magnetostatic surface spin wave (MSSW) configurations where the magnetic field is applied in-plane along the direction of travel and perpendicular to the direction of travel, respectively. Tuning the geometry of the

magnonic crystal, such as the groove spacing, size, and depth, as well as the choice of magnetic materials, alter the transmission characteristics [75, 76], where the length scales of magnonic crystals range from the micrometer scale [63–66] down to the nanoscale [75]. One of the unresolved puzzles in the field is that magnonic crystals measured in the BV configuration show a larger band gap rejection efficiency (up to 600 times larger) as compared to the same crystals measured in the MSSW configuration [63]. The MSSW configuration, however, offers advantages over the BV configuration, so finding strategies to improve the rejection efficiency of a 1D MSSW magnonic crystal is important. The MSSW configuration offers faster group velocities [74] and higher excitation efficiencies as compared to BV configuration. MSSWs are also non-reciprocal, and while this is somewhat of a disadvantage for devices based on multiple reflections, it can be advantageous for some applications [63, 64, 77]. Further, the MSSW configuration also allows for the introduction of interfacial Dzyaloshinskii-Moriya interactions that provide an additional method of tuning the band structure of nanoscale magnonic crystals [78]. For these reasons it is important to understand the nuances of how 1D magnonic crystals work in the MSSW configuration.

Models of magnonic crystal behavior in a 1D magnonic crystal are predominantly 1D in nature. A simple model where the periodic defects are treated as 1D Bragg reflectors provides a conceptual picture of the principles of operation. This approach predicts that spin waves with wavevector $k = n\pi/d$, where d is the center-to-center groove spacing and n is an integer band gap number will be suppressed due to destructive interference, and has also been used to obtain phenomenological estimates of the spin wave transmission characteristics [66]. Approaches involving reciprocal-space solutions to the Landau–Lifshitz–Gilbert equation have also been used to model magnonic crystals [79], mainly to obtain the band structure and standing wave mode profiles [80–82]. Modeling of the time-resolved propagation of a spin wave pulse through a 1D crystal, and the 1D modeling that has been done shows that a standing wave pattern is expected to form at the band gap frequencies but that it takes time for this pattern to develop [75]. A common theme in magnonic crystal modeling is that the dimensionality of the solution is matched to the dimensionality of the magnonic crystal.

Here we use time-resolved Brillouin light scattering (TR-BLS) to obtain detailed spatial maps of the propagation of spin wave pulses through a 1D magnonic crystal in the MSSW configuration. Magnonic crystals are commonly characterized using microwave measurements, which yield a width-averaged response at the location of the output antenna, and the models for the transmission characteristics use simple 1D models to estimate the transmission as a function of frequency [66]. TR-BLS provides detailed time and spatial information and has been used to probe a variety of magnon processes including nonlinear spin wave self-focusing effects [83], the time-evolution of nonlinear three magnon processes [84], and Bose Einstein condensates of magnons [85, 86]. Our TR-BLS measurements show that although the structure of the crystal is 1D, the spin wave intensities show complex 2D patterns that agree well with calculations that take into account not just the reflections from the 1D grooves but also the width quantization of the spin wave modes. Furthermore, these measurements suggest that width-quantized modes, if not considered carefully in the design of the magnonic crystal, may significantly reduce the obtainable rejection efficiencies.

2.3.2 Experimental Methods

Microwave and time-resolved BLS measurements were made on a magnonic crystal made of YIG, where YIG was chosen because of its low damping and long spin wave propagation distances. A schematic of the experimental setup is shown in Fig 2.1a). A 6.4 μm-thick, $l = 2.25$ mm-wide, yttrium iron garnet (YIG) film on a gallium gadolinium garnet (GGG) substrate was patterned with 20 grooves with widths of $a = 25$ μm and depths of 3.5 μm separated by a $w = 250$ μm flat region, giving an overall center-to-center spacing of $d = 275$ μm. The grooves were chemically etched into the film using hot orthophosphoric acid. The profile of the grooves, measured via profilometry, is shown in Fig 2.1b).

Two 50 μm wide stripline antennas were placed approximately 10 mm apart, one ahead of the patterned region to excite spin wave pulses propagating through the crystal, and one after the patterned region to detect the spin waves for transmission measurements made using a vector network analyzer. An external bias field of $H = 865$ Oe was applied in the plane of the film

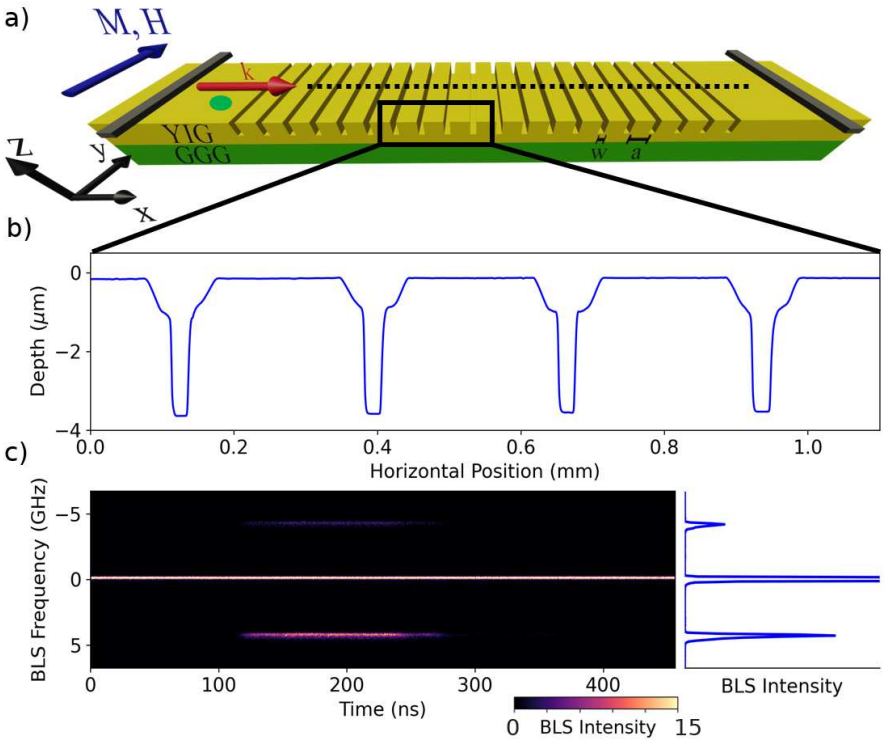

Figure 2.1: a) Diagram of the magnonic crystal. The YIG film (yellow) on a GGG substrate (green) has 20 grooves of width $w = 25$ μm and depth 3.5 μm with a center-to-center spacing of $d = 275$ μm. The magnetic field H is applied along the y direction, perpendicular to the long axis of the crystal (MSSW configuration) and spin wave pulses are excited by a stripline antenna (grey). b) The measured profile of the etched grooves. c) A TR-BLS spectrum (left) showing the spin wave pulse, and the corresponding time integrated signal (right), measured at the position marked by the green dot in a) with $H = 865$ Oe and a driving frequency $f = 4.25$ GHz.

in the magnetostatic surface spin wave (MSSW), or Damon-Eshbach, configuration. Microwave measurements were made to obtain the frequencies response of the 1D magnonic crystal, and time- and spatially- resolved Brillouin light scattering measurements [83] were made at selected frequencies to obtain detailed spatial and temporal information on spin wave propagation through the crystal. The TR-BLS measurements were made in the forward scattering geometry. A 200 ns microwave was pulse applied at the input antenna to excite a spin wave pulse, created using a microwave source and gated microwave switch triggered by a delay generator. A microwave power of 4 dBm was used, with a pulse repetition rate of 1.2 ms, chosen to ensure that the sample response is in the linear regime and to minimize sample heating, respectively. The sample response was

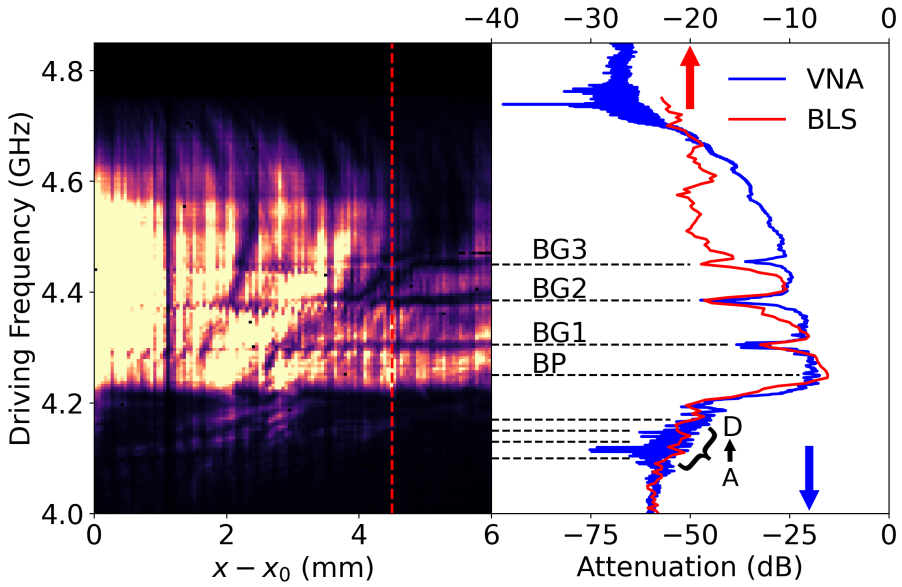

Figure 2.2: Comparison of BLS measurements at various driving frequencies and microwave measurements. (left) Time integrated BLS measurements as a function of frequency and position along the central axis of the magnonic crystal (shown as a dashed line in Fig 2.1a). (right) Comparison of microwave transmission measurements (blue line, measured between the left and right antennas in Fig 2.1a) and the ratio of BLS intensities measured at $x - x_0 = 4.3$ mm (red dashed line) and at $x - x_0 = 0$ are shown in red. Band gaps (BG1, BG2, and BG3) are observed in the BLS and microwave measurements.

scanned over the sample in a square grid pattern with a grid spacing of 50 μm and the inelastically scattered light, which is sensitive to the spin wave excitations, was analyzed using a TFP2-HC tandem Fabry-Perot interferometer with a mirror spacing of 10 mm. A fast time-of-flight card was used to bin the photons striking the photodetector in 250 ps time bins.

2.3.3 Results

A comparison of BLS measurements along the central axis of the crystal to microwave measurements is shown in Fig 2.2.

Dark horizontal stripes in the BLS measurements are observed at the band gap frequencies, corresponding to extinction of the SW density as the pulse propagates through the crystal. Band gap formation in the BLS measurements is observed at $f = 4.305$, 4.38, and 4.455 GHz. Vertical dark arc features, such as the feature starting at $x - x_0 = 2$ mm, are observed in the BLS measurements and do not have a corresponding feature in the microwave measurements. The dark

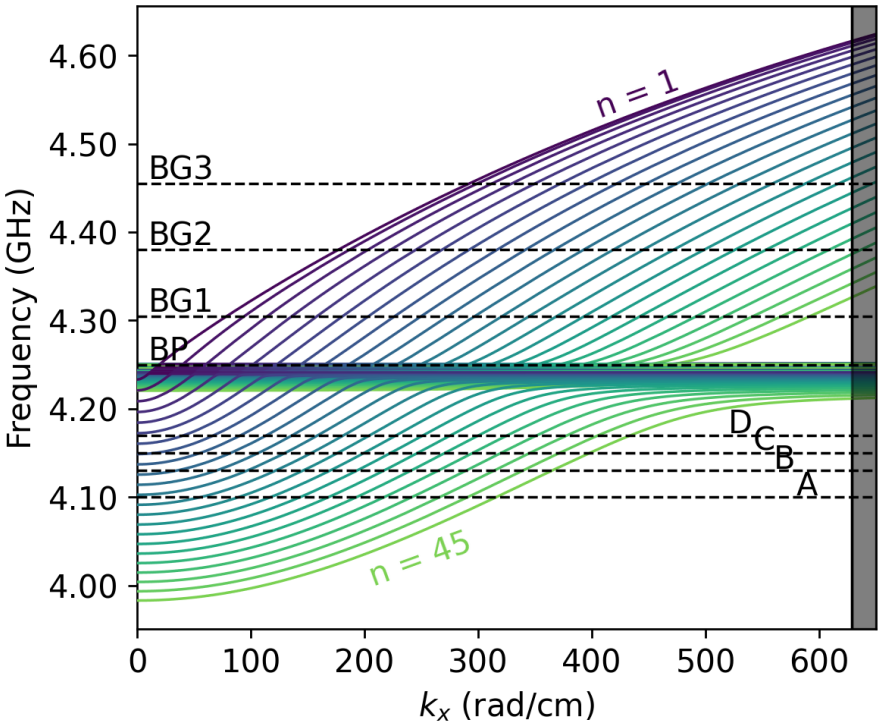

Figure 2.3: Calculated dispersion relations for the first 45 odd width-quantized modes. Spatial scans were measured by BLS at the frequencies marked by dashed lines above FMR (BP, BG1, BG2, BG3 in Fig 2.4 and below FMR (A, B, C, D in Fig 2.5. The unshaded (shaded) regions indicate the wavevector ranges over which the antenna efficiently (inefficiently) excites spin waves.

vertical line at $x - x_0 = 1.1$ mm is due to a scratch in the GGG substrate, confirmed with an optical microscope. The stripline transducer inherently averages over the width of the crystal and therefor the microwave measurements do not provide any information about the 2D nature of the spin wave pulse. Differences in the attenuation in the BLS measurement compared to the microwave measurement are due to insertion losses of the stripline excitation and detection. In addition to the spin wave density above the ferromagnetic resonance (FMR) frequency, spin wave density is observed below FMR. These modes originate from width quantized modes shifted down in frequency with respect to the uniform mode.

To understand what waves will be present at a given frequency, as well as how they will propagate, we turn to the dispersion relation for the system. Shown in Fig 2.3, the first 45 width quantized modes were calculated using the matrix method described in [45]. The full dispersion

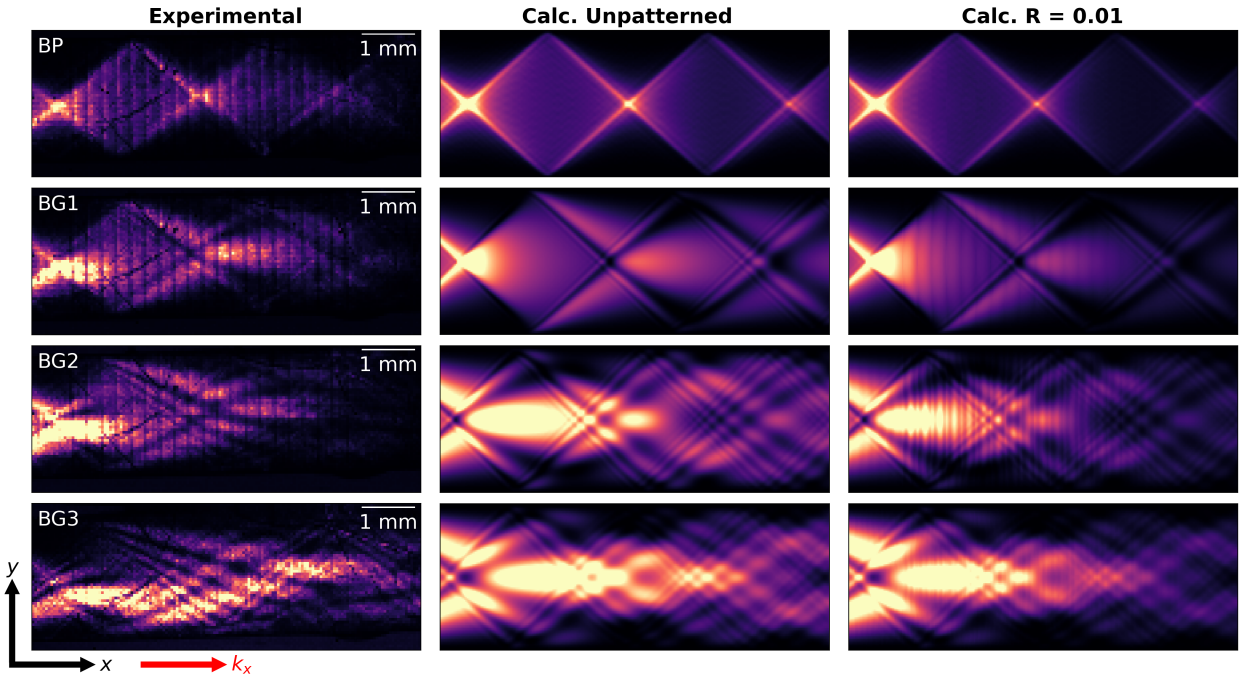

Figure 2.4: Two-dimensional maps of the spin wave propagation, where the scan region begins at $x_0 = 1$ mm away from the edge of the antenna. The columns show, from left to right, BLS measurements, calculations with no reflections ($R = 0$), and calculations with reflections ($R = 0.01$), and the rows correspond to the frequencies marked in Fig 2.2 (BP, BG1, BG2, BG3).

surface for an unpatterned infinite film was first calculated, then cuts along the surface corresponding to transverse wavevectors at $k_y = n\pi/l$ were made to satisfy the width quantization condition. Only odd modes are shown due to the excitation method used in the experiment. Stripline antennas only excite the odd width quantized modes as the even modes cancel under a uniform excitation field [67]. An applied field of $H = 870$ Oe and a saturation magnetization $M_s = 1765$ Oe were used, with an exchange parameter $\alpha_{ex} = 3.1 \times 10^{-12}$ cm^2. Totally unpinned boundary conditions were used, as pinning modes were not observed in the microwave measurements. 45 width quantized modes were considered as the 45th mode corresponds to the maximum efficient wavevector excited by the 50 μm width stripline antenna.

In Fig 2.3, frequencies at which 2D-TR BLS maps were measured are marked by dashed lines: BP, BG1, BG2, and BG3 correspond to $f = 4.25, 4.305, 4.38$, and 4.455 GHz, respectively, while A, B, C, and D correspond to $f = 4.10, 4.13, 4.15$, and 4.17 GHz respectively.

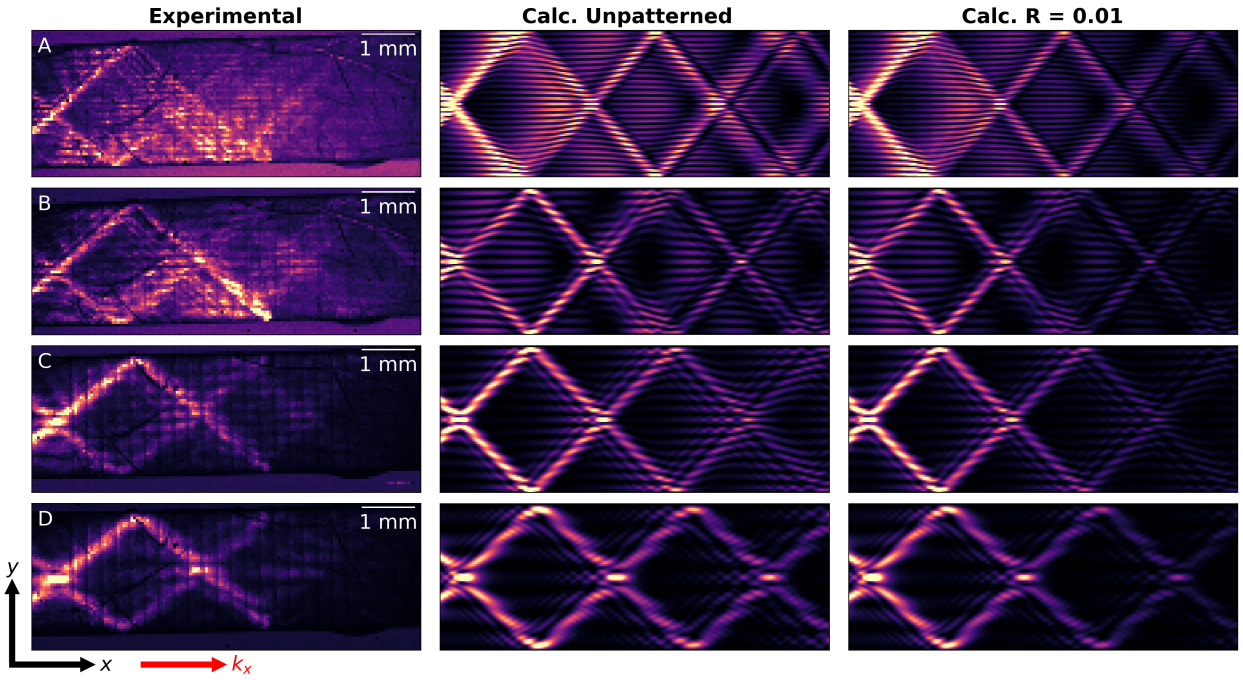

Figure 2.5: Two-dimensional maps of the spin wave propagation as a function of the position, where the scan region begins at $x_0 = 1$ mm away from the edge of the antenna. The columns show, from left to right, BLS measurements, calculations with no reflections ($R = 0$), and calculations with reflections ($R = 0.01$), and the rows correspond to the frequencies marked in Fig 2.2 below FMR (A, B, C, D).

The time-averaged 2D BLS maps are shown in Fig 2.4 and Fig 2.5. Fig 2.4 (left column) shows the maps for the BP, BG1, BG2, and BG3. Fig 2.5 (left column) shows the maps for A, B, C, and D. Complex interference patterns are formed for each measured frequency due to each width quantized mode excited having different longitudinal wavevectors. At the BP, the interference pattern takes the form of a repeating filled diamond. This pattern has been observed and reported in the literature previously [87, 88]. The slight asymmetry in the diamond is due to the YIG strip being misaligned with the field by approximately 1.5°. Dark vertical lines in each observed pattern are due to the laser light passing through the grooves causing a reduction in BLS signal intensity. The spin wave pulse travels uniformly through the interior of the diamond pattern, with periodic focusing of the spin wave density at the joint of one diamond to the next. As the excitation frequency is increased, the interference patterns observed become more complex. At BG1, the diamond has dark edges with spin wave density outside of the diamond and focused

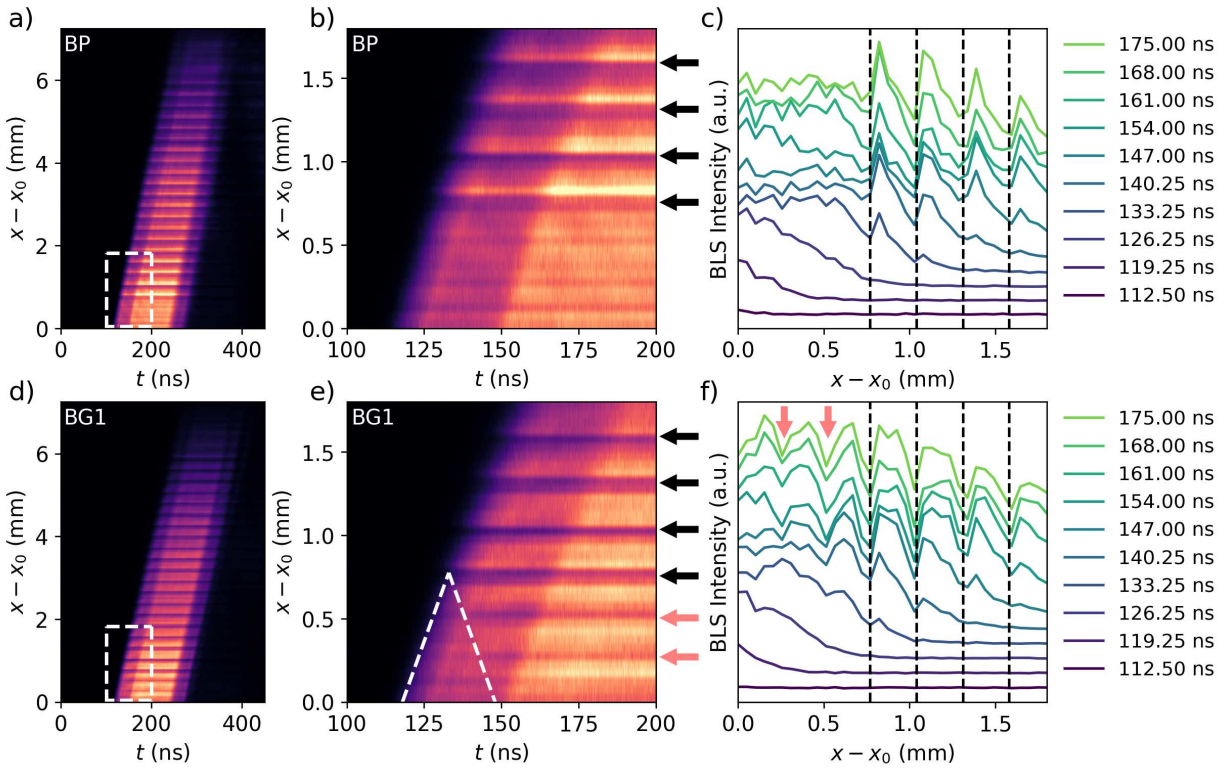

Figure 2.6: TR-BLS measurements along the length of the magnonic crystal where the intensity has been integrated over the width of the crystal. Panels (a-c) show measurements made at the first band pass (BP), while (d-f) show measurements at the first band gap (BG1). (a,d) show the pulse propagating down the full length of the crystal and (b,e) show a zoomed view (white square in (a, d)) ahead of the first etched groove. Black arrows indicate the groove positions, and the pink arrows in (e) and (f) show the positions of interference lines that develop at the first band gap BG1. No interference is observed for BP (b,c). The dark horizontal lines in (e) are absent within the region indicated by the dashed white lines and develop just to the right of the right-most line that marks the arrival times of reflection from the first groove position.

jet of spin wave density is formed along the center axis in the second repetition of the diamond. Enhanced spin wave density is also observed at the center of the flat between each groove. BG2 shows additional dark diagonal stripes, with an increased number of lobes forming for the spin wave jet. Finally, at BG3 the interference pattern no longer resembles the diamond pattern, with a more complex structure showing many lobes to the spin wave jet. The spatial resolution of the experiment is no longer sufficient to distinguish the finer features of the interference pattern.

The measurements below FMR, in Fig 2.5, show interference patterns that mainly take the form of the outline of a diamond. These interference patterns are primarily comprised of high

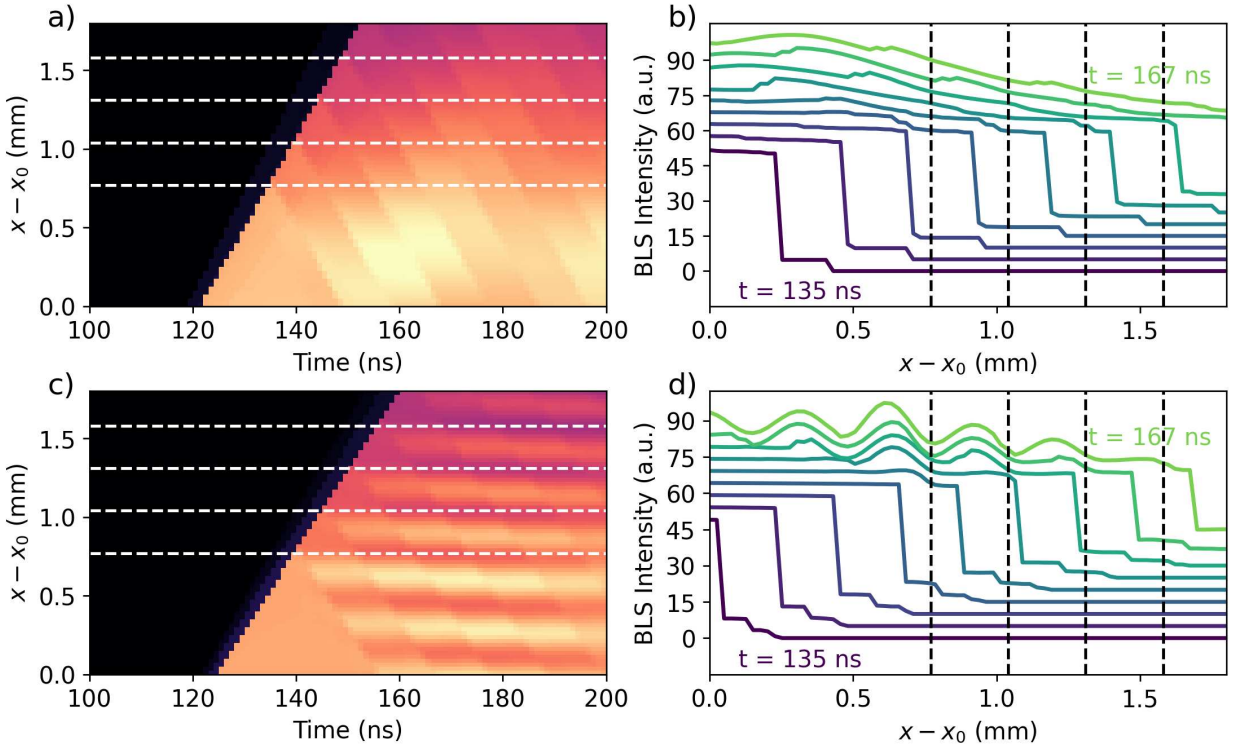

Figure 2.7: Calculated spin wave density as function of time for BP (a,b) and BG1 (c,d). Grooves are marked by white (black) dashed lines in (a,c) (b,d). a,c) show the calculated BLS spin wave density for the zoomed region in Fig 2.6b,e) for the BP and BG1, respectively. b,d) show single time traces spaced by 4 ns starting at $t = 135$ ns

n width quantized modes, as shown by the dispersion relation in Fig 2.3. Without the effect of width quantization, there would be no propagating modes at these frequencies. The width quantization can be directly observed in A, B, and C in the bright-dark pattern across the width of the crystal, with the number of anti-nodes (bright spots) across the width giving the lowest n mode excited at this frequency. The BLS intensity measured is an order of magnitude reduced from the measurements above FMR, and the spin wave pulse attenuates before the end of the scan region.

To disentangle the effects of width quantization and the magnonic crystal patterning, interference patterns were calculated for each of the measured frequencies. The center and right columns in Fig 2.4 and Fig 2.5 show calculated interference patterns both with (right column, $R = 0.01$) and without (center column, $R = 0$) reflections. The process used to include the effect of reflections is detailed in Appendix A.1. As can be seen when comparing two cases, the interference

patterns calculated are in good agreement with the experimental data, and are present regardless of reflections. The main interference pattern observed at each frequency is then due only to the confined geometry of the magnonic crystal. The reflections take the form of a perturbation on top that generate the ripples observed at the band gap frequencies. At the BP, the reflections only serve to cause additional attenuation down the length of the crystal and do not generate an additional interference pattern. At the band gaps, the reflections destructively interfere with the incoming spin waves, forming a standing interference pattern that corresponds to a wavevector of $k_{bg} = m\pi/d$, where m is the band gap number. BG1 thus has anti-nodes at the center of each repetition of the grooves, while BG2 has two anti-nodes, and BG3 has three. At BG3, the spatial resolution of the experiment is no longer able to resolve the standing interference pattern. The fine features within the lobes of the spin wave jet in BG3 are similarly smaller than the resolution of the experiment and cannot be resolved.

The calculated patterns for the sub-FMR measurements, shown in Fig 2.5, are in similarly good agreement with the patterns measured via BLS. These patterns demonstrate the importance of considering higher n width quantized modes, for in order to achieve good agreement with experiment, modes up to $n = 45$ must be considered. The lowest modes included for each patterns are $n = 13$ for D, $n = 15$ for C, $n = 19$ for B, and $n = 23$ for A. The addition of reflections does not change the overall spin wave pattern for these frequencies, only increasing attenuation down the length of the crystal.

Aside from the interference patterns observed, the time-resolved BLS intensity allows direct observation of the mechanism behind the band gap formation. Fig 2.6 shows the time-resolved BLS intensity for the BP (a-c) and BG1 (d-f), averaged over the width of the crystal. The propagation of the entire pulse along the entire length of the crystal can be seen in Fig 2.6a,d). The first groove is located at $x - x_0 = 0.775$ mm, and the dark horizontal features at position after this coincide with the subsequent grooves. A zoomed in view of the region before the first groove can be seen in Fig 2.6b,e). Single time traces are plotted in Fig 2.6c,f), showing both the buildup of interference for BG1, and the lack of coherent interference for the BP. The single time traces show

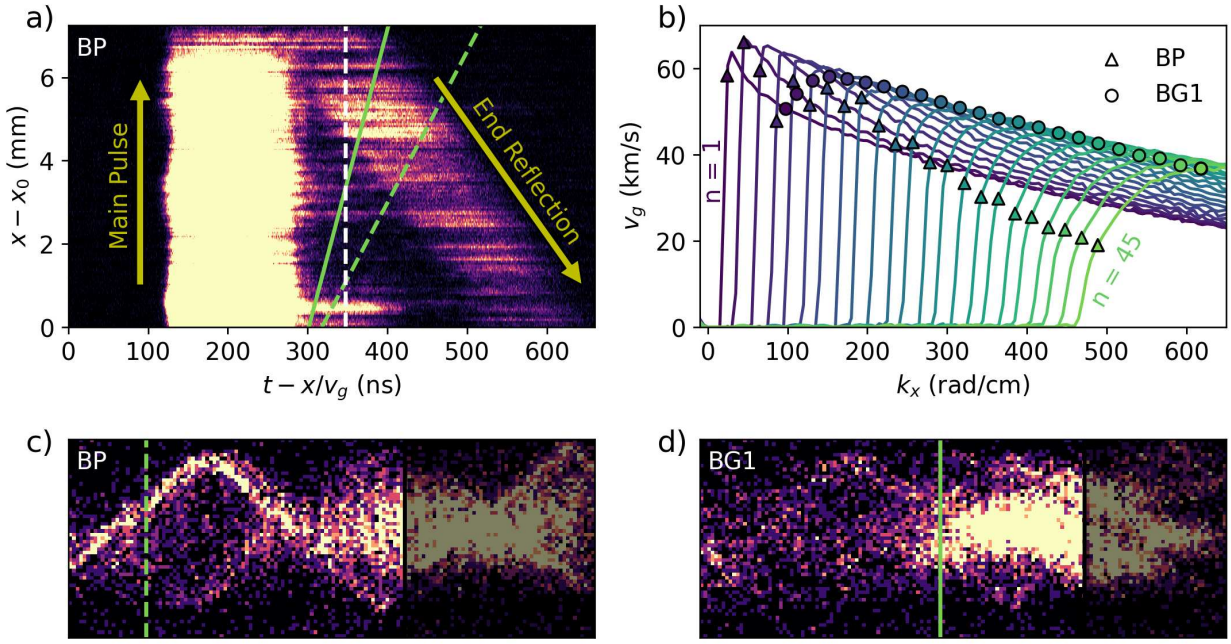

Figure 2.8: a) Width averaged time-resolved BLS intensity shifted by the average pulse group velocity for the BP. The trailing edge of mode $n = 45$ is indicated by the dashed green line for the BP, and the solid green line for BG1. The group velocities for each mode are shown in b), with triangles giving the group velocity for each mode at the BP, and circles for BG1. The spatial distribution of the BLS intensity at the time marked by the white dashed line in a) are shown for c) the BP and d) BG1. The predicted trailing edge of direct arrivals for the pulse is marked by the green dashed (solid) lines for the BP (BG1). The region where the reflection from the end of the crystal is present is shaded.

the formation of periodic structure at the same spacing as the grooves, marked by pink arrows in Fig 2.6e,f). These dips form only after the pulse has had time to both reflect from the first groove, and back propagate to interfere with the incident pulse. This is illustrated by the lack of interference build up in the region indicated by the white dashed lines in Fig 2.6e). No buildup of interference is observed for the BP, as there is no periodic structure in the region ahead of the first groove. Through this, we have directly observed the mechanism for the band gap formation in this magnonic crystal geometry.

In Fig 2.7, the calculated time-resolved spin wave density along the same region of the sample as shown. In Figs. 2.6b and 2.6e, single time traces show the same buildup in periodic structure ahead of the first groove at BG1, and a corresponding lack at the BP.

Close examination of the measured TR-BLS intensity shows additional intensity lingering after the main pulse passes through the crystal. Fig. 2.8a shows the TR-BLS intensity at the BP, after having been shifted by the average group velocity of the pulse. The group velocity the frequencies measured above FMR are $v_g = 53.5 \pm 0.2, 46.8 \pm 0.5, 38.3 \pm 0.5$, and 33.44 ± 0.08 km/s for the BP, BG1, BG2, and BG3 respectively. The average group velocity for each pulse was extracted through the use of cross correlation to track the pulse as it propagated through the crystal, as shown in Fig. A3. A linear fit to the lag time vs measurement position given by the cross correlation was used to find the group velocity, as shown in Fig. A3 a. The pulse was shifted so that the spatial distribution of the spin wave density after the main pulse passed could be examined. Fig. 2.8c and d show the spatial distribution for the BP and BG1 at time B. For the BP, the lagging spin wave intensity forms the outline of the diamond pattern, similar to the measurements for the sub-FMR frequencies shown in Fig. 2.5. This is due to the higher n width quantized modes having slower group velocities for the BP, shown in Fig. 2.8b, when compared to the low n modes. As these modes travel slower, they arrive later and form an interference pattern consisting only of them. Predicted direct arrival times are shown in Fig. A4 for the BP and BG1 in a and b respectively. Between the green dashed line and the shaded region in Fig. 2.8c, we expect only direct arrivals of modes $n \geq 21$ to be present. Any spin waves from reflections in this region will be much lower in amplitude than the direct arrivals. At BG1, the modes travel along a much narrower range of group velocities and the spatial distribution of spin wave density does not form a coherent interference pattern. The density at positions before the green line in Fig 2.8d is due to reflections from the grooves trapping spin waves.

2.3.4 Discussion

The time and spatially resolved BLS measurements directly show the mechanism behind the formation of band gaps in this magnonic crystal geometry through the buildup of interference between reflected and incident spin waves. BLS measurements made along the center axis of the crystal at various driving frequencies show the expected extinction in intensity at the band gap

frequencies shown in microwave measurements, additional features appear that are not adequately captured by the 1D model used to qualitatively describe the band gap formation. These features indicate that there is some 2D nature to the spin wave propagation through the crystal.

2D time and spatially resolved maps of the spin wave pulse show complex interference patterns that appear due to interference between width quantized modes. These modes appear due to the finite width of the magnonic crystal. The interference patterns can be calculated using the dispersion relation for an infinite film, from which cuts along transverse wavevectors satisfying the width quantization condition are made. As each mode has a slightly different dispersion relation, exciting spin waves at a given frequency generates a range of spin waves with different wavevectors. The difference between the longitudinal wavevector for each of these modes results in the formation of the interference patterns observed. These patterns are endemic to the confined geometry of the YIG strip and are not the result of the magnonic crystal patterning, as illustrated by the calculation of these patterns both with and without the presence of reflections. The 1D model of the magnonic crystal as a Bragg reflector captures the effect of the patterning, yet hides the complex interference effects and localization of the spin wave density.

The mechanism behind band gap formation was directly observed in the time-resolved BLS intensities measured at the band gap frequencies. By averaging the TR-BLS intensities over the width of the crystal, buildup of interference ahead of the first groove becomes apparent. After the pulse is partially reflected by the first groove, dips in the BLS intensity corresponding to the interference between the incident and reflected waves appears. Examining the calculated time resolved spin wave density shows the same behaviour at the band gap frequencies, and a corresponding lack of interference at the BP. In addition, lingering spin wave density due to reflection trapping spin waves is observed in the TR-BLS measurement of BG1.

These results suggest that the width-quantized modes are an important consideration for 1D magnonic crystals in the MSSW geometry. If a magnonic crystal lattice parameter is chosen with only the first width-quantized mode and there is no overlap between the band gap condition for the first mode and any of the other modes, the best possible rejection that could be obtained is

$10\log((\sum_{n=3,5...}^{45} 1/n^2)/(\sum_{n=1,3,5...}^{45} 1/n^2)) = -7.4$ dB since the transmission leakage from the other modes will limit the possible rejection efficiency. This mode leakage should be reduced substantially if the crystal is designed such that multiple modes simultaneously satisfy the band gap criteria. For example, if the first six odd-numbered modes are blocked then the rejection efficiency can be better than -15 dB. The effect of the width modes is, consequently, significant. For the magnonic crystal used in our work, the grove depth is large (3.5 μm), which helps to obtain a large rejection efficiencies. The expected band gaps overlap better for BG2 as compared to BG1, and the former has a better rejection efficiency, which is consistent with the idea that it is important to pay attention to the width modes. Previously, Chumak et al. found that BV magnonic crystals have a much greater rejection efficiency at the band gaps as compared to the MSSW geometry [64]. They showed that a transmission matrix model works well to explain the qualitative features of the microwave transmission measurements made in both configurations, however, reflection coefficients that differed by a factor of 12 were needed to match the experimental results, in spite of the fact that their estimates based on the first Born approximation predict that the reflectivity coefficients should be similar for the two configurations. They suggest that one of the possible reasons for this difference is coupling of the incident BVMSW to higher-order thickness modes, but the possible effects of width-quantized modes were not considered. Our results suggest that the thickness modes may contribute to the observed difference in their measurements. Adding in the thickness dimension may also be important, but the width dimension should not be neglected. In particular, choosing the width of the YIG strip l and dimensions of the the magnon crystal such that the transmission of many of the odd numbered width quantized modes ($n = 1, 3, 5, ...$) as possible are blocked at the same band gap frequencies will result in improved rejection efficiencies.

2.3.5 Conclusion

In conclusion, while it may be called a 1D magnonic crystal, the spin wave propagation through a 1D magnonic crystal in the MSSW configuration is inherently two dimensional. TR-BLS measurements show that quantization of the spin waves due to the finite width of the YIG strip lead

to prominent, diamond-shaped interference patterns. Localized increases in the spin wave density are observed, the distribution of which becomes increasingly complex with increasing frequency. The experimentally measured patterns agree well with calculations that consider interference of the width-quantized modes. The number of width quantized modes needed to reproduce the experimental observations is not small - approximately 22 modes are needed. The underlying mechanism for the formation of band gaps is also directly observed and replicated by the modeling. While the prevailing 1D model for magnonic crystals provides a useful framework to obtain a qualitative understanding of the expected band gap frequencies, consideration of the width quantization will be a key consideration in the design of 1D magnonic crystals with improved rejection efficiencies. Furthermore, the 2D nature of spin wave propagation in confined geometries detailed in this work provides additional avenues to exploit when designing future magnonic crystals, for example, the localization of spin wave density may be used as a potential tool in future device designs, either through beneficial placement of transducers, or through targeted placement of control elements.

Chapter 3

Magnonic notch filter based on spin wave caustic beams

3.1 Context

This chapter consists of the paper *Magnonic notch filter based on spin wave caustic beams*, which was accepted for publication in Applied Physics Letters in February 2024, as Editor's Pick.[2]

The supplemental information is shown in section B.1. In this work, the propagation of spin wave pulses through a 2D magnonic crystal were explored with time-resolved Brillouin light scattering. The generation of spin wave caustic beams at the crystal edges and at the defect lattice were observed and their relation to the formation of a rejection band in the transmission profile was explored.

3.2 Paper Summary

Here we study a magnonic crystal made of low-damping yttrium iron garnet that utilizes pseudo-caustic spin wave beams generated from subwavelength square well features arranged in a two dimensional array. The lattice symmetry and the angle between the caustic beam propagation direction and the applied magnetic field were tailored to optimize the interaction of spin waves with the engineered defects. A prominent, narrow 3 MHz feature with a large rejection efficiency is observed in the spin wave transmission spectrum that could be useful as a narrowband notch filter, and time- and space-resolved Brillouin light scattering (BLS) measurements suggest that that

[2]Author list: Mitchell S. Swyt, Lia Compton, Arturo Reyes-Almanza, César L. Ordóñez-Romero, Giuseppe Pirruccio, H. J. Jason Liu, and Kristen S. Buchanan. The magnonic crystal was patterned by Arturo Reyes-Almanza, César L. Ordóñez-Romero, and Giuseppe Pirruccio (Universidad Nacional Autónoma de México). All Brillouin light scattering measurements were made by Mitchell S. Swyt and Lia Compton. Microwave measurements on the magnonic crystal were made by Mitchell S. Swyt and Lia Compton. Microwave measurements on unpatterned YIG were made by César L. Ordóñez-Romero and Giuseppe Pirruccio. Calculations of the caustic beam properties were made by Mitchell S. Swyt and Kristen S. Buchanan. The paper was written and edited by Mitchell S. Swyt, Kristen S. Buchanan, H. J. Jason Liu, César L. Ordóñez-Romero, and Giuseppe Pirruccio.

both caustic interference and edge effects may contribute to this notch feature. Furthermore, the BLS measurements show that caustics are generated efficiently at the laser ablated wells, and by tuning the frequency by 30 MHz, the caustic beam angles and hence the details of how the spin wave caustics hit the ablated wells change sufficiently to add and remove caustic beams, which can be used to create additional device functionality. The generation and conversion of caustic beams show promise for applications that require directional energy transport, and for magnonic devices.

3.3 Research Article

Magnonic devices use spin waves, also known as magnons, to transmit information and perform logic operations. These devices offer the possibility of chargeless, low power operation and compatibility with CMOS, [5–10] and hybrid solutions for quantum information and magnonic logic. [72] Magnonic crystals, artificial crystals with periodically modulated magnetic properties, are one of the building blocks of magnonic devices including magnonic transistors. [89] Periodic modulation can be achieved by altering the material properties, [76, 78, 90, 91] or the geometry by using patterned grooves. [64, 65] The simplest magnonic crystals are periodic in one dimension and show band gaps due to the interference of multiply reflected waves when the spin wave wavevectors are integer multiples of π/a, where a is the lattice parameter. [63–66] 2D magnonic crystals have also been realized experimentally and form band structures that agree well with micromagnetic predictions, [79, 82, 92–95] and diffractive effects from carefully arranged patterns can be used to focus spin waves through Fresnel-type lenses and to generate repeated patterns via the Talbot effect. [96]

Caustic beams, narrow (sub-wavelength) beams that can be generated in anisotropic systems, exhibit a high degree of spatial coherence and are promising for applications that require directional energy transport. Caustics form in a variety of systems involving photons, phonons, and magnons when anisotropies that lead to preferred group velocity directions are present. Spin wave caustics can be realized in in-plane magnetized films, where spin wave beams will radiate from a point source excitation along preferred directions. [97–99] Formally, caustics form at points in

wave vector (k)-space where the curvature of an isofrequency curve, obtained from dispersion relations, is zero, which corresponds to a region in k-space where the wave amplitudes are enhanced, and pseudo-caustic beams can be observed when an isofrequency curve has regions with nearly constant group velocity directions even if the curvature of the isofrequency curve does not drop to zero. [100, 101] Spin wave caustics have been observed from a variety of point sources including defects, [83] patterned anti-dots and sub-wavelength features, [69, 102–104] and femtosecond laser pulse excitations, [105]. Caustics have also been generated from the junction of a thin waveguide and an extended film, [99] edge mode scattering, [100] and specially-designed antennas. [98] Caustics are highly directional, and their angle of propagation can be controlled by the angle and magnitude of the applied external field and the excitation frequency, which can be used for frequency selectors and demultiplexers. [97, 106, 107] Furthermore, the effective wavelength of a caustic $\lambda_{\mathtt{eff}}$ is also tunable, which may be useful for the design of interference-based magnonics devices. Pseudo-caustic beams have been observed in a variety of magnetic systems, however the potential of incorporating caustics into a magnonic crystal has remained largely unexplored thus far.

Here we investigate a 2D magnonic crystal with features that are small compared to the spin wave wavelength. Microwave measurements of the transmission profile of the crystal show rich features rather than the simple periodic band gaps that are observed for 1D magnonic crystals, and time- and spatially-resolved Brillouin light scattering (BLS) measurements show that the small relative feature sizes allow for the generation of spin wave caustics, creating an operational mechanism unlike other reports on 2D magnonic crystals. A pronounced narrow-band region with a suppression of the transmission of > 20 dB is found when the magnetic field is applied at an angle where the caustics are well aligned with the lattice of square wells, and BLS measurements suggest that interference effects as well as interactions of the caustics with the sample edges may both contribute to the observed suppression.

A 2D magnonic crystal was fabricated using a yttrium iron garnet (YIG) film, $h = 6.4$-μm thick, grown by liquid phase epitaxy on a gadolinium gallium garnet (GGG) substrate. YIG was

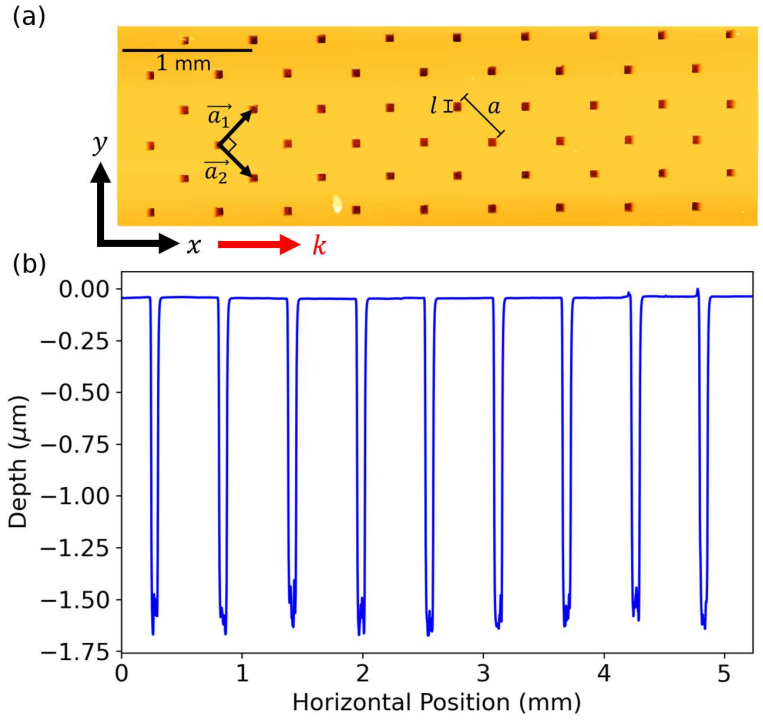

Figure 3.1: Profilometry measurements of the 2D magnonic crystal showing (a) the patterned region and (b) a cross-sectional profile along the length of the crystal through the second row from the top. The lattice parameters $\boldsymbol{a}_1$ and $\boldsymbol{a}_2$, spacing a, and width l of the square wells are shown on (a).

chosen for its low magnetic damping and long spin wave propagation distances. [68] Gentle micro laser ablation was used to create a two-dimensional lattice of square wells with depth $d = 1.6$ μm, side length $l = 70$ μm, and nearest neighbor center-to-center spacing of $a = 400$ μm on a YIG strip that was $w = 2$ mm wide and $\sim$15 mm long. Femtosecond (230 fs) pulses centered around 515 nm are generated by a high power ultrafast laser (Pharos, Light Conversion) with a repetition rate of 1 MHz. Pulses are focused to a 2 μm spot, which is at least two orders of magnitude smaller than the spin wave wavelength and one order of magnitude smaller than the spatial resolution obtainable with a traditional mask-assisted chemical etching. Figure 3.1 shows profilometry measurements of the patterned region, which consists of a square lattice of wells rotated by 45° with respect to the long axis of the crystal with an angle of 90° between the lattice vectors $\boldsymbol{a_1}$ and $\boldsymbol{a_2}$ with $|\boldsymbol{a_1}| = |\boldsymbol{a_2}| = a$. The edges of the square wells are nearly vertical and the film surface near the

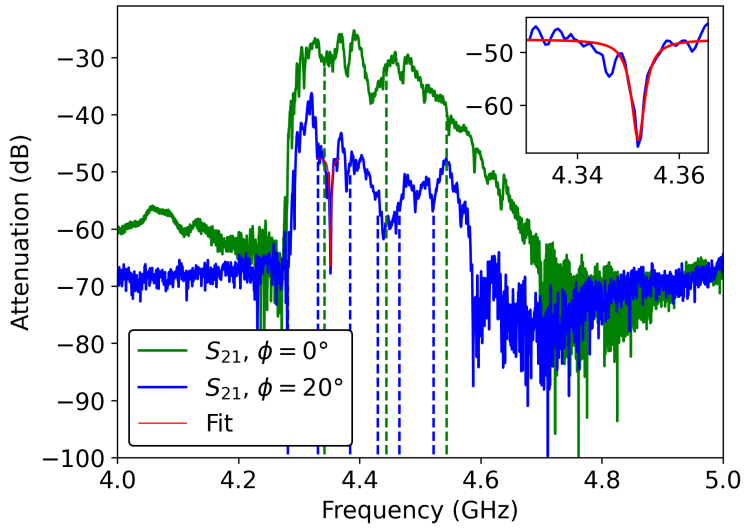

Figure 3.2: Spin wave transmission profile in the MSSW configuration ($\phi = 0°$, green) and with H applied at $\phi = 20°$ from the y-direction (blue). The inset shows a zoomed-in view of a sharp dip in transmission observed for $\phi = 20°$ with a fit (red line). Dashed lines indicate frequencies at which the effective caustic wavelength $\lambda_{\mathtt{eff}}$ (Fig. 3.4(d)) satisfies the condition for destructive interference for $\phi = 0°$ (green) and $\phi = 20°$ (blue).

wells is unaffected by the patterning process. The well spacing a is on the order of the spin wave wavelength λ so that interference may occur, and l is small relative to λ.

Microwave antennas were placed approximately 3 mm before and 2 mm after the patterned region to excite and detect spin waves, respectively. Transmission measurements were made using a vector network analyzer with an in-plane external magnetic field of $H = 865$ Oe in the magnetostatic surface spin wave (MSSW) geometry ($\phi = 0°$), and with $\phi = 20°$, where ϕ is the angle of H with respect to the y-direction. An input power of $P_{in} = -17$ dBm was used, which is within the linear response regime. Time- and spatially-resolved BLS measurements were made at selected frequencies to investigate the details of the spin wave propagation patterns. Spin wave pulses, 200 ns in duration, were generated using a microwave source and a microwave switch with an input power of 4 dBm and a repetition time of 1.2 μs, selected to remain in the linear response regime and to minimize sample heating, respectively. BLS measurements were made with a 50 μm spacing between points using a wavelength of 532 nm in a forward scattering configuration that is sensitive to wavevectors up to at least 3.6×10^4 rad/cm. [55] The inelastically scattered light was

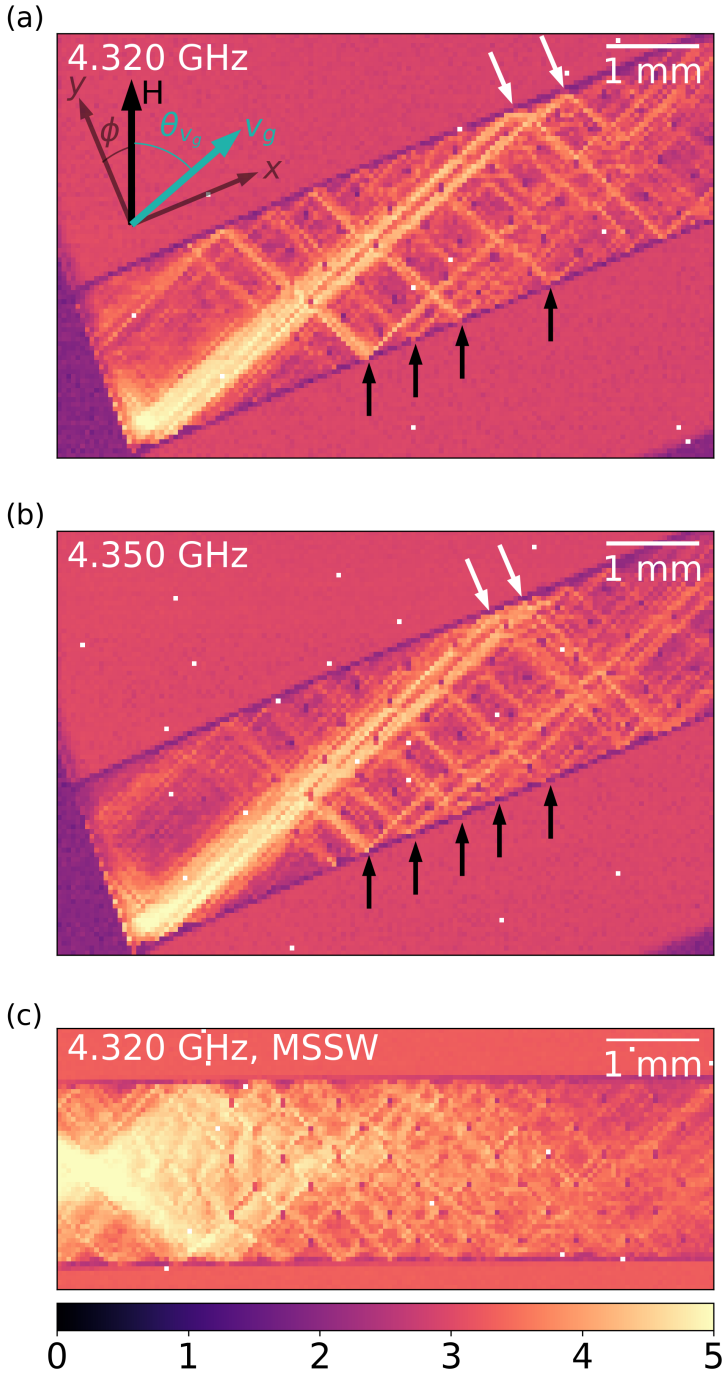

Figure 3.3: Time-integrated BLS intensity maps with a logarithmic intensity scale for (a) 4.320 GHz, and (b) 4.350 GHz with $\phi = 20°$, and for (c) 4.320 GHz with $\phi = 0°$. The spin waves are generated by the antenna on the left. In (a) and (b), white arrows indicate where the main pulses hit the edge of the crystal, and black arrows highlight selected caustics generated by the square wells. The white dots in the images are areas where the transmitted light intensity was low.

collected with a TFP2-HC tandem Fabry-Perot interferometer with a mirror spacing of 10 mm and separated into 250 ps bins using a fast time-of-flight DAQ card.

Figure 3.2 shows transmission profiles of the 2D magnonic crystal in the MSSW geometry ($\phi = 0°$) and for $\phi = 20°$. The $\phi = 0°$ transmission profile is similar to the profile for MSSWs in an unpatterned YIG strip (Fig. S1). The transmission increases sharply at approximately the ferromagnetic resonance (FMR) frequency, shows a maximum at just above FMR, and then decreases gradually with increasing frequency due to a decrease in the excitation efficiency of the antenna with increasing k. The modulations in the transmission profile between 4.3 and 4.5 GHz are attributed primarily to the patterning of the film, while the narrow, periodic dips at about 4.45 GHz and above are weak pinning modes. The most prominent feature in the MSSW transmission profile is a broad dip centered at 4.42 GHz, but this feature shows a less dramatic maximum attenuation as compared to band gap profiles observed for 1D YIG magnonic crystals, and may be due to the film rather than the patterning (e.g., see [64]).

For $\phi = 20°$ (Fig. 3.2, blue), the transmission is reduced as compared to $\phi = 0°$, and the transmission profile shows a number of peaks and dips, most notably a deep, narrow dip appears at $f_r = 4.352$ GHz with a full width half max of 3 MHz (based on a Lorentzian fit) and an attenuation of > 20 dB relative to the transmission profile at adjacent frequencies. Transmission measurements on an unpatterned YIG strip from the same wafer (Supplemental Materials) show that the transmission profiles can vary depending on the antenna placement for $\phi = 20°$, which suggests that transmission measurements alone are not sufficient to understand the spin wave propagation at this angle.

BLS scans were collected to gain further insight into the spin wave propagation in the 2D magnonic crystal. Figures 3.3(a) and (b) show time-integrated maps of the spin wave propagation patterns obtained at 4.320 GHz, the peak transmission frequency, and at 4.350 GHz, near the notch feature at f_r. The ratios of input to transmitted counts are similar for Figs. 3.3(a) and (b), hence the BLS measurements shown in Fig. 3.3(b) do not correspond exactly to the notch feature in Fig. 3.2. Large (10 cm diameter) pole pieces were used to obtain a spatially uniform field, but a

small gradient of ~ 3 Oe is present across the sample that shifts the spin wave frequencies by up to 5 MHz, hence it is difficult to obtain scanned BLS measurements for the exact conditions that correspond to the notch feature. The BLS measurements nevertheless provide direct insight into how the spin wave propagation pattern changes with frequency.

In both Fig. 3.3(a) and (b) a strong initial bright beam is observed near the bottom of the antenna. This initial beam interacts with the sample edge to create two main caustic beams with widths of approximately 150-200 μm. These beams are well aligned with a series of wells, and when the beams hit the wells they are scattered into additional caustics that appear as bright tracks radiating from the wells. When the main beams (white arrows) and secondary caustics (black arrows) interact with the edge of the YIG film, bright, coherent beams are also seen afterwards. These are new caustics, not reflections, as the angles of the beam before and after the edge interactions are symmetric with respect to the direction of H rather than the the edge normal. The propagation angles θ_{vg} were obtained from the BLS images directly and using a Radon transform method that computes the line integrals of different paths through an image. This yields $\theta_{vg} = 48.38°$ for 4.320 GHz, and $\theta_{vg} = 47.62°$ for 4.350 GHz, with a difference of $\Delta\theta = 0.77°$.

The change in θ_{vg} is enough to change the alignment of the main beams with the wells and the caustic patterns. At 4.320 GHz, caustics directed towards the top left are generated when the top beam interacts with the lower set of intersected wells, and these back-directed beams are almost completely absent at 4.350 GHz. At 4.320 GHz the bottom beam also creates forward-directed caustics at each of these wells, marked by black arrows in Fig. 3.3(a). At 4.350 GHz, caustic beams that are directed towards the bottom right are generated from the wells in the paths of both the top and bottom beams (marked by black arrows in Fig. 3.3(b)), and the beams after the main pulse hits the edge of the crystal are less intense and more diffuse in Fig. 3.3(b) (white arrows) as compared to what is seen in Fig. 3.3(a).

Caustic spin wave beams are also observed in the MSSW geometry (Fig. 3.3(c)), however, the initial beam spans the width of the YIG film so while caustics are generated at each of the wells,

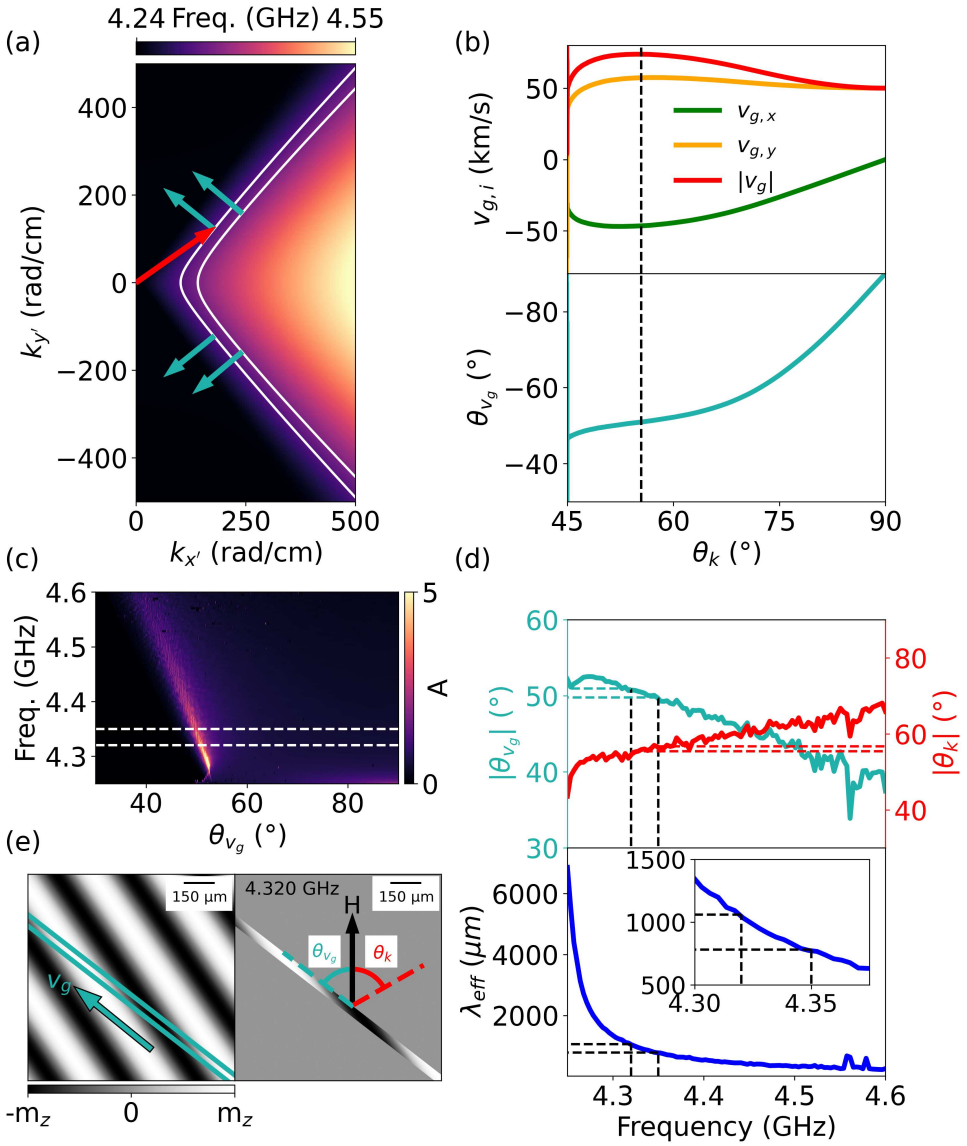

Figure 3.4: (a) Calculated dispersion relation for a YIG film with isofrequency curves (white) for $f = 4.320$ GHz and 4.350 GHz. Only the highest frequency mode is shown. Pseudo-caustic points are marked with teal arrows that indicate the direction of the group velocity. The red arrow shows the wave vector for one of the 4.320 GHz caustic points. (b) Group velocity magnitudes (top) and angle θ_{vg} (bottom) as a function of θ_k, both relative to $\boldsymbol{H}$ (y'), for 4.320 GHz. The vertical dashed line indicates the pseudo-caustic point. (c) A versus f and θ_{vg}, showing strong enhancement in specific directions. (d) Angles $|\theta_{vg}|$ (teal) and $|\theta_k|$ (red) for the maximum A in (c), and $\lambda_{\mathtt{eff}}$ (bottom) as a function of f. The inset shows a zoomed view of $\lambda_{\mathtt{eff}}$. The measurement frequencies, 4.320 and 4.350 GHz, are marked by vertical dashed lines. (e) Calculated caustic for $f = 4.320$ GHz showing a plane wave with the caustic beam position overlaid (teal lines) and the corresponding masked caustic beam (right).

only a portion of the initial beam is converted to caustics. This explains why the features in the transmission spectrum for $\phi = 0°$ are weak compared to those observed for a 1D magnonic crystal.

To confirm that the observed beams are caustics, the dispersion relation for the YIG film (Fig. 3.4(a)) was calculated following the matrix method described by Kalinikos et al. [45] using a saturation magnetization $M_s = 1758$ Oe, an exchange parameter of $\alpha_{ex} = 3.1 \times 10^{-12}$ cm^2, and unpinned boundary conditions since the transmission profile in the MSSW geometry (Fig. 3.2 (green)) shows only weak pinning modes.[3] The group velocity, $\boldsymbol{v}_g = \nabla_{\boldsymbol{k}} 2\pi f$ where f is frequency, is perpendicular to an isofrequency curve in k-space, and the isofrequency curves in Fig. 3.4(a) (white lines) show that a wide range of wave vectors will have similar θ_{v_g}.

Caustic and pseudo-caustic points correspond to points in k-space where the curvature of the isofrequency curve is zero or minimal, respectively. For 4.320 GHz a caustic point occurs with $\theta_{v_g} = 50.38°$, and for 4.350 GHz a pseudo-caustic point is found with $\theta_{v_g} = 49.57°$, with a difference of $\Delta\theta = 0.81°$, consistent with the BLS measurements. Caustic points can also be identified using the amplitude enhancement factor [108]

$$A = \left(\frac{1}{|v_g|} \frac{dv_g}{d\theta_k} \right)^{-1}, \tag{3.1}$$

where $\theta_k = \arctan(k_{x'}/k_{y'})$ is the angle of the wavevector. The values of $\boldsymbol{v_g}$, θ_{vg}, and θ_k are determined along an isofrequency curve (Fig. 3.4(b)) and used to calculate A (Fig. 3.4(c)). The caustic or pseudo-caustic beam direction corresponds to the maximum of A for a given f. Figure 3.4(d) shows that $|\theta_{vg}|$ decreases almost linearly with increasing f, while the effective wavelength of the caustic $\lambda_{\mathtt{eff}} = \lambda/cos(\theta_{vg} - \theta_k)$, the wavelength along the radiation direction, decreases rapidly with increasing f, with $\lambda_{\mathtt{eff}} = 1032$ μm for 4.320 GHz (Fig. 3.4(e)), and $\lambda_{\mathtt{eff}} = 764$ μm for 4.350 GHz. Note that the peak in A in Fig. 3.4(c) covers a broader range of θ_{vg} at 4.350 GHz

[3]The dispersion relation surface was calculated numerically using the method described in Kalinikos et al. [45] Sec. 5. The isofrequency curves were found by fitting a spline to the surface at the selected frequencies. From the isofrequency curve, the group velocity was found using a numerical gradient and smoothed with a Savitzky-Golay filter to remove numerical noise.

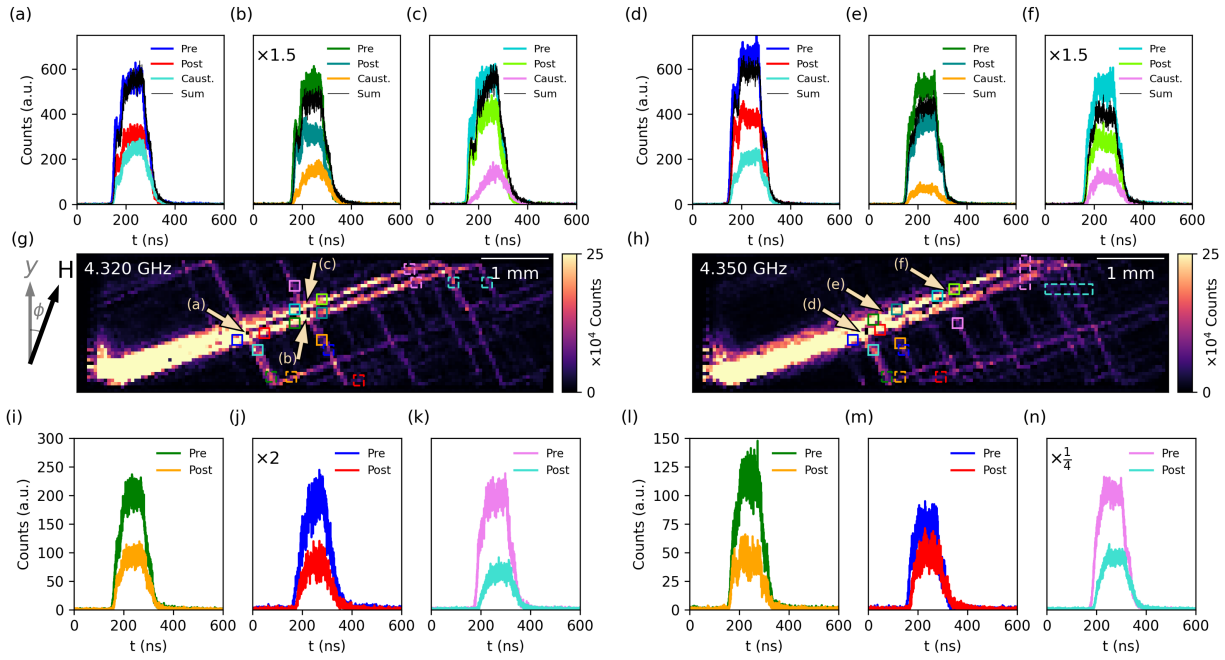

Figure 3.5: BLS intensity as a function of time integrated over the boxed regions in (g) and (h), where the trace and box colors correspond. (a-f) BLS signals before and after the labeled wells in (g) and (h). “Pre" and “Post" signals correspond to positions along the main beam before and after interaction with a well, “Caust." is the caustic offshoot, and “Sum" is the sum of “Post" and “Caust." (black line). (i-n) BLS signals obtained before (“Pre") and after (“Post") selected edge locations, where the integration regions are indicated by the dashed boxes. The signals in (a-c,g,i-k) and (d-f,h,l-n) were obtained at 4.320 and 4.350 GHz, respectively, for $\phi = 20°$.

as compared to 4.320 GHz, which is likely the reason the caustics show greater broadening at 4.350 GHz as compared to 4.320 GHz in Fig. 3.3.

Figure 3.5 shows the time-dependent BLS measurements at selected positions. Strong caustics, where approximately one third to one half of the original signal intensity goes into the caustic (the ratio of the “Caust." curve to the “Pre." curve in Figs. 3.5(a-f)), are observed when the incoming beam hits a well directly (Figs. 3.5(a,b,d)), and glancing interactions generate weaker caustics (Figs. 3.5(c,e,f)) where the caustic intensity is less than one third of the initial signal. In all cases, the caustic generation process is efficient. The sum of the post-caustic and caustic signals (black lines in Fig. 3.5 (a-f)) shows only a 0-20% change as compared to the pre-caustic signal. In contrast, as shown in Fig. 3.5(i-n), the intensity of a caustic beam drops by 33 to 66% (approximate

attenuation of ~ -2 dB) when it is regenerated at the sample edge, and the losses vary considerably with location, which is likely due to variations of the edge quality.

There are several possible explanations for the observed notch feature: (i) losses due to caustic generation at the wells, (ii) losses due to edge interactions, and (iii) destructive interference of forward- and backward-propagating caustics.

An upper limit for (i) is obtained by comparing the conversion losses for a caustic that intersects seven wells along its path, estimated from Fig. 3.3(b), as compared to a caustic that misses all of the wells, which yields $\sim$6.8 dB (assumes a 20% loss per well). Mechanism (i) is insufficient to explain the > 20 dB rejection, especially since the difference in beam-well interactions for Figs. 3.3(a) and (b) is $\sim$2.

The losses due to interactions of the caustics with the sample edge are larger and more varied as compared to losses at the wells. The main beams carry the majority of the energy for $\phi = 20°$. The position where these beams hit the edge for the second time (Fig. 3.5(k,n)) changes by $\sim$500 μm from $f = 4.320$ to 4.350 GHz, a large enough distance that it is likely that edge effects play a role in the observed variations in the transmission spectrum for $\phi = 20°$ (Fig. 3.2). For surface and backward volume spin waves the precession amplitudes are lower near edges, [109–111] which reduces edge losses. As shown in the Supplemental Materials, the spin wave transmission in an unpatterned YIG film is sensitive to the antenna placement for $\phi \geq 4°$, which is likely due to edge effects. The maximum edge loss observed in Fig. 3.5 is $\sim$10 dB, which is still less than the notch depth, though larger edge losses may be possible.

Destructive interference between the forward and backward-going caustics (iii), may also explain the notch feature. While the 3 MHz notch width is small compared to the 10-50 MHz band gaps typical for a 1D magnonic crystal, [66] $\lambda_{\mathtt{eff}}$ changes rapidly with frequency (Fig. 3.4(d)), which would lead to a narrower band gap. Destructive caustic interference and reduced transmission are expected when $\lambda_{\mathtt{eff}} = n\pi/a_{\mathtt{eff}}$, shown as dashed lines in Fig. 3.2, calculated using $a_{\mathtt{eff}} = a$ for $\phi = 0°$, and the well spacing along the main caustic path $a_{\mathtt{eff}} = |2\boldsymbol{a_1} + \boldsymbol{a_2}| = 894\ \mu$m for $\phi = 20°$. The calculated frequencies are close to several features in the transmission profiles,

and the $n = 2$ line (4.331 GHz) is close to f_r, within the uncertainty of the calculations. While further investigations are needed to definitively determine the relative importance of each of these mechanisms, these results highlight the unique potential of caustic beams for magnonics applications.

In summary, BLS measurements show that caustic formation is a primary consideration in the behavior of this 2D magnonic crystal with subwavelength features. By tuning the frequency by 30 MHz, caustic beams can be turned on or off through changes in how the beams interact with the wells. Since the caustic beam angle can also be tuned locally through small changes in H or ϕ_H, this effect may be useful for logic operations. Furthermore, an unusually deep (> 20 dB) and narrow (3 MHz) feature is observed when H is applied in-plane at an angle of $\phi = 20°$, which may be due to edge effects, destructive interference of caustics, or a combination of these. This could serve as a notch filter. Our results demonstrate the unique potential of caustics to add functionality to magnonic devices by tuning the beam direction, exploiting the rapid change of effective wavelength, and by tailoring the characteristics of edges to tune the caustic absorption and regeneration process.

Chapter 4

Low temperature Brillouin Light Scattering measurement of the interfacial Dzyaloshinskii-Moriya interaction

4.1 Context

This chapter consists of the paper *Low temperature Brillouin Light Scattering measurement of the interfacial Dzyaloshinskii-Moriya interaction*, a manuscript under preparation.[4]

This paper reports the measurement of the temperature dependence of the interfacial Dzyaloshinskii-Moriya interaction in Pt/Co from 15 K to room temperature by low temperature Brillouin light scattering. It explores a temperature range unreported in the literature and provides a temperature dependence consistent with measurements made above room temperature.

4.2 Paper Summary

There has been enormous recent interest in the Dzyaloshinskii-Moriya interaction (DMI), especially the interfacial DMI (iDMI) that arises at the interface of heavy metal (HM) and Ferromagnetic (FM) bilayer thin films due to a combination of large spin orbit coupling and broken inversion symmetry. The iDMI can promote the formation of chiral magnetic spin textures such as magnetic skyrmions and leads to anisotropic spin wave propagation effects, which are potentially important for applications. Here we report direct measurement of the temperature dependence of the iDMI in Pt/Co/SiO_2 thin films, an aspect that has received little attention thus far. Brillouin Light Scattering measurements made from room temperature (RT,$\sim$ 300 K) down to 15 K show

[4]Author list: Mitchell S. Swyt, Lia Compton, Md. A. Jafar Pikul, Yang Wang, John Q. Xiao, and Kristen S. Buchanan. The films used were deposited by Yang Wang and John Q. Xiao (University of Delaware). The Brillouin light scattering measurements were made by Mitchell S. Swyt and Lia Compton. Magnetometry was performed by Md. A. Jafar Pikul. The paper was written and edited by Mitchell S. Swyt and Kristen S. Buchanan.

that the iDMI increases with decreasing temperature following a scaling law of $D \propto M_s^{\alpha}$ where $\alpha = 4.5 \pm 0.8$, a greater scaling than predicted by theory ($\alpha = 1.5$ or 2), but in agreement with previous measurements of the iDMI at high temperatures.

4.3 Research Article

4.3.1 Introduction

The interfacial Dzyaloshinskii-Moriya interaction (iDMI), an antisymmetric exchange interaction that occurs at the interface of magnetic and non-magnetic layers with large spin-orbit coupling, has attracted considerable attention recently. The presence of iDMI leads to an energetically favored chirality or handedness, and this leads to interesting static and dynamic effects. The iDMI stabilizes chiral spin textures, such as Néel domain walls with preferred chiralities and skyrmions, small swirling spin textures with a central [12, 29]. Skyrmions and chiral domain walls in a magnetic film or wire can be propelled by spin currents [13, 14] due to the spin transfer torque and spin orbit torques. The iDMI also leads to unusual dynamic effects including anisotropic spin wave propagation, caustic beams, unusual nonlinear effects [112]. Exploring the iDMI has consequently become of particular interest in the pursuit of appropriate materials from which to build spintronic devices.

Here we can add some references to theory papers on tunability of skyrmion size, to experimental review papers on the DMI magnitude.

The interplay between magnetic anisotropy, exchange, and the iDMI leads to a complex magnetic phase diagram for the ground state, so the ability to tune the iDMI is essential in selecting the desired spin texture. Sizeable iDMI has been observed in FM/HM bilayers [20–22], and the iDMI has also been observed in FM/FMO_x [113, 114], FM/MgO_x [115, 116], and more [117–121]. In addition to looking for new materials, the ability to control the iDMI with an applied voltage [116] or with strain [122] has been demonstrated. Spintronic devices, such as racetrack memory [11], that rely on spin currents to manipulate magnetic textures necessarily involve the heating of the device, as Joule heating is unavoidable with an applied current density. Thus, understand-

ing the temperature dependence of the iDMI is necessary to understanding the behavior of these devices in operation. Previous studies have explored temperature ranges above room temperature, through measurements of domain expansion [123], and through Brillouin light scattering (BLS) studies [124]. Both of these studies have reported similarly large deviations from the theoretical dependence of $D \propto M_s^2$ [125] or $D \propto M_s^{3/2}$ [126].

Here we report the measurement of the temperature dependence of the iDMI parameter along the range from 15 K to 300 K for Pt/Co. Cryo-BLS was used to measure the frequency shift induced by the iDMI for surface spin waves propagating in opposite directions, with magnetometry used to measure the temperature profile of the magnetization. We find that for the system studied, the iDMI varies strongly with temperature, with a greater dependence on the magnetization than theory predicts. The measured dependence, however, is consistent within uncertainty of the dependencies shown in [123, 124] for similar systems above room temperature.

4.3.2 Experimental Methods

The iDMI was measured using Brillouin Light Scattering (BLS) in the Damon-Eshbach (DE) configuration. Each measurement was made at the same applied field, while the temperature of the sample was varied. The applied field was parallel to the surface of the film, and perpendicular to the plane of incidence of the laser. The iDMI has measurable effects on surface spin waves in thin films [30, 127] that provide a means to probe the magnitude of the iDMI quantitatively. In extended films with a HM/FM interface, the iDMI leads to an asymmetry in the dispersion relation for surface waves. According to Moon et al. [30] (eq. 16) the frequency of a surface wave is linearly proportional to the wavevector k in the limit $|k|d << 1$, where d is the thickness of the magnetic thin film. These frequency shifts are resolvable by BLS, which has proven to be a valuable technique to study spin dynamics [128], and has become one of the most reliable ways to obtain quantitative measurements of the iDMI. [19, 54]

BLS measurements were performed on Pt/Co (Si/Ta/Pt/Co/SiO2 [Sub./5/3/1/5 nm]) in a backscattering configuration to probe the iDMI. The backscattered light was collected and analyzed using

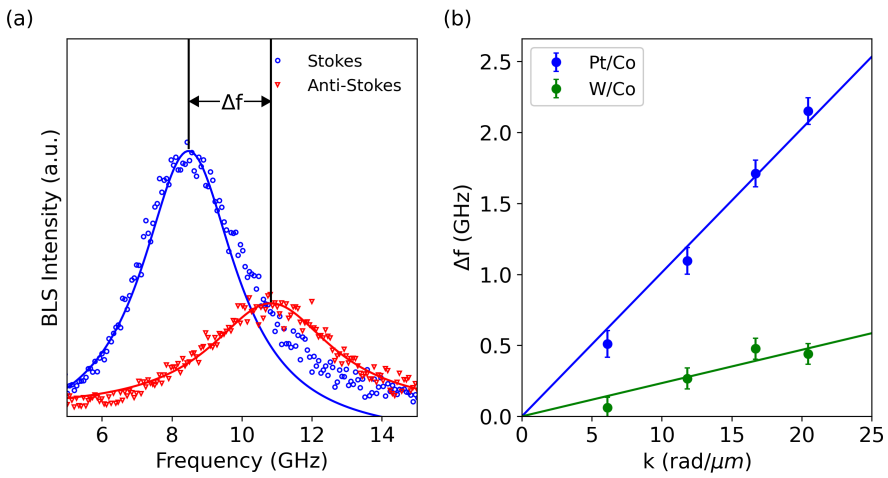

Figure 4.1: (a) BLS spectra for spin waves in Pt/Co measured at $T = 238$ K. Lorentzian fits are overlaid. (b) Frequency shifts measured at room temperature for Pt/Co and W/Co as a function of wavevector. Linear fits used to extract D are overlaid.

a Sandercock TFP2-HC interferometer with a mirror spacing of 8 mm, giving a fundamental frequency resolution of the interferometer $2\Delta d_{1/2} = d_{fsr}/\mathcal{F} = 156$ MHz. A Montana Instruments Cryostation cryostat with the Magneto-Optical Module was used to cool the samples while allowing for optical access. A calibrated temperature probe mounted inside the sample post, directly under the sample, was used to measure the temperature of the sample. The sample was initially cooled to 15 K, then warmed to each measurement temperature sequentially, up to RT. The samples were mounted to the post with N-grease to ensure good thermal contact.

A saturating magnetic field, H, was applied parallel to the surface of the sample and perpendicular to the plane of incidence of the light. The angle of incidence θ, measured relative to normal of the sample was fixed at 45° for measurements below room temperature and varied from 15° to 70° at room temperature. A single measurement at 45° has been shown to be sufficient to estimate the iDMI, with the room temperature measurements confirming this assumption. Through conservation of momentum, the in-plane wavevector is given by

$$k = \frac{4\pi}{\lambda} \sin\theta, \tag{4.1}$$

where λ is the wavelength of incident light, which is 532 nm for these measurements. For nanometer-thick films, two peaks are generally detected that are due to surface waves with the same $|k|$, one on the Stokes side of the spectrum and the other on the anti-Stokes side. The two peaks are associated with surface waves that travel in opposing directions, one on the top and the other on the bottom surface of the magnetic layer. The difference, Δf, between the anti-Stokes and Stokes peak frequencies f_0 was used to calculate the iDMI parameter. This was done for the peaks of a single spectrum at a fixed field.

Laser heating of the laser spot region can change the local temperature of the sample, introducing uncertainty in the exact temperature measured. Laser power dependent measurements were made on the Pt/Co sample to estimate the effect of laser heating on the measured iDMI. 10 mW of incident laser power (1.21 kW/cm^2) was chosen to minimize laser heating of the laser spot region while also providing a sufficient signal-to-noise ratio. An achromatic, aspheric cemented-doublet lens with a focal length of 100 mm was used to focus the sample beam, giving a spot diameter of about 33 μm. These measurements were made at an apparent temperature of 50 K.

Magnetometry was performed to determine the temperature profile of the magnetization. A Quantum Design MPMS3 SQUID magnetometer was used to measure magnetic hysteresis loops at selected temperatures. The temperature profile was measured at a fixed saturating field of $\mu_0 H = 100$ mT for the in-plane configuration. An out-of-plane hysteresis loop was measured at room temperature to estimate the anisotropy.

4.3.3 Results and Discussion

Figure 4.1 (a) shows a typical BLS spectra for surface waves in Pt/Co, measured at $T = 238$ K with an applied field $\mu_0 H = 150$ mT. The spin wave signals were fit with a Lorentzian lineshape, and the frequency shift, $\Delta f = |f_{AS}| - |f_S|$, was extracted from the fits. By varying the measured wavevector, as shown for RT in Fig. 4.1 (b), a linear fit to the resulting frequency shifts can be used

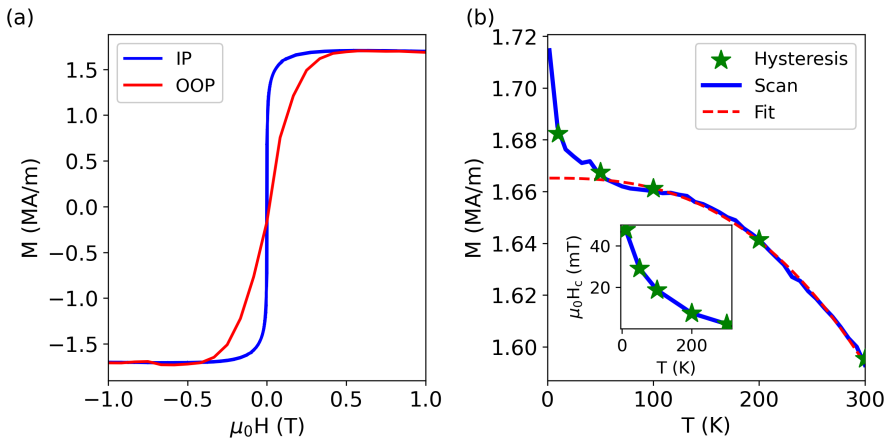

Figure 4.2: (a) Room temperature hysteresis loops for in-plane (blue) and out-of-plane (red) configurations, showing an in-plane easy axis. (b) Magnetization measurements as a function of temperature for Pt/Co at $\mu_0 H = 100$ mT (blue), values extracted from hysteresis measurements at $\mu_0 H = 100$ mT (green stars), and a fit overlaid (red). Coercivity versus temperature is shown in the inset (green stars) where the line is a guide to the eye.

to calculate the iDMI parameter, according to

$$\Delta f = \frac{2|\gamma|D}{\pi M_s} k, \tag{4.2}$$

using a gyromagnetic ratio of $|\gamma| = 177.8$ GHz/T, the saturation magnetization M_s, and the measured wavevector k. For the measurements below room temperature, the wavevector is fixed at $k = 16.7$ rad/μm, which is sufficient to estimate the iDMI parameter using Eq. 4.2.

To understand the temperature dependence of the iDMI, the temperature profile of the magnetization is a necessity. Figure 4.2 (a) shows the RT in-plane and out-of-plane hysteresis loops measured for Pt/Co, while the temperature profile of M_s is shown in Fig. 4.2 (b, blue), measured at a fixed field of $\mu_0 H = 100$ mT. The sample has an in-plane easy axis, with an effective anistropy $K_{\text{eff}} = -0.48$ MJ/m^3. The magnetization above 75 K was fit to the Bloch law,

$$M_s(T) = M_s(0\ K)\left(1 - \left(\frac{T}{T_c}\right)^{\beta}\right), \tag{4.3}$$

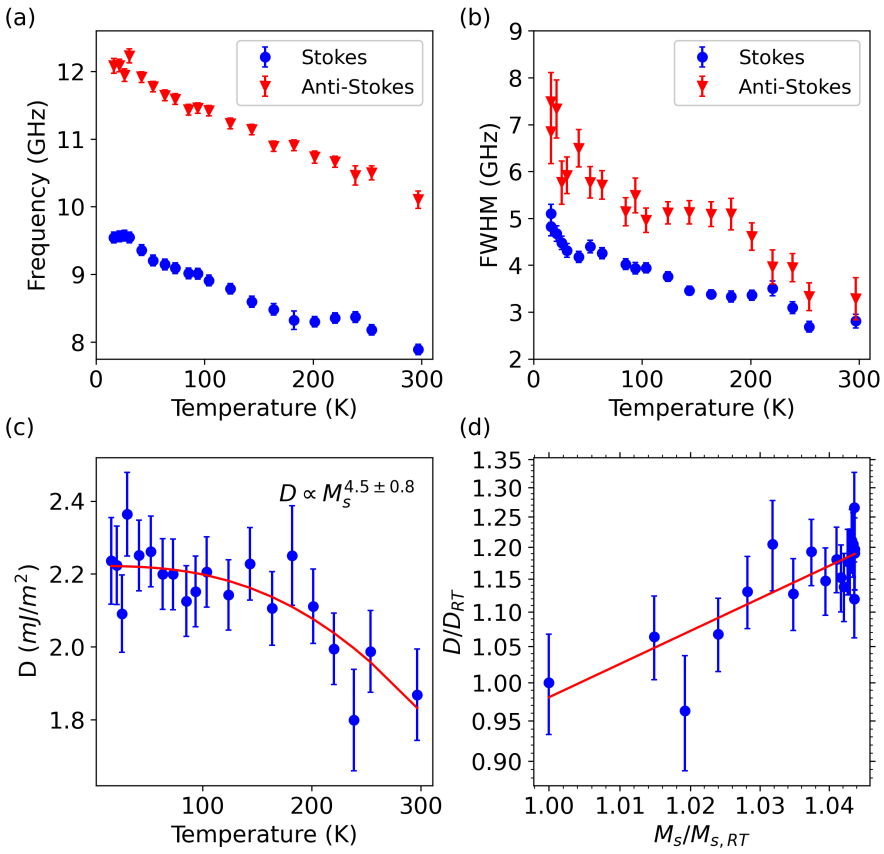

Figure 4.3: (a) Measured spin wave frequencies, Stokes and Anti-Stokes, versus temperature. (b) FWHM of the Lorentzian fit to the spin wave peak. (c) Extracted iDMI parameter D versus temperature, with fit overlaid. (d) Log-log plot of D versus M_s, each normalized to their room temperature value. The linear fit, $\log_{10} D/D_{RT} = \alpha \log_{10} M_s/M_{s,RT} + \beta$, shows a power dependence of $\alpha = 4.5 \pm 0.8$ of D on M_s.

with $M_s(0\ K) = 1665.2 \pm 0.7$ MA/m, $\beta = 2.66 \pm 0.08$, and $T_c = 980 \pm 30$ K. Hysteresis measurements (green stars) at selected temperatures agree well with the temperature scan. The deviation from the Bloch law at $T \leq 75$ K is attributed to the paramagnetic moment of oxygen inclusions in the film, and consequently these points are neglected in the fit. The inset shows the increase in coercivity at low temperatures. The deviation of $M_s(0\ K)$, β, and T_c from their theoretical values can be attributed to the polycrystalline nature of the sputtered film [129].

The surface wave frequencies were made along the range from 15 K to RT to determine the temperature dependence of the iDMI. Fig. 4.3 (a) shows the measured spin wave frequencies and (b) FWHM of the spin wave signal. The FWHM increases strongly at lower temperatures, with an

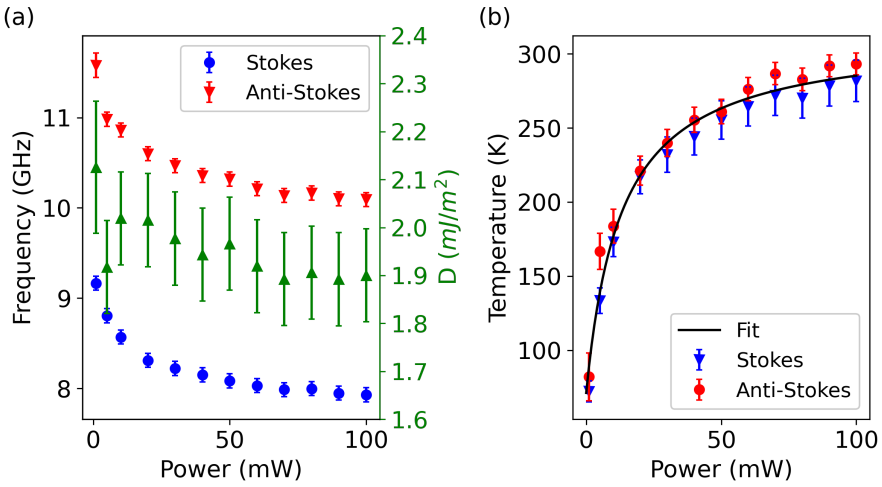

Figure 4.4: (a) Measured spin wave frequencies (blue, red) and D (green) versus incident laser power. (b) Apparent local temperature extracted from linear fits to the spin wave frequencies versus temperature, and from the measured iDMI parameter versus temperature.

increase of 2 GHz for the Stokes frequency and 4.2 GHz for the Anti-Stokes from RT to 15 K. The change in linewidth is consistent with low temperature ferromagnetic resonance studies on similar Pt/Co systems [124]. Using Eq. 4.2 with the measured $M_s(T)$ and $k = 16.7$ rad/μm, the iDMI parameter, shown in (c), is calculated from the frequencies shown in (a). A strong temperature dependence is observed, with a change of -0.36 mJ/m^2 or 16.5%, from 15 K to RT. A log-log plot of D and M_s, Fig. 4.3 (d), normalized to the RT values, shows a strong dependence of D on M_s. The linear fit gives a power relationship of $D \propto M_s^{4.5\pm0.8}$. The resulting temperature dependence of D is overlaid on the data in (c).

From previous theoretical exploration of the iDMI [], we expect that $D \propto M_s^2$ in a mean-field approximation. This proportionality is similar to the exchange parameter, where $A \propto M_s^2$ as well. These studies indicate that the iDMI and the exchange scale with M_s in the same manner. However, we observe a strong deviation from this scaling, as shown in Fig. 4.3 (c,d). This observation is consistent with measurements of the iDMi in temperature ranges above RT, where Zhang et al. [130] report $D \propto M_s^{5.25\pm0.33}$, measured with BLS, and Schlotter et al. [123] report $D \propto M_s^{4.9\pm0.7}$, measured through domain expansion. Both studies were conducted for systems similar to that reported here, being Co/Pt [1.5/1.5 nm] and [Pt/Co/Cu]$_{15}$ [2/1.1/1 nm], respectively. These reports,

taken together, indicate that the iDMI is more sensitive to temperature than predicted. Strain at the interface induced by the change in temperature may be an explanation, as it has been shown to strongly alter the iDMI [122]. As the spatial extent of the iDMI is limited to the interfacial layer [131], any modification of the interface conditions, such as lattice strain, can play a role in altering the iDMI.

Aside from changes in the interface conditions, local heating effects can influence BLS measurements, especially at low temperatures where the heat capacity of the material is lower. To explore the effect of laser heating, power dependent measurements at a fixed cryostat temperature were made. Fig. 4.4 (a) shows the measured spin wave frequencies at a set sample temperature of 50 K for incident laser powers from 1 mW to 100 mW, with the extracted iDMI parameter shown in green. An additional measurement, not shown, was made at 250 mW, but the power density (30.25 kW/cm^2) was sufficient to ablate the film. The laser power is measured just before the sample lens and aperture to the cryostat. Using the frequencies for each temperature and a linear fit to the frequencies shown in Fig. 4.3 (a), the apparent local temperature at each incident power can be estimated. The extracted temperatures are shown in Fig. 4.4 (b) with a fit to the average temperature at each power. A saturating function,

$$T = T_{sat}\frac{P}{P + P_{1/2}} + T_0 \tag{4.4}$$

was used to provide a phenomenological way to estimate the effects of local laser heating. For this function, T_0 is the local temperature with no incident laser, $T_0 + T_{sat}$ is the equilibrium temperature at large laser powers, and $P_{1/2}$ is the laser power at which the local temperature is halfway between T_0 and $T_0 + T_{sat}$. Here, $T_{sat} = 242 \pm 9$ K, $T_0 = 71 \pm 10$ K, and $P_{1/2} = 13 \pm 2$ mW.

10 mW was chosen as the measurement power for the temperature dependent measurements to balance signal-to-noise ratio (SNR) with local heating effects. Laser powers below 10 mW show apparent temperatures closer to the cryostat temperature, but have much longer collection times to achieve a similar SNR. The measurement position was changed between the temperature sweep measurement and the power sweep. The change in local anisotropy conditions, due to

changes in the local interface between measurement positions, shifts the spin wave frequencies by ~ 750 MHz, causing the apparent local temperature extracted from fits to the temperature sweep to be shifted to larger temperatures, resulting in an overestimation of the local apparent temperature.

The local heating of the sample spot size likely resulted in a shift of the measured spin wave frequencies, and consequently the iDMI parameter, at each measurement position in Fig. 4.3 (a,c) toward smaller values. This will change the absolute values measured, but not the temperature dependence, as the shifts should be consistent for each measurement position.

4.3.4 Conclusion

In conclusion, we have measured the temperature dependence of the iDMI along the range from 15 K to RT. We found that $D \propto M_s^{\alpha}$ where $\alpha = 4.5 \pm 0.8$, deviating from theory but consistent with measurements of the iDMI above RT [123, 124]. Changes in strain at the Pt/Co interface are a potential mechanism through which the iDMI may have an increased sensitivity to temperature. We have briefly explored local laser heating effects, which result in a shift of measured iDMI values to lower values. However, at a fixed laser power, the measured temperature dependence of the iDMI remains unchanged.

Chapter 5

Conclusion

This thesis explored two different types of magnonic crystals with time-resolved Brillouin light scattering, and the temperature dependence of the interfacial Dzyaloshinskii-Moriya interaction, a magnetic interaction important in magnonics and for stabilizing chiral spin textures. In Chapter 2, we presented the spatial and temporal mapping of spin wave pulses propagating through a 1D magnonic crystal. The band gap formation, in which spin waves reflected from the magnonic crystal lattice interfere destructively with incident spin waves, was observed building up in time. Additional complex 2D interference patterns were observed, which change rapidly with spin wave frequency and are not reported in the literature, were observed. We provide a method to calculate these interference patterns and show their importance in understanding the spin wave propagation through confined geometries like magnonic crystals.

In Chapter 3, we used time- and spatially-resolved BLS to map the spin wave propagation through a new type of 2D magnonic crystal where the patterned features are small compared to the spin wave wavelength. With the magnonic crystal consisting of square wells in a square lattice rotated by 45°, the formation of spin wave caustic beams from the patterning, as well as from the edge of the crystal, were observed. When the crystal was tilted in the applied field, we show the compression of the spin wave pulse into two narrow caustic beams made the transmission particularly sensitive to the edge characteristics of the sample and to the alignment of the main caustic beams with the patterning lattice.

In Chapter 4, low temperature BLS measurements were performed to determine the temperature dependence of the interfacial Dzyaloshinskii-Moriya interaction. With the use of a cryostat with optical access, we measured the frequency shifts induced by the iDMI at the Pt/Co interface along the temperature range from 15 K to room temperature. We show agreement in the measured temperature dependence, $D \propto M_s^{4.5\pm0.8}$, with that reported in the literature for similar systems above room temperature, measured either by BLS or by domain expansion.

These studies provide insight into important characteristics of spin wave propagation previously ignored, in the case of the 1D magnonic crystal, new regimes of design for magnonic crystals, for the 2D magnonic crystal, and bolster our understanding of the iDMI, a property important in the stabilization of chiral magnetic textures. In all cases, BLS has proven to be an invaluable tool in exploring the behavior of spin waves.

Bibliography

[1] TableStable LTD. *Tandem Fabry-Perot Interferometers TFP-1 and TFP-2 HC*. TableStable LTD.

[2] Quantum Design. *Magnetic Property Measurement System MPMS3 User's Manual*, 2016.

[3] Daniel D Stancil and Anil Prabhakar. *Spin waves*, volume 5. Springer, 2009.

[4] Abdulqader Mahmoud, Florin Ciubotaru, Frederic Vanderveken, Andrii V Chumak, Said Hamdioui, Christoph Adelmann, and Sorin Cotofana. Introduction to spin wave computing. *Journal of Applied Physics*, 128(16):161101, 2020.

[5] Anjan Barman, Gianluca Gubbiotti, S. Ladak, A. O. Adeyeye, M. Krawczyk, J. Grafe, C. Adelmann, S. Cotofana, A. Naeemi, V. I. Vasyuchka, B. Hillebrands, S. A. Nikitov, H. Yu, D. Grundler, A. V. Sadovnikov, A. A. Grachev, S. E. Sheshukova, J. Y. Duquesne, M. Marangolo, G. Csaba, W. Porod, V. E. Demidov, S. Urazhdin, S. O. Demokritov, E. Albisetti, D. Petti, R. Bertacco, H. Schultheiss, V. V. Kruglyak, V. D. Poimanov, S. Sahoo, J. Sinha, H. Yang, M. Münzenberg, T. Moriyama, S. Mizukami, P. Landeros, R. A. Gallardo, G. Carlotti, J. V. Kim, R. L. Stamps, R. E. Camley, B. Rana, Y. Otani, W. Yu, T. Yu, G. E.W. Bauer, C. Back, G. S. Uhrig, O. V. Dobrovolskiy, B. Budinska, H. Qin, S. Van Dijken, A. V. Chumak, A. Khitun, D. E. Nikonov, I. A. Young, B. W. Zingsem, and M. Winklhofer. The 2021 Magnonics Roadmap. *Journal of Physics Condensed Matter*, 33(41):413001, 2021.

[6] A. V. Chumak, A. A. Serga, and B. Hillebrands. Magnonic crystals for data processing. *Journal of Physics D: Applied Physics*, 50(24):244001, 2017.

[7] György Csaba, Ádám Papp, and Wolfgang Porod. Perspectives of using spin waves for computing and signal processing. *Physics Letters, Section A: General, Atomic and Solid State Physics*, 381(17):1471–1476, 2017.

[8] Arabinda Haldar and Adekunle Olusola Adeyeye. Functional magnetic waveguides for magnonics. *Applied Physics Letters*, 119(6):060501, 2021.

[9] V. V. Kruglyak, S. O. Demokritov, and D. Grundler. Magnonics. *Journal of Physics D: Applied Physics*, 43(26):264001, 2010.

[10] Sebastian Neusser and Dirk Grundler. Magnonics: Spin waves on the nanoscale. *Advanced Materials*, 21(28):2927–2932, 2009.

[11] Stuart SP Parkin, Masamitsu Hayashi, and Luc Thomas. Magnetic domain-wall racetrack memory. *Science*, 320(5873):190–194, 2008.

[12] Albert Fert, Nicolas Reyren, and Vincent Cros. Magnetic skyrmions: advances in physics and potential applications. *Nature Reviews Materials*, 2(7):1–15, 2017.

[13] Kwang-Su Ryu, Luc Thomas, See-Hun Yang, and Stuart Parkin. Chiral spin torque at magnetic domain walls. *Nature nanotechnology*, 8(7):527–533, 2013.

[14] Wanjun Jiang, Xichao Zhang, Guoqiang Yu, Wei Zhang, Xiao Wang, M Benjamin Jungfleisch, John E Pearson, Xuemei Cheng, Olle Heinonen, Kang L Wang, et al. Direct observation of the skyrmion hall effect. *Nature Physics*, 13(2):162–169, 2017.

[15] Charles Kittel. *Introduction to solid state physics*. John Wiley & sons, inc, 2005.

[16] Henry Norris Russell and Frederick Albert Saunders. New regularities in the spectra of the alkaline earths. *Astrophysical Journal, vol. 61, p. 38*, 61:38, 1925.

[17] David J. Griffiths and Colin Inglefield. Introduction to Electrodynamics. *American Journal of Physics*, 73(6):574–574, 06 2005.

[18] J. D. Jackson and Ronald F. Fox. Classical Electrodynamics, 3rd ed. *American Journal of Physics*, 67(9):841–842, 09 1999.

[19] Hans T. Nembach, Justin M. Shaw, Mathias Weiler, Emilie Jué, and Thomas J. Silva. Linear relation between Heisenberg exchange and interfacial Dzyaloshinskii-Moriya interaction in metal films. *Nature Physics*, 11(10):825–829, 2015.

[20] Kai Di, Vanessa Li Zhang, Hock Siah Lim, Ser Choon Ng, Meng Hau Kuok, Jiawei Yu, Jungbum Yoon, Xuepeng Qiu, and Hyunsoo Yang. Direct observation of the dzyaloshinskii-moriya interaction in a pt/co/ni film. *Physical review letters*, 114(4):047201, 2015.

[21] Silvia Tacchi, RE Troncoso, Martina Ahlberg, Gianluca Gubbiotti, Marco Madami, Johan Åkerman, and Pedro Landeros. Interfacial dzyaloshinskii-moriya interaction in pt/cofeb films: effect of the heavy-metal thickness. *Physical review letters*, 118(14):147201, 2017.

[22] Kowsar Shahbazi, Joo-Von Kim, Hans T Nembach, Justin M Shaw, Andreas Bischof, Marta D Rossell, Vincent Jeudy, Thomas A Moore, and Christopher H Marrows. Domain-wall motion and interfacial dzyaloshinskii-moriya interactions in pt/co/ir (t ir)/ta multilayers. *Physical Review B*, 99(9):094409, 2019.

[23] Masaya Uchida, Yoshinori Onose, Yoshio Matsui, and Yoshinori Tokura. Real-space observation of helical spin order. *Science*, 311(5759):359–361, 2006.

[24] S. Mühlbauer, B. Binz, F. Jonietz, C. Pfleiderer, A. Rosch, A. Neubauer, R. Georgii, and P. Böni. Skyrmion lattice in a chiral magnet. *Science*, 323(5916):915–919, 2009.

[25] XZ Yu, Yoshinori Onose, Naoya Kanazawa, Joung Hwan Park, JH Han, Yoshio Matsui, Naoto Nagaosa, and Yoshinori Tokura. Real-space observation of a two-dimensional skyrmion crystal. *Nature*, 465(7300):901–904, 2010.

[26] XZ Yu, Naoya Kanazawa, Yoshinori Onose, K Kimoto, WZ Zhang, Shintaro Ishiwata, Yoshio Matsui, and Yoshinori Tokura. Near room-temperature formation of a skyrmion crystal in thin-films of the helimagnet fege. *Nature materials*, 10(2):106–109, 2011.

[27] S. X. Huang and C. L. Chien. Extended skyrmion phase in epitaxial $\mathrm{FeGe}(111)$ thin films. *Phys. Rev. Lett.*, 108:267201, Jun 2012.

[28] A. Fert and Peter M. Levy. Role of anisotropic exchange interactions in determining the properties of spin-glasses. *Phys. Rev. Lett.*, 44:1538–1541, Jun 1980.

[29] See-Hun Yang, Ron Naaman, Yossi Paltiel, and Stuart SP Parkin. Chiral spintronics. *Nature Reviews Physics*, 3(5):328–343, 2021.

[30] Jung-Hwan Moon, Soo-Man Seo, Kyung-Jin Lee, Kyoung-Whan Kim, Jisu Ryu, Hyun-Woo Lee, R. D. McMichael, and M. D. Stiles. Spin-wave propagation in the presence of interfacial dzyaloshinskii-moriya interaction. *Phys. Rev. B*, 88:184404, Nov 2013.

[31] M. Kostylev. Interface boundary conditions for dynamic magnetization and spin wave dynamics in a ferromagnetic layer with the interface Dzyaloshinskii-Moriya interaction. *Journal of Applied Physics*, 115(23):233902, 06 2014.

[32] Bernard Dennis Cullity and Chad D Graham. *Introduction to magnetic materials*. John Wiley & Sons, 2011.

[33] MT Johnson, PJH Bloemen, FJA Den Broeder, and JJ De Vries. Magnetic anisotropy in metallic multilayers. *Reports on Progress in Physics*, 59(11):1409, 1996.

[34] Charles Kittel. On the theory of ferromagnetic resonance absorption. *Physical review*, 73(2):155, 1948.

[35] LALE Landau and Evgeny Lifshitz. On the theory of the dispersion of magnetic permeability in ferromagnetic bodies. In *Perspectives in Theoretical Physics*, pages 51–65. Elsevier, 1992.

[36] Thomas L Gilbert. A phenomenological theory of damping in ferromagnetic materials. *IEEE transactions on magnetics*, 40(6):3443–3449, 2004.

[37] F. Bloch. Nuclear induction. *Phys. Rev.*, 70:460–474, Oct 1946.

[38] N. Bloembergen. Spin relaxation processes in a two-proton system. *Phys. Rev.*, 104:1542–1547, Dec 1956.

[39] M.J. Donahue and D. G. Porter. Oommf user's guide, version 1.0. *NISTIR*, 6376.

[40] Arne Vansteenkiste, Jonathan Leliaert, Mykola Dvornik, Mathias Helsen, Felipe Garcia-Sanchez, and Bartel Van Waeyenberge. The design and verification of MuMax3. *AIP Advances*, 4(10):107133, 10 2014.

[41] Henryk Puszkarski. Theory of surface states in spin wave resonance. *Progress in Surface Science*, 9(5-6):191–247, 1979.

[42] Vladislav E. Demidov and Sergej O. Demokritov. Magnonic waveguides studied by microfocus brillouin light scattering. *IEEE Transactions on Magnetics*, 51(4):1–15, 2015.

[43] Lei Zheng, Lichuan Jin, Tianlong Wen, Yulong Liao, Xiaoli Tang, Huaiwu Zhang, and Zhiyong Zhong. Spin wave propagation in uniform waveguide: effects, modulation and its application. *Journal of Physics D: Applied Physics*, 55(26):263002, 2022.

[44] K Yu Guslienko and AN Slavin. Boundary conditions for magnetization in magnetic nanoelements. *Physical Review B*, 72(1):014463, 2005.

[45] B. A. Kalinikos and A. N. Slavin. Theory of dipole-exchange spin wave spectrum for ferromagnetic films with mixed exchange boundary conditions. *Journal of Physics C: Solid State Physics*, 19(35):7013–7033, 1986.

[46] B.A. Kalinikos. Excitation of propagating spin waves in ferromagnetic films. *IEE Proceedings H (Microwaves, Optics and Antennas)*, 127:4–10(6), February 1980.

[47] Rf W Damon and JR Eshbach. Magnetostatic modes of a ferromagnet slab. *Journal of Physics and Chemistry of Solids*, 19(3-4):308–320, 1961.

[48] Leon Brillouin. Diffusion of light and x-rays by a transparent homogeneous body. *Ann. Phys*, 17(2):88–122, 1922.

[49] W Wettling, MG Cottam, and JR Sandercock. The relation between one-magnon light scattering and the complex magneto-optic effects in yig. *Journal of Physics C: Solid State Physics*, 8(2):211, 1975.

[50] Lev Davidovich Landau, John Stewart Bell, MJ Kearsley, LP Pitaevskii, EM Lifshitz, and JB Sykes. *Electrodynamics of continuous media*, volume 8. elsevier, 2013.

[51] Giovanni Carlotti. Elastic characterization of transparent and opaque films, multilayers and acoustic resonators by surface brillouin scattering: A review. *Applied Sciences*, 8(1), 2018.

[52] J.F. Cochran and J.R. Dutcher. Calculation of the intensity of light scattered from magnons in thin films. *Journal of Magnetism and Magnetic Materials*, 73(3):299–310, 1988.

[53] Paul Rostron, Safa Gaber, and Dina Gaber. Raman spectroscopy, review. *laser*, 21:24, 2016.

[54] AA Stashkevich, M Belmeguenai, Y Roussigné, SM Cherif, Mikhail Kostylev, M Gabor, Daniel Lacour, Coriolan Tiusan, and Michel Hehn. Experimental study of spin-wave dispersion in py/pt film structures in the presence of an interface dzyaloshinskii-moriya interaction. *Physical Review B*, 91(21):214409, 2015.

[55] César L Ordóñez-Romero, Boris A Kalinikos, Pavol Krivosik, Wei Tong, Pavel Kabos, and Carl E Patton. Three-magnon splitting and confluence processes for spin-wave excitations in yttrium iron garnet films: Wave vector selective brillouin light scattering measurements and analysis. *Physical Review B*, 79(14):144428, 2009.

[56] Christoph Mathieu, Valeri T. Synogatch, and Carl E. Patton. Brillouin light scattering analysis of three-magnon splitting processes in yttrium iron garnet films. *Phys. Rev. B*, 67:104402, Mar 2003.

[57] Sergej O. Demokritov and Vladislav E. Demidov. Micro-brillouin light scattering spectroscopy of magnetic nanostructures. *IEEE Transactions on Magnetics*, 44(1):6–12, 2008.

[58] H. J. Jason Liu, Aron Guerrero, Katherine E. Nygren, Mitchell Swyt, and Kristen S. Buchanan. Spin wave wavevector up-conversion in Y-shaped Permalloy structures. *Applied Physics Letters*, 119(17):172403, 10 2021.

[59] Grant Alston Riley. *The Effects of Structural Confinement and Thermal Profiles on Propagating Spin Waves*. PhD thesis, Colorado State University, 2018.

[60] Victorino Franco and Brad Dodrill. *Magnetic Measurement Techniques for Materials Characterization*. Springer, 2021.

[61] MicroSense. *Model 10 Mk II Vibrating Sample Magnetometer*.

[62] M. A. Garcia, E. Fernandez Pinel, J. de la Venta, A. Quesada, V. Bouzas, J. F. Fernández, J. J. Romero, M. S. Martín González, and J. L. Costa-Krämer. Sources of experimental errors in the observation of nanoscale magnetism. *Journal of Applied Physics*, 105(1):013925, 01 2009.

[63] AV Chumak, AA Serga, B Hillebrands, and MP Kostylev. Scattering of backward spin waves in a one-dimensional magnonic crystal. *Applied Physics Letters*, 93(2):022508, 2008.

[64] AV Chumak, AA Serga, S Wolff, B Hillebrands, and MP Kostylev. Scattering of surface and volume spin waves in a magnonic crystal. *Applied Physics Letters*, 94(17):172511, 2009.

[65] Andrii V Chumak, Philipp Pirro, Alexander A Serga, MP Kostylev, RL Stamps, H Schultheiss, K Vogt, SJ Hermsdoerfer, B Laegel, PA Beck, et al. Spin-wave propagation in a microstructured magnonic crystal. *Applied Physics Letters*, 95(26):262508, 2009.

[66] AV Chumak, AA Serga, S Wolff, B Hillebrands, and MP Kostylev. Design and optimization of one-dimensional ferrite-film based magnonic crystals. *Journal of Applied Physics*, 105(8):083906, 2009.

[67] Charles Kittel. Excitation of spin waves in a ferromagnet by a uniform rf field. *Physical Review*, 110(6):1295, 1958.

[68] AA Serga, AV Chumak, and B Hillebrands. Yig magnonics. *Journal of Physics D: Applied Physics*, 43(26):264002, 2010.

[69] CS Davies, A Francis, AV Sadovnikov, SV Chertopalov, MT Bryan, SV Grishin, DA Allwood, Yu P Sharaevskii, SA Nikitov, and VV Kruglyak. Towards graded-index magnonics: Steering spin waves in magnonic networks. *Physical Review B*, 92(2):020408, 2015.

[70] Denis R Candido, Gregory D Fuchs, Ezekiel Johnston-Halperin, and Michael E Flatté. Predicted strong coupling of solid-state spins via a single magnon mode. *Materials for Quantum Technology*, 1(1):011001, 2020.

[71] Masaya Fukami, Denis R Candido, David D Awschalom, and Michael E Flatté. Opportunities for long-range magnon-mediated entanglement of spin qubits via on-and off-resonant coupling. *PRX quantum*, 2(4):040314, 2021.

[72] Yi Li, Wei Zhang, Vasyl Tyberkevych, Wai-Kwong Kwok, Axel Hoffmann, and Valentine Novosad. Hybrid magnonics: Physics, circuits, and applications for coherent information processing. *Journal of Applied Physics*, 128(13):130902, 2020.

[73] HY Yuan, Yunshan Cao, Akashdeep Kamra, Rembert A Duine, and Peng Yan. Quantum magnonics: When magnon spintronics meets quantum information science. *Physics Reports*, 965:1–74, 2022.

[74] Abdulqader Mahmoud, Florin Ciubotaru, Frederic Vanderveken, Andrii V Chumak, Said Hamdioui, Christoph Adelmann, and Sorin Cotofana. Introduction to spin wave computing. *Journal of Applied Physics*, 128(16):161101, 2020.

[75] Huajun Qin, Gert-Jan Both, Sampo J Hämäläinen, Lide Yao, and Sebastiaan van Dijken. Low-loss yig-based magnonic crystals with large tunable bandgaps. *Nature communications*, 9(1):5445, 2018.

[76] Björn Obry, Philipp Pirro, Thomas Brächer, Andrii V Chumak, Julia Osten, Florin Ciubotaru, Alexander A Serga, Jürgen Fassbender, and Burkard Hillebrands. A micro-structured ion-implanted magnonic crystal. *Applied Physics Letters*, 102(20):202403, 2013.

[77] HJ Jason Liu, Grant A Riley, and Kristen S Buchanan. Directly excited backward volume spin waves in permalloy microstrips. *IEEE Magnetics Letters*, 6:1–4, 2015.

[78] Silvia Tacchi, Jorge Flores-Farías, Daniela Petti, Felipe Brevis, Andrea Cattoni, Giuseppe Scaramuzzi, Davide Girardi, David Cortés-Ortuño, Rodolfo A Gallardo, Edoardo Albisetti, et al. Experimental observation of flat bands in one-dimensional chiral magnonic crystals. *Nano Letters*, page 6776–6783, 2023.

[79] Glade Sietsema, Tianyu Liu, and Michael E. Flatté. Electric-field control of magnon gaps in a ferromagnet using a spatially-periodic electric field. *SPIN*, 07(03):1740012, 2017.

[80] Zhi Kui Wang, Vanessa Li Zhang, Hock Siah Lim, Ser Choon Ng, Meng Hau Kuok, Shikha Jain, and Adekunle Olusola Adeyeye. Nanostructured magnonic crystals with size-tunable bandgaps. *ACS nano*, 4(2):643–648, 2010.

[81] ZK Wang, VL Zhang, HS Lim, SC Ng, MH Kuok, S Jain, and AO Adeyeye. Observation of frequency band gaps in a one-dimensional nanostructured magnonic crystal. *Applied Physics Letters*, 94(8):083112, 2009.

[82] G Gubbiotti, S Tacchi, M Madami, G Carlotti, AO Adeyeye, and Mikhail Kostylev. Brillouin light scattering studies of planar metallic magnonic crystals. *Journal of Physics D: Applied Physics*, 43(26):264003, 2010.

[83] Oliver Büttner, Martin Bauer, SO Demokritov, B Hillebrands, Yuri S Kivshar, V Grimalsky, Yu Rapoport, and AN Slavin. Linear and nonlinear diffraction of dipolar spin waves in yttrium iron garnet films observed by space-and time-resolved brillouin light scattering. *Physical Review B*, 61(17):11576, 2000.

[84] HJ Jason Liu, Grant A Riley, César L Ordóñez-Romero, Boris A Kalinikos, and Kristen S Buchanan. Time-resolved study of nonlinear three-magnon processes in yttrium iron garnet films. *Physical Review B*, 99(2):024429, 2019.

[85] Sergej O Demokritov, Vladislav E Demidov, Oleksandr Dzyapko, Gennadii A Melkov, Alexandar A Serga, Burkard Hillebrands, and Andrei N Slavin. Bose–einstein condensation of quasi-equilibrium magnons at room temperature under pumping. *Nature*, 443(7110):430–433, 2006.

[86] Dmytro A Bozhko, Peter Clausen, Gennadii A Melkov, Victor S L'vov, Anna Pomyalov, Vitaliy I Vasyuchka, Andrii V Chumak, Burkard Hillebrands, and Alexander A Serga. Bottleneck accumulation of hybrid magnetoelastic bosons. *Physical Review Letters*, 118(23):237201, 2017.

[87] Zhizhi Zhang, Michael Vogel, José Holanda, Junjia Ding, M Benjamin Jungfleisch, Yi Li, John E Pearson, Ralu Divan, Wei Zhang, Axel Hoffmann, et al. Controlled interconversion of quantized spin wave modes via local magnetic fields. *Physical Review B*, 100(1):014429, 2019.

[88] Evgeny N Beginin, Alexandr V Sadovnikov, Yurii P Sharaevsky, and Sergey A Nikitov. Multimode surface magnetostatic wave propagation in irregular planar yig waveguide. *Solid State Phenomena*, 215:389–393, 2014.

[89] Andrii V. Chumak, Alexander A. Serga, and Burkard Hillebrands. Magnon transistor for all-magnon data processing. *Nature Communications*, 5(May 2013):4700, 2014.

[90] J. Ding, M. Kostylev, and A. O. Adeyeye. Realization of a mesoscopic reprogrammable magnetic logic based on a nanoscale reconfigurable magnonic crystal. *Applied Physics Letters*, 100(7):073114, 2012.

[91] Seung Jae Lee, Dong Kyu Lee, and Kyung Jin Lee. Effect of inhomogeneous Dzyaloshinskii-Moriya interaction on antiferromagnetic spin-wave propagation. *Physical Review B*, 101(6):64422, 2020.

[92] Anulekha De, Sucheta Mondal, Samiran Choudhury, Sourav Sahoo, Sudip Majumder, Saswati Barman, Yoshi Chika Otani, and Anjan Barman. Shape dependent high frequency spin-wave dynamics in nanoscale magnonic crystals. *Journal of Magnetism and Magnetic Materials*, 487(April):165263, 2019.

[93] Arundhati Adhikari, Sudip Majumder, Yoshi Chika Otani, and Anjan Barman. Active Control of Dipole-Exchange Coupled Magnon Modes in Nanoscale Bicomponent Magnonic Crystals. *ACS Applied Nano Materials*, 6(9):7166–7172, 2023.

[94] Chandrima Banerjee, Samiran Choudhury, Jaivardhan Sinha, and Anjan Barman. Pseudo-One-Dimensional Magnonic Crystals for High-Frequency Nanoscale Devices. *Physical Review Applied*, 8(1):014036, 2017.

[95] Anulekha De, Chandrima Banerjee, Avinash Kumar Chaurasiya, Ruma Mandal, Yoshichika Otani, Rajib Kumar Mitra, and Anjan Barman. Anisotropic spin-wave dispersion in two-dimensional Ni80Fe20 diatomic nanodot array. *Journal of Magnetism and Magnetic Materials*, 491(July):165557, 2019.

[96] Mateusz Gołebiewski, Paweł Gruszecki, Maciej Krawczyk, and Andriy E. Serebryannikov. Spin-wave Talbot effect in a thin ferromagnetic film. *Physical Review B*, 102(13):134402, 2020.

[97] V. Veerakumar and R. E. Camley. Magnon focusing in thin ferromagnetic films. *Physical Review B*, 74(21):214401, 2006.

[98] Alexis Wartelle, Franz Vilsmeier, Takuya Taniguchi, and Christian H. Back. Caustic spin wave beams in soft thin films: Properties and classification. *Physical Review B*, 107:144431, Apr 2023.

[99] T. Schneider, A. A. Serga, A. V. Chumak, C. W. Sandweg, S. Trudel, S. Wolff, M. P. Kostylev, V. S. Tiberkevich, A. N. Slavin, and B. Hillebrands. Nondiffractive subwavelength wave beams in a medium with externally controlled anisotropy. *Physical Review Letters*, 104(19):197203, 2010.

[100] T. Sebastian, T. Brächer, P. Pirro, A. A. Serga, B. Hillebrands, T. Kubota, H. Naganuma, M. Oogane, and Y. Ando. Nonlinear emission of spin-wave caustics from an edge mode of a microstructured $Co_2Mn_{0.6}Fe_{0.4}Si$ waveguide. *Physical Review Letters*, 110(6):067201, 2013.

[101] Vladislav E Demidov, Sergej O Demokritov, Daniel Birt, Brian O'Gorman, Maxim Tsoi, and Xiaoqin Li. Radiation of spin waves from the open end of a microscopic magnetic-film waveguide. *Physical Review B*, 80(1):014429, 2009.

[102] C. S. Davies and V. V. Kruglyak. Generation of Propagating Spin Waves from Edges of Magnetic Nanostructures Pumped by Uniform Microwave Magnetic Field. *IEEE Transactions on Magnetics*, 52(7):2300504, 2016.

[103] R. Gieniusz, H. Ulrichs, V. D. Bessonov, U. Guzowska, A. I. Stognii, and A. Maziewski. Single antidot as a passive way to create caustic spin-wave beams in yttrium iron garnet films. *Applied Physics Letters*, 102(10):102409, 2013.

[104] Felix Groß, Mateusz Zelent, Nick Träger, Johannes Förster, Umut T. Sanli, Robert Sauter, Martin Decker, Christian H. Back, Markus Weigand, Kahraman Keskinbora, Gisela Schütz, Maciej Krawczyk, and Joachim Gräfe. Building Blocks for Magnon Optics: Emission and Conversion of Short Spin Waves. *ACS Nano*, 14(12):17184–17193, 2020.

[105] S. Muralidhar, R. Khymyn, A. A. Awad, A. Alemán, D. Hanstorp, and J. Åkerman. Femtosecond Laser Pulse Driven Caustic Spin Wave Beams. *Physical Review Letters*, 126(3):37204, 2021.

[106] Frank Heussner, Matthias Nabinger, Tobias Fischer, Thomas Brächer, Alexander A. Serga, Burkard Hillebrands, and Philipp Pirro. Frequency-division multiplexing in magnonic logic networks based on caustic-like spin-wave beams. *physica status solidi (RRL) – Rapid Research Letters*, 12(12):1800409, oct 2018.

[107] Frank Heussner, Giacomo Talmelli, Moritz Geilen, Björn Heinz, Thomas Brächer, Thomas Meyer, Florin Ciubotaru, Christoph Adelmann, Kei Yamamoto, Alexander A. Serga, Burkard Hillebrands, and Philipp Pirro. Experimental realization of a passive gigahertz frequency-division demultiplexer for magnonic logic networks. *physica status solidi (RRL) – Rapid Research Letters*, 14(4):1900695, 2020.

[108] Jan W. Jaeken and Stefaan Cottenier. Solving the Christoffel equation: Phase and group velocities. *Computer Physics Communications*, 207(June):445–451, 2016.

[109] K. Yu Guslienko, S. O. Demokritov, B. Hillebrands, and A. N. Slavin. Effective dipolar boundary conditions for dynamic magnetization in thin magnetic stripes. *Physical Review B*, 66(13):132402, 2002.

[110] M. P. Kostylev, G. Gubbiotti, J. G. Hu, G. Carlotti, T. Ono, and R. L. Stamps. Dipole-exchange propagating spin-wave modes in metallic ferromagnetic stripes. *Physical Review B*, 76(5):054422, 2007.

[111] K. Yu Guslienko and A N Slavin. Boundary conditions for magnetization in magnetic nanoelements. *Physical Review B*, 72(1):014463, 2005.

[112] Robert E. Camley and Karen L. Livesey. Consequences of the Dzyaloshinskii-Moriya interaction. *Surface Science Reports*, 78(3):100605, 2023.

[113] Hans T Nembach, Emilie Jué, Eric R Evarts, and Justin M Shaw. Correlation between dzyaloshinskii-moriya interaction and orbital angular momentum at an oxide-ferromagnet interface. *Physical Review B*, 101(2):020409, 2020.

[114] Monika Arora, Justin M Shaw, and Hans T Nembach. Variation of sign and magnitude of the dzyaloshinskii-moriya interaction of a ferromagnet with an oxide interface. *Physical Review B*, 101(5):054421, 2020.

[115] Anni Cao, Xueying Zhang, Bert Koopmans, Shouzhong Peng, Yu Zhang, Zilu Wang, Shaohua Yan, Hongxin Yang, and Weisheng Zhao. Tuning the dzyaloshinskii–moriya interaction in pt/co/mgo heterostructures through the mgo thickness. *Nanoscale*, 10(25):12062–12067, 2018.

[116] W Zhang, H Zhong, R Zang, Y Zhang, S Yu, G Han, GL Liu, SS Yan, S Kang, and LM Mei. Electrical field enhanced interfacial dzyaloshinskii-moriya interaction in mgo/fe/pt system. *Applied Physics Letters*, 113(12):122406, 2018.

[117] Baishun Yang, Qirui Cui, Jinghua Liang, Mairbek Chshiev, and Hongxin Yang. Reversible control of dzyaloshinskii-moriya interaction at the graphene/co interface via hydrogen absorption. *Physical Review B*, 101(1):014406, 2020.

[118] Sajid Husain, Naveen Sisodia, Avinash Kumar Chaurasiya, Ankit Kumar, Jitendra Pal Singh, Brajesh S Yadav, Serkan Akansel, Keun Hwa Chae, Anjan Barman, PK Muduli, et al. Observation of skyrmions at room temperature in co2feal heusler alloy ultrathin film heterostructures. *Scientific reports*, 9(1):1085, 2019.

[119] Xin Ma, Guoqiang Yu, Seyed A Razavi, Stephen S Sasaki, Xiang Li, Kai Hao, Sarah H Tolbert, Kang L Wang, and Xiaoqin Li. Dzyaloshinskii-moriya interaction across an antiferromagnet-ferromagnet interface. *Physical review letters*, 119(2):027202, 2017.

[120] Yassine Quessab, Jun-Wen Xu, Chung Ting Ma, W Zhou, Grant A Riley, JM Shaw, HT Nembach, SJ Poon, and Andrew D Kent. Tuning interfacial dzyaloshinskii-moriya interactions in thin amorphous ferrimagnetic alloys. *Scientific Reports*, 10(1):7447, 2020.

[121] Jiawei Jiang, Zhiwen Wang, Jinghua Liang, Qirui Cui, Wenbo Mi, and Hongxin Yang. Interfacial dzyaloshinskii-moriya interaction and perpendicular magnetic anisotropy at

cobalt/diamond interfaces. *Journal of Magnetism and Magnetic Materials*, 529:167852, 2021.

[122] NS Gusev, AV Sadovnikov, SA Nikitov, MV Sapozhnikov, and OG Udalov. Manipulation of the dzyaloshinskii–moriya interaction in co/pt multilayers with strain. *Physical review letters*, 124(15):157202, 2020.

[123] Sarah Schlotter, Parnika Agrawal, and Geoffrey SD Beach. Temperature dependence of the dzyaloshinskii-moriya interaction in pt/co/cu thin film heterostructures. *Applied Physics Letters*, 113(9):092402, 2018.

[124] TGA Verhagen, HN Tinkey, HC Overweg, M Van Son, M Huber, JM Van Ruitenbeek, and J Aarts. Temperature dependence of spin pumping and gilbert damping in thin co/pt bilayers. *Journal of Physics: Condensed Matter*, 28(5):056004, 2016.

[125] Levente Rózsa, Unai Atxitia, and Ulrich Nowak. Temperature scaling of the dzyaloshinsky-moriya interaction in the spin wave spectrum. *Physical Review B*, 96(9):094436, 2017.

[126] R Tomasello, KY Guslienko, M Ricci, A Giordano, J Barker, M Carpentieri, O Chubykalo-Fesenko, and G Finocchio. Origin of temperature and field dependence of magnetic skyrmion size in ultrathin nanodots. *Physical Review B*, 97(6):060402, 2018.

[127] Mikhail Kostylev. Interface boundary conditions for dynamic magnetization and spin wave dynamics in a ferromagnetic layer with the interface dzyaloshinskii-moriya interaction. *Journal of Applied Physics*, 115(23):233902, 2014.

[128] Burkard Hillebrands. *Modern Techniques for Characterizing Magnetic Materials*, chapter Brillouin Light Scattering. Kluwer Academic Publishers, 2005.

[129] Peter Vang Hendriksen, Søren Linderoth, and P-A Lindgård. Finite-size modifications of the magnetic properties of clusters. *Physical Review B*, 48(10):7259, 1993.

[130] Yabing Zhang, Xiangjie Kong, Guofu Xu, Ying Jin, Changjun Jiang, and Guozhi Chai. Direct observation of the temperature dependence of the dzyaloshinskii–moriya interaction. *Journal of Physics D: Applied Physics*, 55(19):195304, 2022.

[131] William Legrand, Yanis Sassi, Fernando Ajejas, Sophie Collin, Laura Bocher, Hongying Jia, Markus Hoffmann, Bernd Zimmermann, Stefan Blügel, Nicolas Reyren, et al. Spatial extent of the dzyaloshinskii-moriya interaction at metallic interfaces. *Physical Review Materials*, 6(2):024408, 2022.

Appendix A

The importance of two dimensional behavior of spin waves in a 1D magnonic crystal

A.1 Calculation of interference patterns with reflections

Spatial Dependence

The complex interference patterns described in this work originate from the interference of many width quantized spin wave modes. These patterns can be calculated following the procedure given in [87]. A brief detailing of this procedure goes as follows. Due to the finite width of the YIG strip, standing modes form across the width of the strip. Each standing mode must have transverse wavevector, k_y, satisfying

$$k_y = n\pi/l \tag{A.1}$$

$$m_n(y) \propto \frac{1}{n} sin(k_y y) \tag{A.2}$$

where l is the width of the YIG strip. With the stripline excitation method used, only odd n modes are excited [67], and their amplitudes go as $1/n$. The longitudinal wavevector k_x for each mode is determined by the dispersion relation shown previously in Fig 2.3. Each mode has a slightly different dispersion relation, giving each mode a different wavevector for the same frequency. The difference in wavevector for each mode causes the overall interference pattern to form. The spatial distribution of the dynamic magnetization, m_n, each mode is then given by

$$m_n(x, y) \propto \frac{1}{n} sin(\frac{n\pi}{l} y) e^{i(k_x x + \phi)} \tag{A.3}$$

where the addition of an arbitrary phase factor, ϕ, will be used to find the maximum in one cycle later. The interference between the modes is given by

$$I \propto (\sum_{n=1}^{45} m_n)^2 \tag{A.4}$$

BLS as a technique is sensitive to the amplitude of the dynamic magnetization, so the maximum of the intensity found in A.4 in one period using the phase factor ϕ is found. This pattern is then what the BLS experiment will detect.

Time Dependence

The model in A.1 does not account for a propagating wave packet, so we must extend m_n to incorporate, in this case, a single square wave. Spatial decay will be introduced as well. The center of the wave packet for each mode will travel at the group velocity, v_g, with a width of 200 ns, chosen to match the width of the experimental pulse. m_n is then given by

$$m_n(x,y,t) \propto sq(x)e^{-x/l_d}\frac{1}{n}sin(\frac{n\pi}{l}y)e^{i(k_x x-\omega t+\phi)} \tag{A.5}$$

$$sq(x) = \begin{cases} 1, & \text{if } |x - v_g t| < v_g \times 100 \text{ ns} \\ 0, & \text{if } |x - v_g t| > v_g \times 100 \text{ ns} \end{cases} \tag{A.6}$$

$$l_d = \frac{v_g}{\alpha_G \omega_0} \tag{A.7}$$

where $sq(x)$ is the square wave packet, l_d is the decay length, $\alpha_G = 1 \times 10^{-5}$ is the damping parameter for YIG, and $\omega_0 = 4.23$ GHz is the ferromagnetic resonance frequency for the applied field. The pulse propagation is now included into the model.

Tracking Reflections

To include reflections from grooves in the sample, the sample is modeled as 41 separate regions. Each groove is two distinct regions: the flat between grooves, and the groove itself. An initial region between the antenna and the first groove is added, as well as the region after the last groove. Each barrier will have a reflection efficiency R, and a transmission efficiency $T = 1 - R$. For MSSW, the $R \sim 0.01$.

When a wave is incident on a partially reflective barrier, such as when moving from one region to the next, it is split by the partial transmission through the barrier. This generates an additional wave traveling in the opposite direction, with an added phase of π. Each of these waves can then propagate to their adjacent regions and be split again. To track the propagation of all of the generated waves, we introduce additional variables A, x_b, x_{tot}, ϕ_r, and β, where A is the wave's amplitude, x_b is the position of the last barrier the wave propagated through, x_{tot} is the

total distance traveled by the wave up to the last barrier, ϕ_r is the phase added by reflections, and $\beta = 0, 1$ accounts for the direction of propagation of the wave. Including these variables, the time dependent magnetization of each wave is given by

$$m_n(x,y,t) \propto \frac{A}{n} sq(x) e^{-(|x-x_b|+x_{tot})/l_d} sin(\frac{n\pi}{l} y) e^{(-1)^\beta i k_x (x-x_b)} e^{-i\omega t} e^{i(k_x x_{tot}+\phi_r+\phi)} \tag{A.8}$$

$$sq(x) = \begin{cases} 1, & \text{if } |x-(x_b+(-1)^\beta(v_g t - x_{tot}))| \leq v_g \times 100 \text{ ns} \\ 0, & \text{if } |x-(x_b+(-1)^\beta(v_g t - x_{tot}))| > v_g \times 100 \text{ ns} \end{cases} \tag{A.9}$$

Each wave can then be parameterized by a list of the variables

$$C_{ij} = \begin{bmatrix} A & \beta & x_{tot} & \phi_r \end{bmatrix}. \tag{A.10}$$

An array of these lists can be generated algorithmically to represent all waves in the sample. The array will be $N \times 41$, where N is how many times the waves will be allowed to propagate from one region to the next, and each column will represent a region in the sample. The first entry in the array represents the initial conditions of the wave excited at the stripline:

$$C_{00} = \begin{bmatrix} \eta_k & 0 & 0 & 0 \end{bmatrix}. \tag{A.11}$$

The amplitude is given by the excitation efficiency, η_{eff}, of the stripline antenna for that wavevector. η_{eff} is taken from the Fourier transform of the field generated by the stripline antenna. The wave will have no distance traveled, propagation in the $+\hat{x}$ direction, and no phase added by reflection. Propagating this wave to the next region generates two waves in the next row of the array:

$$C_{10} = \begin{bmatrix} \eta_k R & 1 & a_0 & \pi \end{bmatrix} \tag{A.12}$$

$$C_{11} = \begin{bmatrix} \eta_k T & 0 & a_0 & 0 \end{bmatrix} \tag{A.13}$$

C_{10} represents the wave reflected from the first barrier, while C_{11} represents the transmitted wave. The amplitude of each is multiplied by the transmission or reflection coefficient, depending. The length of the region is added to the total distance traveled, and the reflected wave has a phase of π added. The next step in propagating the wave will generate two more waves, as the wave traveling towards the antenna is no longer propagated.

$$C_{21} = \begin{bmatrix} \eta_k TR & 1 & a_0 + w & \pi \end{bmatrix} \tag{A.14}$$

$$C_{22} = \begin{bmatrix} \eta_k T^2 & 0 & a_0 + w & 0 \end{bmatrix} \tag{A.15}$$

A third propagation will give

$$C_{33} = \begin{bmatrix} \eta_k T^3 & 0 & a_0 + w + a & 0 \end{bmatrix} \tag{A.16}$$

$$C_{32} = \begin{bmatrix} \eta_k RT^2 & 1 & a_0 + w + a & \pi \end{bmatrix} \tag{A.17}$$

$$C_{31} = \begin{bmatrix} \eta_k R^2 T & 0 & a_0 + 2w & 2\pi \end{bmatrix} \tag{A.18}$$

$$C_{30} = \begin{bmatrix} \eta_k RT^2 & 1 & a_0 + 2w & \pi \end{bmatrix} \tag{A.19}$$

The waves can be continually propagated in this way to track the reflections from all barriers in the sample. Ultimately, there will be multiple waves in each region. The number of waves present becomes large quickly with the number of propagations used, with many waves becoming degenerate with each other in the same region. These waves, which have the same β, x_{tot}, and ϕ_r, are grouped, with their amplitudes added to reduce the number of waves used in the calculation.

With the array of lists generated, the time resolved propagation of the pulse through the sample can be calculated. The magnetization is then calculated for the spatial extent of the sample, over the time range of interest, and the intensity observed via BLS, according to Eq A.4, is found. This

method allows for an arbitrary number of reflections to be accounted for, though in practice the computation time required scales quickly with the number of reflections.

A.2 Supplemental Materials

A snapshot of the spin wave pulse propagating through the magnonic crystal as measured by time-resolved Brillouin light scattering (TR-BLS) is shown for measurement frequencies above ferromagnetic resonance (FMR) in Fig. A1 and below FMR in Fig. A2, and an animation showing the full propagation of the spin wave pulses is included as Supplementary Material. Frames in the animation are spaced by 250 ps. Each measurement was taken in the MSSW geometry with an applied field of $H = 865$ Oe, with spin waves excited at $f = 4.25, 4.305, 4.38$, and 4.455 GHz for BP, BG1, BG2, and BG3, and $f = 4.10, 4.13, 4.15,$ and 4.17 GHz for A, B, C, and D, respectively. Measurement positions are spaced by 50 μm. The excited spin wave pulse has a width of 200 ns, excitation power of 4 dBm, and a pulse spacing of 1250 ns. The excitation power and pulse spacing were chosen to be in the linear response regime and to avoid sample heating. The time integrated measurements for the BP, BG1, BG2, and BG3 are shown in Fig. 2.4 and A, B, C, and D in Fig. 2.5.

Pulse lag times as a function of position are shown in Fig. A3 a) for the BP. The lag times were extracted using cross correlation to track the pulse as it propagated down the length of the magnonic crystal. The reference pulse (Fig. A3 b), black) was taken at the midpoint along the width of the crystal at the first measurement position. The slope of a linear fit to the lag times gives the average group velocity of the spin wave pulse. Predicted direct arrival times for each mode are shown in Fig. A4 for the BP and BG1. Square pulse envelopes were used, with group velocities calculated from the dispersion relation shown in Fig. 2.3. Fig. A4 a) shows the high-n width quantized modes arriving at later times, creating the observed tail on the pulse shape. At times after the main pulse has propagated through the crystal, direct arrivals of high-n modes will be present for the BP, forming the outline of the diamond pattern observed trailing the main pulse in the animation. At BG1 and higher, the tail on the pulse is not due to direct arrivals of slower modes, but due to reflections from grooves.

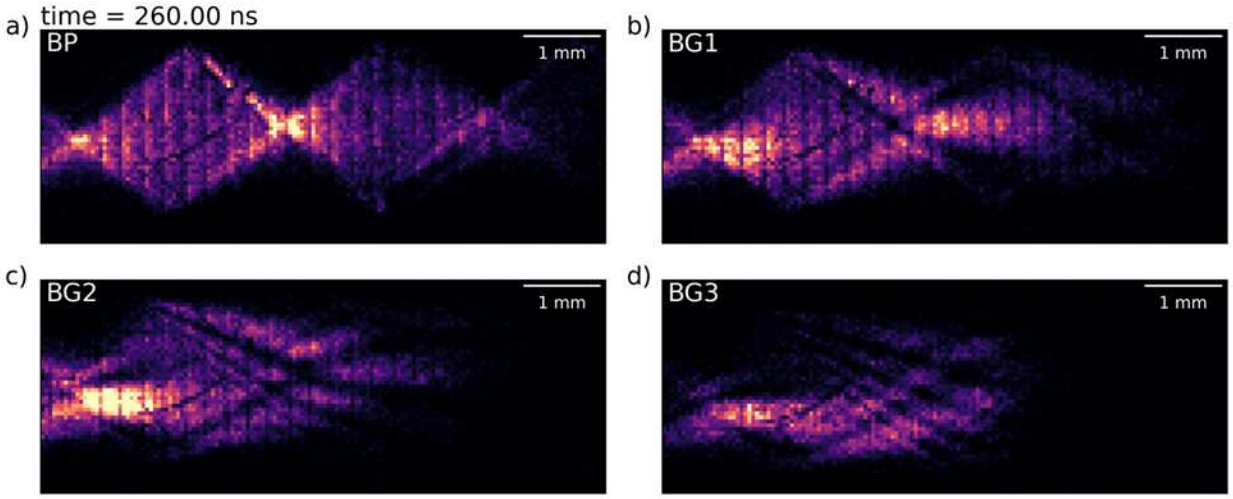

Figure A1: Snapshots of the spin wave pulses for a) the BP, b) BG1, c) BG2, and d) BG3, 260 ns after excitation.

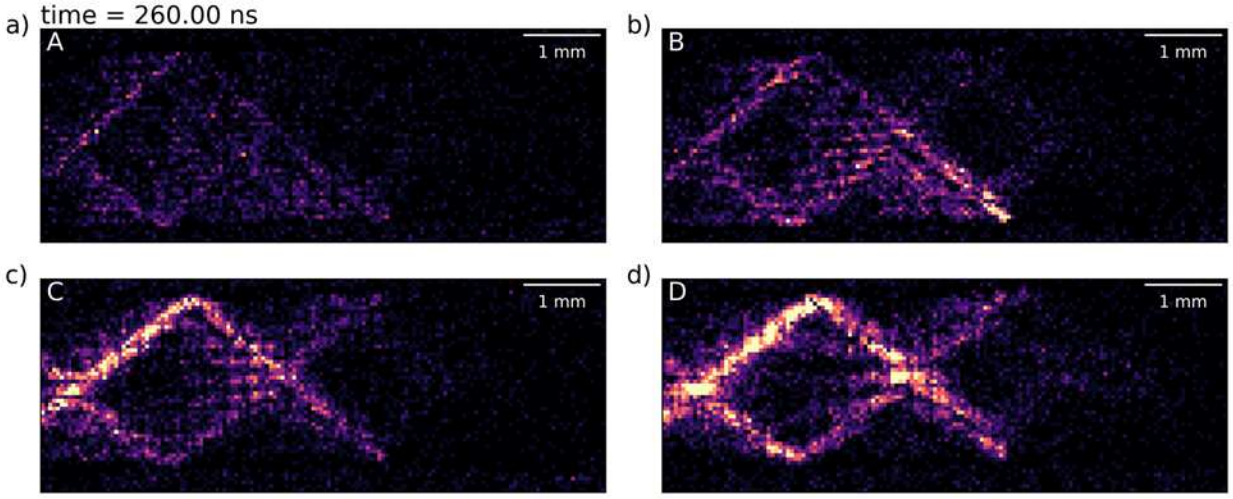

Figure A2: Snapshots of the spin wave pulses for measurement frequencies a) A, b) B, c) C, and d) D, 260 ns after excitation.

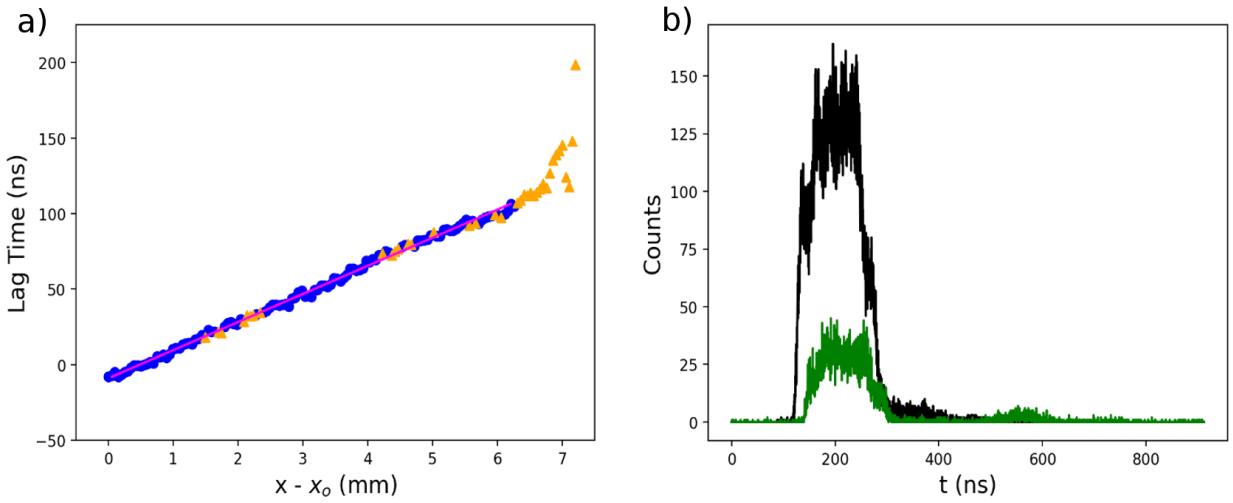

Figure A3: a) Pulse lag times vs. position for the BP, found through cross correlation. Blue markers indicate cross correlation amplitudes greater than 10% of the autocorrelation amplitude, and orange indicate amplitudes lower than 10%. A linear fit (red) to the high amplitude points is overlaid. b) An example of the cross correlated pulses, with the (black) reference pulse and (green) pulse further along the sample.

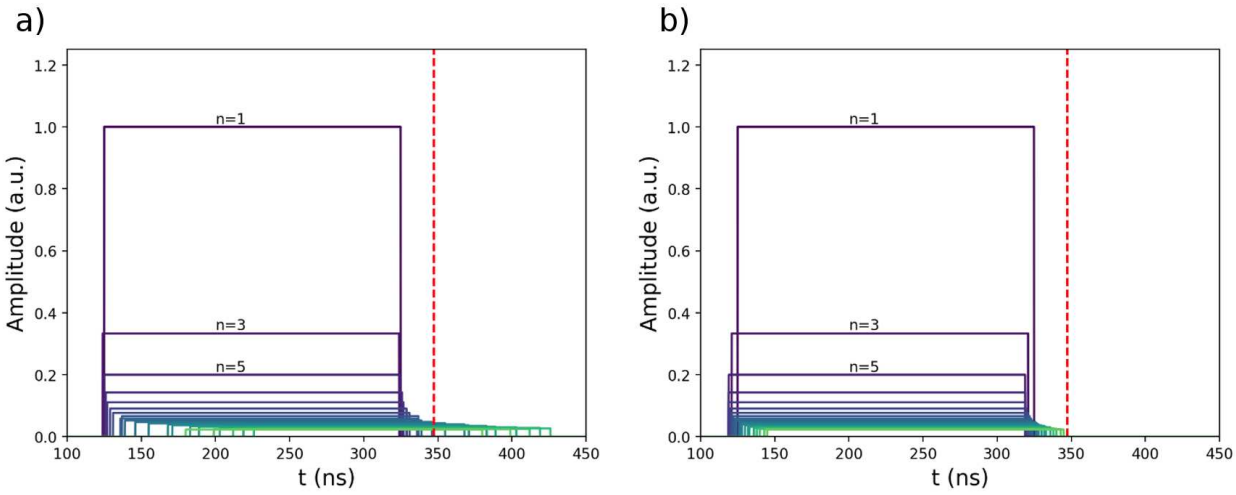

Figure A4: Predicted arrival times for the first 45 odd width quantized modes for a) the BP and b) BG1. The red dashed line indicates the time marked in Fig. 2.8 a), showing the presence of direct arrivals of n≥21 for the BP, and no direct arrivals present for BG1.

Appendix B

Magnonic notch filter based on spin wave caustic beams

B.1 Supplemental Materials

Spin wave transmission measurements were made on an unpatterned yttrium iron garnet (YIG) strip cut from the same wafer as the magnonic crystal using a diamond saw, which is also how the YIG strip for the magnonic crystal was prepared. The unpatterned YIG strip was 6.4-μm thick, 1.92-mm wide, close to the width of the YIG magnonic crystal, and 39.7-mm long. Due to the cutting process, edge defects on the order of 100 μm are present. The exact defects present will differ in the unpatterned and patterned samples, but the general characteristics of the defects are the same. For the measurements on the unpatterned YIG strip, an external field of $H = 770$ Oe was applied using a permanent magnet at angles of $\phi = -20^\circ$ to 20° in steps of 2°, where ϕ is the angle between the short axis of the YIG strip and H as defined in Fig. 3(a). The transmission measurements for $\phi = 0^\circ, +20^\circ$, and -20° are shown in Fig. A1. The external field H used for the measurements shown in Fig. A1 was lower than was used in Fig. 2 ($H = 865$ Oe) so transmission profiles for the spin waves are shifted to a slightly lower frequency range, but the shape of the transmission profiles change little with magnetic field and hence the transmission profile shape can be compared to the measurements shown in Fig. 2. The spin wave transmission measurements were made using three different input antenna positions with the same output antenna location, and the distances between input and output antennas are indicated in the legend.

As shown in Fig. A1(a), the transmission profiles for $\phi = 0^\circ$, the magnetostatic surface wave configuration, show very little transmission at the lowest frequencies, an abrupt increase in transmission at a frequency of just over 4 GHz that coincides with the lowest frequency allowed by the magnetostatic surface wave spin wave dispersion relations, and then the transmitted signal gradually decreases with increasing frequency, which is due to a decrease in antenna efficiency with increasing spin wave wavevector. The transmission profiles for $\phi = 0^\circ$ are smooth, and are quite similar for the different input antenna locations.

The transmission profiles for $\phi = 20^\circ$ and $\phi = -20^\circ$ (Figs. A1(b) and (c)) show a similar onset frequency as the $\phi = 0^\circ$ measurements, however, unlike the $\phi = 0^\circ$ case, the transmission profiles show peaks and dips of varied bandwidths, and the measured features change markedly

with the position of the input antenna. These differences in transmission for $\phi = \pm 20^\circ$ are likely due to edge effects. The transmission profiles begin to show significant differences based on input antenna locations for $|\phi| \geq 4^\circ$, hence the position of the antenna relative to edge defects in the YIG strip becomes an important consideration that can influence spin wave transmission for $|\phi| \geq 4^\circ$, whereas for $|\phi| < 4^\circ$ the spin wave transmission profiles are fairly insensitive to edge effects.

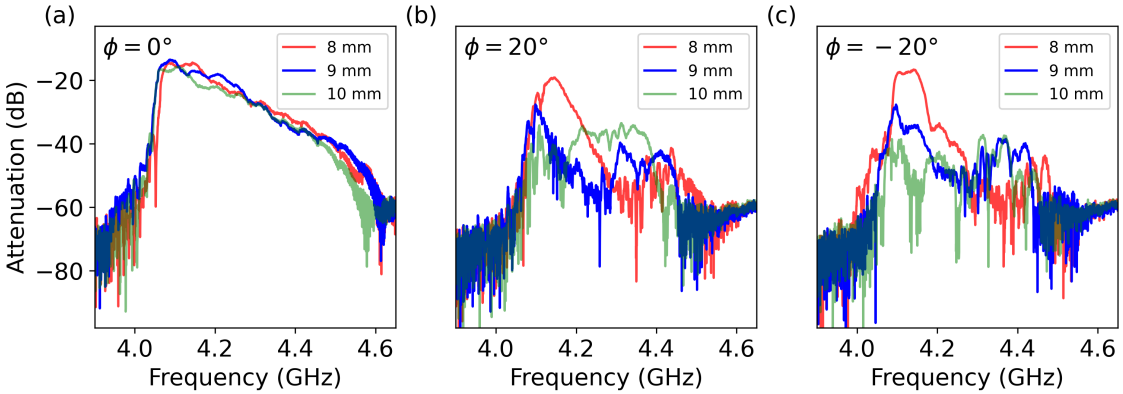

Figure A1: Spin wave transmission profiles of an unpatterned YIG strip measured with three input antenna locations. The legend indicates the input-output antenna separation distance. An external field of $H = 770$ Oe was applied at (a) $\phi = 0^\circ$, (b) $\phi = 20^\circ$, and (c) $\phi = -20^\circ$ from the short axis of the crystal.